

Pathways Towards a Second Generation $^{88}\text{Sr}_2$ Molecular Clock

Emily Tiberi

Submitted in partial fulfillment of the
requirements for the degree of
Doctor of Philosophy
under the Executive Committee
of the Graduate School of Arts and Sciences

COLUMBIA UNIVERSITY

2023

© 2023

Emily Tiberi

All Rights Reserved

Abstract

Pathways Towards a Second Generation $^{88}\text{Sr}_2$ Molecular Clock

Emily Tiberi

For years, frequency standards have been the cornerstone of precision measurement. Among these frequency standards, atomic clocks have set records in both precision and accuracy, and have redefined the second. There is growing interest in more complex molecular systems to complement precision measurements with atoms. The rich internal structure of even the simplest diatomic molecules could provide new avenues for fundamental physics research, including searches for extensions to the Standard Model, dark matter candidates, novel forces or corrections to gravity at short distances, and tests of the variation of fundamental constants.

In this thesis, I discuss the fundamental architecture for a precise molecular system based on a strongly forbidden weakly-bound to deeply-bound vibrational transition in ^{88}Sr dimers. I discuss early studies to characterise our system and gain technical and quantum control over the experiment in anticipation of a precise metrological measurement. I, then, describe the achievement of record-breaking precision for our $^{88}\text{Sr}_2$ molecular clock, ushering in a new era for precision measurement with clocks. Borrowing techniques from previous atomic clock architecture, we measure a \sim 32 THz clock transition between two vibrational levels in the electronic ground state, achieving a fractional uncertainty of 4.6×10^{-14} in a new frequency regime. In this current iteration, our molecular clock is fundamentally limited by two-body loss lifetimes of 200 ms and light scattering

induced by our high-intensity lattice.

Given these limitations, I suggest improvements to combat the effects from both the lattice and two-body collisions in our 1D trap. These include technical improvements to our experiment and strategic choices of particular clock states in our ground electronic potential. I describe in-depth studies of the chemistry and polarizability behaviour of our molecule, which elucidate preferential future directions for a second generation clock system. These empirical results are substantiated by an improved theoretical picture.

Ultimately, our molecular system is built in order to probe new physics and as a tool for precision measurement. Leveraging our record-precision clock and our new-found understanding of our molecule, I predict the capacity for our system to place meaningful, competitive constraints on new physics, in particular on Yukawa-type extensions to gravity. These predictions motivate improvements to our current generation clock and set the stage for future measurements with this system.

Table of Contents

Acknowledgments	xiv
Dedication	xvi
Chapter 1: Introduction	1
1.1 Metrology as Precision Measurement	1
1.2 A Recipe for a Molecular Clock	2
1.3 Evaluating the Quality of our Clock	3
1.3.1 Limitations to clock stability	4
1.3.2 A note about Q factors	5
1.4 Why $^{88}\text{Sr}_2$ is a good candidate	7
1.5 Searches for New Physics	9
Chapter 2: Laying the Groundwork for a Highly Controlled Metrological System	11
2.1 Making Ultracold $^{88}\text{Sr}_2$	11
2.2 State-Insensitive Trapping	15
2.2.1 Mechanism of magic trapping	15
2.2.2 Finding magic wavelengths in our molecular clock	18
2.3 Preferential State-Selection for Magic Trapping	19
2.3.1 Understanding magic detunings	19

2.3.2	Electric-dipole transition strengths in molecules	21
2.3.3	Using line strengths to predict magic detunings	23
2.4	Quantum State Control	27
2.4.1	A complete map of the molecule	27
2.4.2	Coherent transfer of molecules	30
2.5	Long-Lived Molecular States	35
2.5.1	Coherent Rabi oscillations between ground states	35
2.5.2	Lifetime of the absolute ground state	36
2.5.3	Understanding collisional losses	38
Chapter 3: A Systematic Evaluation of Our First Generation Clock		42
3.1	A High-Precision Frequency Measurement in $^{88}\text{Sr}_2$	42
3.1.1	An overview of the clock scheme	42
3.1.2	Methods for technical stabilization of our system	44
3.1.3	Comparison to local time standard	46
3.1.4	An absolute frequency measurement	48
3.2	Systematic Corrections of our Clock Frequency	51
3.2.1	Systematic shifts from light sources	51
3.2.2	Temperature effects	54
3.2.3	The impact of sample density	59
3.3	Limitations of Our Current Clock	60
Chapter 4: Pathways Towards an Improved Clock		62
4.1	Combating Lattice-Induced Scattering	62

4.1.1	A new lattice configuration	62
4.1.2	A search for a new kind of magic wavelength	65
4.1.3	A precise measurement of the dynamic polarizabilities of strontium dimers	69
4.1.4	An improved theoretical picture	75
4.2	Suppressing BBR Shifts in Homonuclear Molecules	80
4.3	Shielding Against Collisional losses	83
4.4	A Proposal for an Improved Molecular Clock	83
Chapter 5: Improving Constraints on Non-Newtonian Gravity		89
5.1	Probing Mass-Dependent Interactions	89
5.1.1	Isotopologues of strontium as a testbed for ultrashort-range gravity	89
5.1.2	Making $^{86}\text{Sr}_2$ molecules	91
5.2	Setting New Constraints on the Yukawa Term	97
5.2.1	Current constraints on α	97
5.2.2	Projected mass-dependent shift in strontium	99
5.2.3	Projected new limits on α	104
Conclusion or Epilogue		106
References		107

List of Figures

1.1	Visual representation of quantum projection noise (QPN) associated with a measurement along the J_z axis of the Bloch sphere. The red arrow shows the state position, while the rainbow shaded region shows the spread associated with the noise of the measurement (left). A sample measurement of a projection along the J_z component of the angular momentum is shown (right). This figure is adapted from [15].	4
1.2	An example of a narrow molecular clock transition with 10.5(1.2) Hz linewidth δf . This transition is achieved by two-photon spectroscopy via an intermediate state (as shown in figure 1.3). The transition frequency f is equal to 31 825 183 207 601.1(3.3) Hz, corresponding to a Q factor of 3.03×10^{12}	6
1.3	A simplified cartoon of our molecular clock system. The clock resonator is a transition between two vibrational states, $ 1\rangle$ and $ 2\rangle$, in the ground electronic potential $X^1\Sigma_g^+$. This transition is strongly forbidden since $g \rightarrow g$ transitions, which do not involve a change in parity, are Laporte forbidden. The transition is, therefore, accessed via an intermediate excited state $ e\rangle$ and two allowed transitions.	8
2.1	A subset of the molecular potentials in $^{88}\text{Sr}_2$. The ground state potential, $X^1\Sigma_g^+$, is taken from empirical data of the strontium dimer [31]. Also shown are the two most relevant excited Hund's case (c) ungerade potentials, 0_u^+ and 1_u , corresponding to atomic $^1\text{S}_0$ - $^3\text{P}_1$ dissociation energy. Models of these excited potentials are fit near-threshold to experimental data of weakly bound binding energies [20]. Adapted from [25].	13
2.2	Simplified schematic of the process of forming $^{88}\text{Sr}_2$ from cooled ^{88}Sr atoms, chronologically from left to right. ^{88}Sr atoms are first laser cooled using a conventional two-stage MOT scheme. The blue MOT addresses the $^1\text{S}_0$ - $^1\text{P}_1$ transition, while the red MOT addresses the narrow-line $^1\text{S}_0$ - $^3\text{P}_1$ transition. We perform repumping on the 3-P states. The atoms are subsequently trapped in a 1D optical lattice. Trapped atoms are photoassociated to weakly bound molecules by coupling the atoms to the $1_u(-1,1)$ state in the excited molecular potential. This state preferentially decays to the least bound, $X_g(62,0)$ or $X_g(-1,0)$, state in the molecular ground, X_g potential.	14

2.3 Our operational experimental protocol. Shown above is a cartoon representation of our sequence including two-stage blue and red MOT cooling and trapping, photoassociation (PA) of atoms to molecules, photodissociation (PD) of molecules back to atoms, and absorption imaging of atomic fragments on the 461 nm atomic transition. Shown below are examples of our absorption images after photodissociation of molecules in $X_g(-1, J = 0, 2)$. Ordinarily both $J = 0$ and $J = 2$ molecules are visible (left). $J = 2$ molecules, with larger momentum, appear as a ring around $J = 0$ molecules due to the finite time of flight during imaging. We can selectively remove $J = 2$ molecules from our sample (right).	16
2.4 The resonance width of a Raman transition, a 2-photon transition via an intermediate state, at various lattice frequencies. The linewidth shrinks dramatically near magic, where lattice-induced and thermal asymmetric broadening are minimized (above). A sample set of the transition spectra at various lattice wavelengths (below). At magic, we find a trace showing a 32(3) Hz linewidth, more than three orders of magnitude narrower. Adapted from [32].	17
2.5 Mechanism for magic trapping. We implement a magic wavelength lattice for our Raman spectroscopy of two states in X_g (green) by coupling our lattice (blue) between the deeply-bound state and an excited state in 1_u (left). By tuning near resonance, we induce a dispersive behaviour in the polarizability of the deeply-bound clock state of the form $\Omega^2/4\delta$ modeled here for Ω_1 , $\Omega_2 = 2\Omega_1$ and $\Omega_3 = 3\Omega_1$ (right). This dispersive change in polarizability facilitates a zero-crossing point with the polarizability of the uncoupled, weakly-bound clock state.	18
2.6 Finding magic lattice wavelength from transition peak centres at high and low lattice intensities. Above we plot individual peak positions fitting a dispersive curve (dashed) of the form $A/(x-x_0)+B$ to describe the polarizability behaviour (above). The region where the two fits intersect corresponds to the region where the magic condition is likely to be met. To quantify the magic wavelength, we plot the differential light shift, as in the shift in peak position between the high lattice and low lattice intensities (below). Sample datasets of individual peak traces show the transition in a high intensity lattice (black) as compared to the transition in a low intensity lattice (red) (right). We infer the magic wavelength by fitting a line to the differential light shift and predicting where it crosses zero.	20
2.7 Line strengths and corresponding magic detunings for pairs of states from $X_g(6, 0)$ to different $1_u(v, 1)$ states. Larger transition strengths (S) are predictors for larger magic detunings (green circles). We show experimental results obtained using two different approaches to measure the lattice intensity: (1) using direct imaging of beam waist (purple circles) and (2) calibrating to the 1S_0 Sr atomic polarizability (green squares). Theoretical predictions from the Morse potential are shown (yellow diamonds) and trends match behaviour in experiment [39].	25

2.8	Transition strengths for pairs of vibrational states in the X_g and 1_u potentials. Below, we zoom in on a particular region of interest to design magic wavelength traps of possible deeply-bound clock states. Importantly, larger transition strengths offer favourable clock configurations. Note that upper (lower) bounds on colorbars represent the upper (lower) cutoffs for plotted transition strengths, and do not necessarily correlate with global maximum (minimum) values. Adapted from [39].	26
2.9	The first 37 (most deeply-bound) vibrational levels of the 0_u^+ potential. A kink in the trend near -1500 1/cm is the result of the avoided crossing in 0_u^+ . Binding energies of the deepest 11 states are fit to equation 2.14, from which we extract the spectroscopic constants for the potential in table 2.1. Adapted from [47].	29
2.10	Scheme for locating ground vibrational levels. The EIT trace shows recovery of the $X_g(-1, 0)$ signal when the detuning of the pump laser is zero (left). This corresponds to the formation of a dark state and indicates that we have located the transition. The two Raman beams are shown in purple (right), where the downleg is fixed on resonance, and the upleg is scanned across the resonance. Adapted from [47].	30
2.11	A complete map of the ground state X_g potential and rotational splittings between $J = 0$ and $J = 2$. Binding energies fit to equation 2.14 from which we extract the spectroscopic constants for the potential in table 2.2. Adapted from [47].	31
2.12	STIRAP transfer scheme. Red and blue arrows show the pump and anti-Stokes transfer lasers via the $0_u^+(11, 1)$ intermediate state (left). We also show the STIRAP transfer scheme, with the conventional time-dependent Rabi frequencies (above), as well as a sample of the population of $X_g(-1, 0)$ as a function of this transfer sequence (below). The one-way efficiency is $\eta = 89(2)\%$	33
2.13	Efficiency of STIRAP transfer. As we detune away from resonance by Δ , we see an increase in efficiency, η , because of scattering near resonance arising from experimental imperfections in controlling probe laser polarization (left). As we tune the lattice to the magic wavelength (dashed line), we see an enhancement in the efficiency of the transfer (right). Adapted from [47].	34
2.14	Two-photon Rabi oscillations between $X_g(-1, 0)$ and $X_g(4, 0)$ (black circles). Favourable magic trapping is achieved by tuning the lattice near the $X_g(4, 0)$ to $1_u(25, 1)$ transition. Also shown are the normalized population decay of $X_g(4, 0)$ (red squares) and $X_g(-1, 0)$ (blue triangles). Adapted from [39].	36
2.15	The lifetime of our absolute ground state molecules, $X_g(0, 0)$. The red curve represents a fit to a two-body loss differential equation, whereas the blue dashed curve represents a fit to a one-body, exponential decay. The decay behaviour clearly favours two-body loss mechanisms, with a lifetime of about 200 ms. Adapted from [47].	38

2.16 Two-body coefficients, β , for $X_g(0, 0)$ and $X_g(62, 0)$. We compare our results to the calculated universal loss rate, $1.22 \times 10^{-10} \text{ cm}^3 \text{s}^{-1}$ (dashed line), and see that our rovibrational ground state molecules collide with near unity probability after a short-range collision. The higher $X_g(62, 0)$ loss rate is suggestive of additional loss mechanisms. Adapted from [47].	41
3.1 Our vibrational molecular lattice clock scheme. Raman lasers (upleg, red arrow; downleg, orange arrow) are detuned from an intermediate state, $0_u^+(11, 1)$ and probe the two-photon vibrational clock transition between $X_g(62, 0)$ and $X_g(0, 0)$. The optical lattice (brown arrow) is parked near resonance, addressing the $1_u(9, 1)$ transition to satisfy the magic condition. Adapted from [18].	43
3.2 A scheme for fibre noise cancellation (FNC) of our probe beams. A laser beam is initially divided on a 50:50 non polarizing beam splitter (BS) cube, and one beam is retro-reflected as a reference, while the other is diffracted by an acousto-optic modulator (AOM) driven by a voltage-controlled crystal oscillator (VCO). Then, the diffracted order is injected into an optical fibre to the experiment. To combat phase noise written by the fibre, we perform active FNC, by retro-reflecting a small portion of the light back through the fibre and recombining it with the original reference light. Beat detection on a low-noise photodiode produces a reference error signal for active feedback on the VCO to preemptively cancel the fibre phase noise. Adapted from [19].	46
3.3 Comparison of our local time standard to global reference time standard. Our local time standard, a Rubidium microwave clock, acts as a flywheel oscillator, linking the molecular clock to GPS time for the absolute frequency measurement. Specifically, we compare our internal 1 pulse-per-second (PPS) from our lab to a reference 1 PPS from GPS via dual-band global navigation satellite system receiver on a time-interval counter. Our GPS time is steered by Coordinated Universal Time (UTC) and International Atomic Time (TAI) giving us a way to locally reference our clock measurements to absolute frequency standards.	47
3.4 Frequency stabilisation of our probe lasers. We utilize a ULE cavity as a reference for our 793 nm upleg probe laser. The repetition rate (f_{RR}) of our frequency comb is phase locked to the upleg probe laser at a beat frequency $f_{b\uparrow}$, inheriting the cavity stability. The downleg 732 nm probe laser is phase locked to the frequency comb at a beat frequency $f_{b\downarrow}$ relative to a higher comb tooth number. The offset of the frequency comb (f_{CEO}) is referenced to the local 10 MHz reference from our rubidium microwave clock standard. Adapted from [19].	48

3.5	Absolute frequency of our clock transition measured over ten trials (left) with all known systematic frequency corrections and comparison to local Rb time base. Blue error bars are 1σ statistical uncertainties, dominated by determination of the comb repetition rate (RR). Red error bars are 1σ systematic uncertainties due to the inherent molecular clock uncertainty (see table 3.1). Black error bars are 1σ total uncertainties, where the uncertainties of the local time-base calibrations are added in quadrature with the statistical and molecular clock systematic uncertainties. The black horizontal line shows the weighted average, and the shaded gray area shows the associated 1σ standard error of the mean. Histogram (right) of all clock frequency measurements in the ten trials, relative to the weighted average of f_{clock} . The solid red line is a Gaussian fit to the histogram. Adapted from [18].	50
3.6	Light shifts from our Raman probe lasers as a function of the upleg laser intensity (left), and the downleg laser intensity (right). The horizontal axes are normalized to operational intensities, $I_{\uparrow,opt}$ and $I_{\downarrow,opt}$. Solid lines are linear fits to the data. Residuals are plotted in units of Hz. Adapted from [18].	52
3.7	Clock shifts due to the lattice light. We show nonlinear shifts of the molecular clock frequency versus trap depth (above). For a given lattice frequency (color coded), we make interleaved measurements of clock shifts (open circles) with respect to a reference trap depth ($\sim 500 E_r$), and fit the data to parabolas (solid lines) with a global quadratic parameter, $-\beta$. We plot the linear light shift coefficient, α , versus lattice frequency (color code matches above), as extracted from the linear fit (black solid line) (below). Adapted from [18].	53
3.8	Chamber temperature logging scheme for BBR shift measurement. We measure the temperature of the stainless steel chamber on four faces using high-precision 10 k Ω MC65F103A Amphenol negative temperature coefficient (NTC) thermistors (below). We continuously record the temperature using a Keithley DAQ6510/7700 system and a home-built, python-based GUI for remote control (above).	57
3.9	Modeled blackbody radiation shift on $X_g(v, 0)$ states at an effective environment temperature $T_r = 300$ K. For our current clock states, $X_g(0, 0)$ and $X_g(62, 0)$, the net BBR shift on the observed clock frequency is $\delta f_{BBR} = 0.70(14)$ Hz. The dynamic term η (equations 3.15 and 3.16) at T_r , included in δf_{BBR} , contributes less than 0.5% to the measured shift.	58
3.10	Differential BBR shift between $X_g(0, 0)$ and other $X_g(v, 0)$ states in the ground potential, as predicted by early theoretical models. These models show state pairs that may exhibit near zero BBR shift corrections at $T = 300$ K.	59

3.11 Evaluation of density-shift systematic. Clock shifts due to molecular collisions are compared to operating conditions (left). We find a small, non-zero correction of $\delta f_{density} = -0.20(10)$ Hz due to these density-dependent collisional shifts. In the same dataset, the shift between successive resonances taken under identical experimental settings serves as a control experiment to check for technical offsets. As expected, this averages to zero, 0.03(20) Hz (right). Both insets show the histogram of normalized residuals, and the solid red lines are Gaussian fits. Adapted from [18].	60
4.1 Design for a new vertical lattice configuration. Probe (clock) and lattice beams are combined along the vertical axis on dichroic beamsplitters (see main text for details). Probes are fed from above, while the lattice is counter-propagated from below.	64
4.2 Home-designed and machined mirror mount for vertical lattice construction.	65
4.3 Polarizability of the electronic ground vibrational states, as predicted by early theoretical models. These models show potential preferable state pairs for vibrational states $v < 28$ with naturally occurring equal DC polarizabilities, $\alpha_0(v)$ (above). These pairs of states may present favourable clock conditions with near zero BBR shift corrections and significant suppression of lattice-induced scattering. This non-monotonic behaviour emerges at wavelengths longer than 1000 nm, and may offer alternative constructions of a magic IR trap (below).	66
4.4 A comparison of two magic trapping schemes. Right axis (black) shows the differential polarizability around conventional near-resonant magic wavelength. Left axis (blue) shows the differential polarizability around predicted off-resonant magic wavelengths. The slope of each curve describes the sensitivity of our system to changes in the lattice frequency. Off-resonant magic wavelengths are 10^5 times less sensitive than our conventional traps. Below, we zoom in to region just around the magic condition, while, above, we show proximity to resonance [25].	67
4.5 Differential polarizability of pairs of clock states in the telecom range (1450-1650 nm). Theory predicts an array of states between $X_g(0, 0)$ and $X_g(21, 0)$, whose differential polarizability is naturally zero. The magic condition is predicted to be satisfied every ~ 15 nm [25].	68
4.6 A scheme for probing the light shift on a clock transition from a auxiliary 1950 nm light source. We perform spectroscopy of our molecular clock transition using a two-photon Raman transition via an intermediate state in the 0_u^+ (red arrows) in a magic lattice that couples our deeply-bound clock state to an excited 1_u state (blue arrow). We induce Stark shifts to probe differential polarizabilities of ground rovibrational states with 1950 nm light (orange arrow).	70

4.7	Light shift of the $X_g(0, 0)$ state with 1950 nm light. We measure the linear light shift as a function of 1950 nm laser power (left). Each point is measured by interleaving scans of the resonance with the 1950 nm light on and off, and averaging over five runs. An example scan at 1.1 W is shown (right).	71
4.8	Calibration of the 1950 nm light intensity to polarizability of the ^{88}Sr $^1\text{S}_0$ to $^3\text{P}_1$ transition. We calibrate the light intensity by referencing the light shift on the intercombination line (right, blue) to the $X_g(62, 0)$ to $X_g(27, 0)$ transition (left, red).	72
4.9	Differential polarizability of a set of $X_g(v, 0)$ states with respect to $X_g(-1, 0)$. The states in the ground state show a monotonic behaviour with binding energy, contrary to previous theoretical predictions (orange), which largely overestimate the polarizability difference in our ground state molecule. Comparisons to <i>ab initio</i> theory (blue) are in good agreement with experiment (see section 4.1.4 for details).	74
4.10	Interaction-induced ac polarizability at $\lambda = 1.95 \mu\text{m}$. In addition to the <i>ab initio</i> result we show absolute experimental polarizabilities in relation to mean internuclear distances \tilde{R} . Horizontal bars indicate the range $[\tilde{R}_v - S_{R_v}, \tilde{R}_v + S_{R_v}]$ of internuclear distances probed by the vibrational wavefunctions shown in the lower panel. Here \tilde{R}_v and S_{R_v} are the mean and standard deviation internuclear distances for wavefunction squared treated as a probability distribution. R_e and R_{LR} are, respectively, the equilibrium distance and the LeRoy radius [93, 94].	77
4.11	Differential polarizability with respect to the least-bound $v = 62$ state in ground state Sr_2 . Points denote experimentally measured ac polarizabilities at $\lambda = 1.95 \mu\text{m}$. Lines are <i>ab initio</i> polarizabilities from dc to $\lambda = 1.25 \mu\text{m}$	78
4.12	(a) Differential polarizabilities for the selected clock transitions. Below, a plot of a BBR spectral radiance $B_\omega(T)$ at 300 K. (b) Absolute BBR shift for $0 \leftrightarrow v'$ clock transitions. (c) Relative BBR uncertainty for the same clock configurations.	82
4.13	Projected Q factor for a non-magic deeply-bound clock construction. We compare the Q factor of a non-magic $X_g(0, 0)$ to $X_g(1, 0)$ with our current record clock at various temperatures (above). This new clock only outperforms our current clock at very low temperature, $\sim \text{nK}$. At $2 \mu\text{K}$, the $X_g(0, 0)$ to $X_g(1, 0)$ clock, which has minimum polarizability mismatch, offers the best Q factor, still orders of magnitude lower than our current clock. We conclude that non-magic clocks are not a viable option for the highest-precision experiments.	85

4.14 Modeling the polarizability behaviour of $X_g(0, 0)$ and $X_g(v, 0)$ in near-resonant magic traps. We plot the resonant behaviour of $X_g(0, 0)$ polarizability around the $1_u(9, 1)$ excited resonance and fit a line to model the background polarizability (above) [25]. The intersection with the $X_g(62, 0)$ occurs at 4.49 GHz detuned from resonance as measured in our experiment [18]. We estimate the polarizability of other clock states in this region using $\delta\alpha_{62,0}$ and assume a linear $\delta\alpha/\delta\nu$. Since $R_{scatt} \sim 1/\Delta^2$, we predict magic detunings for other clock states in order to capitalise on improvement in molecular lifetime.	87
4.15 Projected Q factor of $X_g(0, 0)$ to $X_g(v, 0)$ in near-resonant magic traps. We find two orders of magnitude improvement in the Q factor of a resonant magic $X_g(0, 0)$ to $X_g(1, 0)$ clock over our current clock.	88
5.1 A scheme for transverse cooling in our molecular clock. We pick off a small amount of light from our Zeeman slower for additional cooling along the transverse direction, just after our strontium oven. Our current apparatus accommodates transverse cooling through two existing windows. We can achieve adequate trapping of ^{86}Sr and ^{84}Sr in the blue MOT with a 10 cm interaction region.	93
5.2 A protocol for interleaved cooling and trapping of ^{86}Sr and ^{88}Sr atoms in our system. We use TTL-enabled AOMs to selectively modulate light at a frequency matching the isotope shift for a given transition. An additional AOM (AOMO 3200-125) is included in the red MOT optical path to shift the frequency of light by ~ 164 MHz and another AOM (AOMO 3110-120) is included in the blue MOT optical system to shift the frequency of blue light by ~ 125 MHz before it is distributed to the Zeeman slower and 3 MOT arms. We can switch between input from modulated (-1 order) light and unmodulated (0 order) light using a TTL-enabled fibre switch.	95
5.3 A protocol for interleaved creation of weakly-bound $^{86}\text{Sr}_2$ and $^{88}\text{Sr}_2$ molecules. We use a TTL-enabled fibre switch to selectively send photoassociation light to the experiment from two separate, phase-locked lasers. We phase lock the two lasers at ~ 1 GHz, a frequency which matches the isotope shift of the PA line relative to $^{88}\text{Sr}_2$	96
5.4 The current constraints on the interaction constant, α , and interaction range, λ , of the Yukawa-type interaction from various experiments. Previous measurements include micro-mechanical measurements of the effective Casimir pressure, measurements of the Casimir force using a torsion pendulum, Cavendish-type experiments and neutron scattering experiments [119, 122–125]. The regions above each line are excluded, and those below each line are allowed.	98

5.5	Projected shift from the additional Yukawa-type potential. We treat the additional Yukawa term as a perturbation to the Hamiltonian as in equation 5.3 and calculate the projected isotope shift between $^{86}\text{Sr}_2$ and $^{88}\text{Sr}_2$ as a function of vibrational state for a series of ranges, λ . α for each range is set at the current limit. Different vibrational states probe different internuclear separations, and deeply-bound states are more sensitive overall to the Yukawa force. The shaded region corresponds to current absolute clock resolution [18].	100
5.6	Projected shift from the additional Yukawa-type potential as a function of λ . Different vibrational states probe different internuclear separations, and deeply-bound states are more sensitive overall to the Yukawa force. The onset of response corresponds to the particular wavefunction of the state.	101
5.7	Isotope shift of the $X_g(62, 0)$ and $X_g(61, 0)$ to $X_g(0, 0)$ clock transitions in $^{86}\text{Sr}_2$ and $^{88}\text{Sr}_2$. Isotope shifts are calculated by constraining $\alpha = 10^{21}$ for the Yukawa-type potential as in equation 5.3. We show individual frequency shifts introduced by the perturbation for each of $X_g(0, 0)$, $X_g(62, 0)$ and $X_g(61, 0)$ as a function of the range, λ (above). Note that $X_g(62, 0)$ state in $^{86}\text{Sr}_2$ has a very small binding energy, -83 kHz, and very long mean bond length, $4436.70\text{ }a_0$; it experiences a small shift by comparison to the other states studied. We consider pairs of states corresponding to potential clock transitions of interest and predict the corresponding isotope shift, $\delta\nu_{IS}^{\text{Yukawa}}$ (below). We find overall isotope shifts on these clock transitions on the order of ~ 100 Hz, which is resolvable with our current clock precision.	102
5.8	Isotope shift of the $X_g(62, 0)$ and $X_g(1, 0)$ to $X_g(0, 0)$ proposed clock transitions in $^{86}\text{Sr}_2$ and $^{88}\text{Sr}_2$. Isotope shifts are calculated by constraining $\alpha = 10^{21}$ for the Yukawa-type potential as in equation 5.3. We show individual frequency shifts introduced by the perturbation for each of $X_g(0, 0)$, $X_g(1, 0)$ and $X_g(62, 0)$ as a function of the range, λ (above). We consider pairs of states corresponding to clock transitions of interest and predict the corresponding isotope shift, $\delta\nu_{IS}^{\text{Yukawa}}$ (below). The $X_g(1, 0)$ to $X_g(0, 0)$ transition is relatively insensitive to the Yukawa term.	103
5.9	Projected constraints on the interaction constant, α , and interaction range, λ , of the Yukawa-type interaction from our clock experiment. We demonstrate improvement by an order of magnitude on constraints on α in the range $\lambda < 1.3$ nm. In this range, we constrain alpha to below below $\alpha = 5.5 \times 10^{19}$ for $\lambda = 1$ nm and below $\alpha = 2.6 \times 10^{21}$ for $\lambda = 0.1$ nm. Current limits are included [122] and other molecular experiments are shown [113, 129].	105

List of Tables

2.1 Extracted spectroscopic constants of 0_u^+ in units of cm^{-1} . They are obtained by fitting equation 2.14 to the 11 most deeply-bound states. Note that since we only measure states of the same angular momentum ($J = 1$), we cannot separate the vibrational and rotational constants when fitting. Theoretical comparisons are from [43].	28
2.2 Spectroscopic constants for X_g in units of cm^{-1} . They are obtained by fitting equation 2.14 to the deepest 8 bound states. We measure binding energies of $J = 0$ as well as rotational splittings from $J = 2$ states. Theoretical comparisons are taken from [31, 46].	28
3.1 A systematic uncertainty budget for the strontium molecular clock. Frequency corrections (f_{corr}), with corresponding uncertainties ($\sigma_{f_{corr}}$), are listed for the primary contributions to the clock uncertainty. The true clock frequency f_{clock} is given by adding these corrections to the measured clock frequency (f_{meas}) (as shown in equation 3.4). All values are expressed in fractional units ($\times 10^{-14}$).	49
4.1 Probing the dynamic polarizabilities throughout the electronic ground state. Relevant states, $X_g(v, 0)$, with corresponding binding energies relative to $X_g(62, 0)$, intermediate transition, $0_u^+(v', 1)$ and magic wavelengths and corresponding 1_u states are listed.	73
4.2 A comparison of experimental differential polarizabilities to <i>ab initio</i> theory.	79
4.3 Contributions to the BBR shift at 300 K for the $0 \leftrightarrow 1$ and $0 \leftrightarrow 62$ transitions.	81
5.1 Isotope shifts between ^{88}Sr and ^{86}Sr for the primary cooling and trapping transitions. Shifts on repump lines are ~ 100 MHz, but are not listed here since the blue MOT capture number is relatively insensitive to frequency changes in the repumps at the level of the isotope shift [106, 107].	92

Acknowledgements

Pursuing my PhD has been equal parts challenging and rewarding. I am grateful for all that I have experienced in this time and learnt about myself, and I would like express my deepest gratitude for those who supported me through the failures and celebrated my successes.

Firstly, I would like to thank my supervisor, Prof. Tanya Zelevinsky, for the opportunity to work on the Sr molecular clock experiment. I was, and remain, excited by the deep, fundamental questions about nature that we investigate, and the chance to work day-to-day on a state-of-the-art experiment. I feel lucky to be a part of Tanya's research group and for the chance to share the space with many brilliant and motivated young scientists from whom I have learnt so much. I would also like to thank Jeremy Dodd, who has been an unofficial mentor and friend to me throughout my PhD.

The work in this thesis would not be possible without the support and hard work of many others. Many graduate students and postdocs before me put in tireless hours to build this machine from the ground up, making the work in this thesis possible. In my early years at Columbia, I had the opportunity to work closely with Stanimir Kondov, Chih-Hsi Lee, Hendrik Bekker, and Kon H. Leung, who helped me develop crucial skills in the lab and grow from student to scientist. I would like to extend special thanks to our current postdoc, Mateusz Borkowski, from whom I have learnt a lot this last year and who has provided invaluable advice, theoretical expertise and a new vision for the future of our experiment... all with a dose of dad humour. Most of all, I wish to

thank Brandon Iritani, with whom I worked most closely in my final year. Beyond my confidence in him has a researcher, I owe a debt of gratitude to Brandon for his personal support, for the joy and laughter of working in the lab with him day after day, and for his friendship. I feel confident leaving the experiment in his more than capable hands and am excited to see what the years ahead have in store for him. I am also very grateful to the other ZLab members I had the pleasure of working with, including Mick Aitken, Konrad Wenz, Sebastian Vazquez-Carson, Debayan Mitra, Qi Sun, Jinyu Dai and Perry Zhou. I thank them for their help and advice, for the countless hours of conversation in the office and for their friendship.

Graduate school has been a time when I have stretched myself the most, and a time of tremendous growth. I could not have succeeded without the unending support of my family and close friends. It is through these relationships that I have become the person I am today. They are the most important people in my life, and have been and continue to be my motivation to learn, to grow and to ever improve myself in my work and in life.

*This thesis is dedicated to my mom and dad,
and to my grandparents, who worked every day to give me this future.*

Chapter 1: Introduction

1.1 Metrology as Precision Measurement

The primary aim of a precision measurement experiment is to utilize specialized tools to probe new physics, or to refine our previous interpretation. By nature, precision measurement experiments work hand-in-hand with theory: our experiments are motivated by ever-changing theoretical pictures — whether they be new exotic particles, new forces or new physical interpretations — and, likewise, precision measurements are integral to testing new avenues of theory.

Traditionally, physicists have probed new physics at energies on the order of 1 GeV or larger, in particle accelerators or in exotic astrophysical events [1]. By contrast, precision measurement in atomic, molecular and optical (AMO) physics operates at very low temperatures and energies, on the order of $\sim 1 \mu\text{K}$ or 10^{-12} eV , where the interactions are extremely weak and the effect of any new, exotic physics will be extremely small. Nevertheless, we can leverage highly-controlled, ultracold atoms and molecules to ask (and answer) these same questions. Given that the interactions we hope to investigate are so weak, it is, therefore, imperative that we rely on state-of-the-art technology to build precise machines. The advantage? We can develop these table-top experiments at a fraction of the cost and with a limited footprint. What is more, atoms and molecules are an incredibly flexible, lego-like platform with which to build tailor-made experiments.

At these low energies, we rely on precision measurement as we aim to answer increasingly complex questions about the physical world around us. As we move ever further towards the frontiers of our understanding, we need to continue to push the boundaries of technique. For years, high-precision frequency standards have been the cornerstone of precision measurement. Among

these frequency standards, atomic clocks have set records in both precision and accuracy [2], and have redefined the second. By definition, any clock uses time-keeping as the essential standard for a measurement. In particular, an atomic clock utilizes the optical transition between two electronic states in the atom as the resonator. This characteristic frequency is fundamental to the atom and, therefore, is a standard for measurement. Variations in this frequency might arise due to changes in the environment or might signal new, anomalous forces beyond the Standard Model. The current record precision of an atomic clock is on the order of one part in 10^{19} [3]. As we continue to push these technical limits, it is also crucial to explore new scientific directions that may probe a new part of the landscape.

Here, I consider a molecule-based lattice clock as a versatile platform for new physics beyond the scope of current atomic lattice clocks [4, 5]. Even the simplest diatomic molecules could provide new channels for fundamental physics research, including searches for extensions to the Standard Model [6], dark matter candidates [7, 8], novel forces [9, 10] or corrections to gravity at short distances [11, 12], and tests of the variation of fundamental constants [13, 14]. I discuss the potential questions that we might investigate with our particular system, as well as the technical challenges we face in building a molecular system. Ultimately, I will suggest pathways towards a more precise clock.

1.2 A Recipe for a Molecular Clock

At its foundation, our experiment seeks to develop a high-precision tool for tests of fundamental physics. This necessitates that our molecular clock be both highly precise and incredibly accurate. To achieve this, our molecular clock should meet a number of requirements:

- The clock transition should have a very narrow linewidth.
- The clock transition should be insensitive to magnetic or electric fields.
- The clock transition should be accessible with available laser technology.

- The molecules should be long-lived in these states.
- The molecules should be highly controlled and allow for precise state-selection.
- The technical system should allow for coherent transfer between clock states.
- The technical system should be well-controlled and understood.

In the following chapters, I will describe how we develop a molecular clock that meets each of these conditions, as well as why they are imperative when building a precise and accurate measuring tool.

1.3 Evaluating the Quality of our Clock

As we look towards designing and building a metrological system, it is important to understand the technical and fundamental limitations of the precision we can achieve. Throughout this thesis, we will discuss avenues to improve our clock precision by combating technical challenges and mitigating inherent limitations. In clock systems, instability refers to the variation in the measured clock frequency over a given averaging time. The instability of a clock is given by the Allan deviation, $\sigma_y(\tau)$, which estimates the frequency stability due to noise processes

$$\sigma_y(\tau) \sim \frac{\delta f}{f} \frac{1}{\sqrt{N\tau}} \quad (1.1)$$

where δf is the observed linewidth of the clock transition with frequency f , N is the number of atoms or molecules probed per second and τ is the total averaging time of the measurement. It is convention to report clock precision in relation to the total interrogation (averaging) time of the experiment.

Clock experiments will usually average over a certain period of time to reach a given reported precision, but this total averaging time must be reasonable, in other words, must be feasible in a real experimental setup over the course of hours and days. The requirements for what is reasonable

may differ depending on a given precision measurement. For comparison, an atomic clock might report fractional instabilities $\sigma_y(\tau)$ at the 10^{-18} level after a few hours of interrogation, assuming fractional uncertainties $\delta f/f = 10^{-14}$ and $N \sim 10^3$ atoms per run. Since current molecular clocks probe fewer particles, we need comparatively better linewidths to achieve a competitive precision in reasonable interrogation times.

1.3.1 Limitations to clock stability

Ultimately in clocks, the fundamental limit is set by the quantum projection noise (QPN), an instability that emerges in population measurements [16]. In ideal cases, QPN should be the dominant noise contribution [16], limiting the precision of your clock. QPN exists in any detection, that is, for example, when the quantum superposition state of an atom or molecule is projected onto the ground or excited state [17]. It arises from the fundamental indeterminate nature of a quantum system measured in a particular state, in accordance with the Heisenberg uncertainty principle (see figure 1.1). As we will see later, in addition to these fundamental noise limitations, we need to

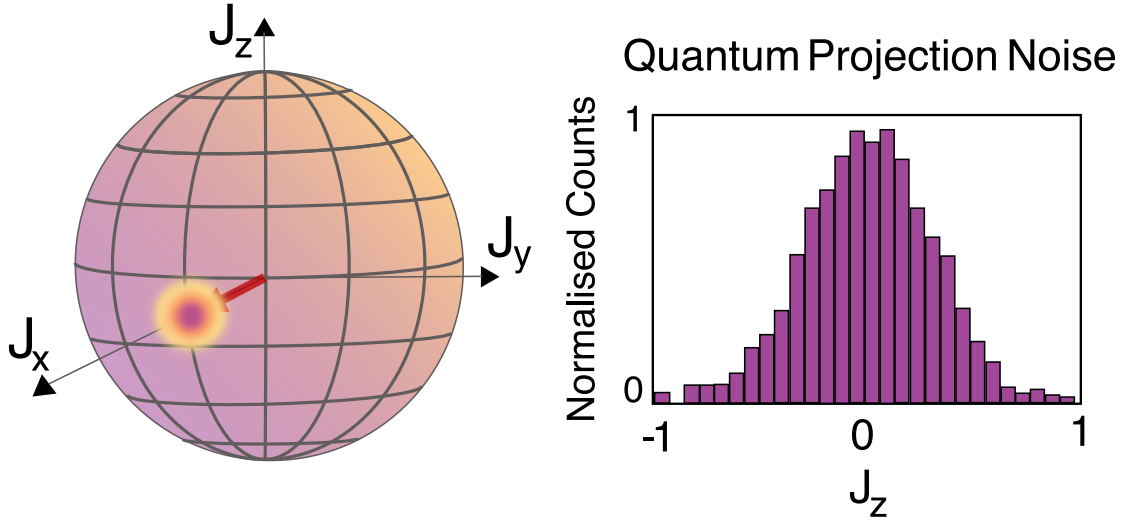


Figure 1.1: Visual representation of quantum projection noise (QPN) associated with a measurement along the J_z axis of the Bloch sphere. The red arrow shows the state position, while the rainbow shaded region shows the spread associated with the noise of the measurement (left). A sample measurement of a projection along the J_z component of the angular momentum is shown (right). This figure is adapted from [15].

carefully account for systematic errors and imperfections that cause frequency drifts in our system.

In large part, our clock stability is a reflection of the linewidth of the clock transition that we are able to achieve. This linewidth is determined by a number of technical and atom/molecule specific factors and is intimately related to the lifetime of atoms or molecules in a particular state:

$$\Gamma_{\text{clock}} = \frac{1}{\tau_{\text{clock}}} \quad (1.2)$$

The lifetime depends first on the natural lifetime of the atoms or molecules in the clock states, which determines how long we can interrogate our system. For instance, if the atomic or molecular lifetime is 0.5 s, then the Fourier-limited linewidth is 2 Hz. On top of the natural lifetime in a given state, other factors can decrease the lifetime of atoms and molecules and, therefore, artificially broaden the linewidth. These factors, which I will discuss at length in the following chapters, include light-induced scattering, thermal inhomogeneous broadening, and interactions and collisions in the trap. Regardless, it is imperative that we preferentially select long-lived clock states with long natural lifetimes to combat this inherent limit.

1.3.2 A note about Q factors

Fundamentally, a molecular clock is a system based on a consistent, robust and stable resonator that is both precise and accurate. One of the ways in which we evaluate the precision of our molecular clock is using the quality factor (Q factor). The Q factor is defined as

$$Q = \frac{f}{\delta f} \quad (1.3)$$

where f is the frequency of the clock transition and δf is its linewidth. Throughout this thesis, I refer to δf as the linewidth of our clock transition interchangeably with the reported uncertainty on our clock transition, depending on the context. We currently hold the record for a molecular clock Q factor of 3.03×10^{12} on a 31 825 183 207 601.1(3.3) Hz transition, achieving linewidths as

narrow as $10.5(1.2)$ Hz (see figure 1.2) [18]. A full description of this record clock measurement is available in KH Leung's thesis [19], but a summary will be presented in chapter 3 of this thesis.

If we consider the fundamental limit set in equation (1.1), we can introduce the Q factor as

$$\sigma_y(\tau) \sim \frac{1}{Q} \frac{1}{\sqrt{N\tau}} \quad (1.4)$$

In this way, the Q factor, as in equation 1.3, is directly related to our ability to reduce the necessary interrogation time of our system at a given precision, and to improve the overall precision of our

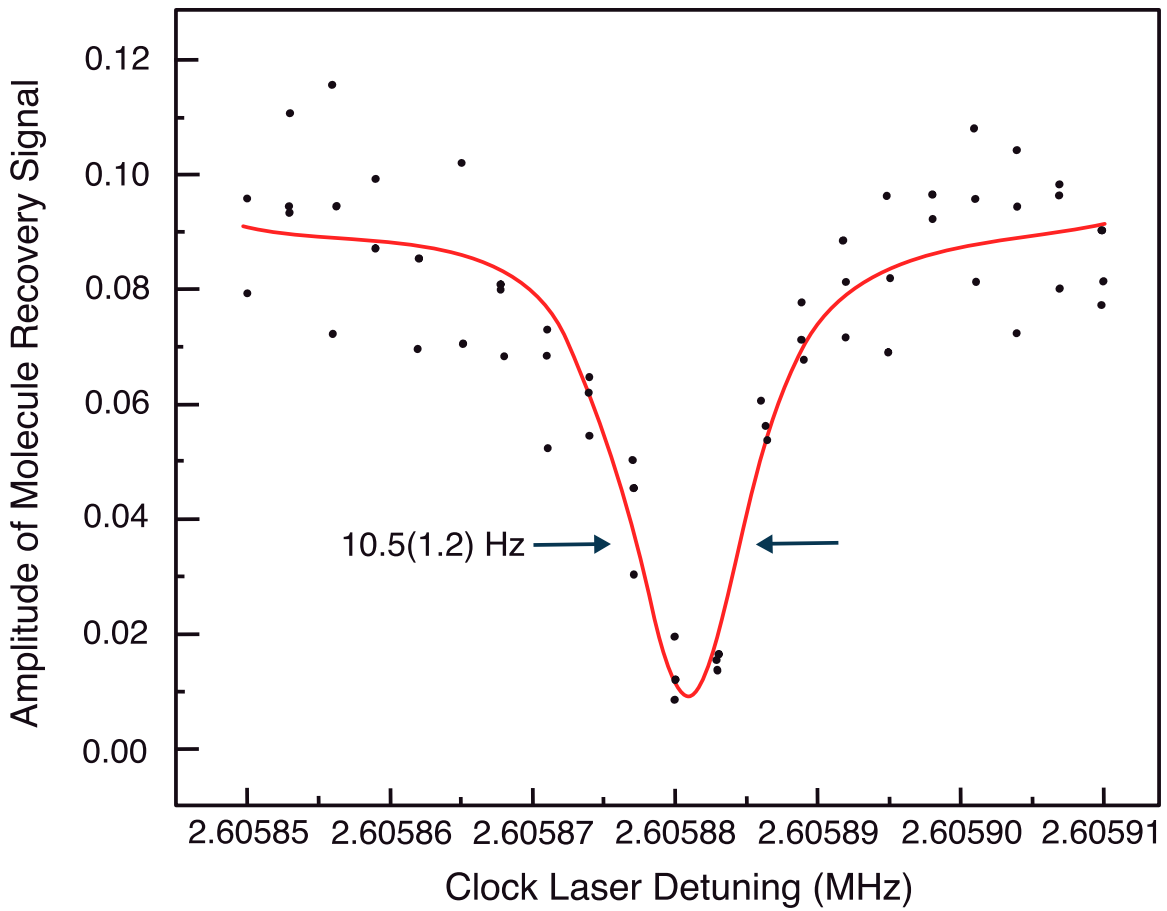


Figure 1.2: An example of a narrow molecular clock transition with $10.5(1.2)$ Hz linewidth δf . This transition is achieved by two-photon spectroscopy via an intermediate state (as shown in figure 1.3). The transition frequency f is equal to $31\ 825\ 183\ 207\ 601.1(3.3)$ Hz, corresponding to a Q factor of 3.03×10^{12} .

clock. Throughout this thesis, I propose pathways towards a next-generation clock for precision measurement. In many cases, I refer to the Q factor as one metric for our clock quality, and in particular will point out potential trade-offs we need to consider when designing a future clock.

1.4 Why $^{88}\text{Sr}_2$ is a good candidate

There are a number of reasons we select $^{88}\text{Sr}_2$ as the basis of our molecular clock. One major advantage of our particular experiment is that we exploit a new type of clock transition. Transitions in our molecule are in the THz frequency range, as compared to atomic clocks, whose transitions are in the optical range; these new clock frequencies allow us to probe new frontiers of physics because they are based on nuclear vibrations rather than electronic transitions.

In atomic clocks, strictly forbidden $^1\text{S}_0$ - $^3\text{P}_0$ transitions in ^{88}Sr are addressed by applying a small magnetic field [20]. For comparison, the natural linewidth of this transition in ^{87}Sr is on the order of mHz [21]. By contrast, in molecular clocks, we address a transition between vibrational states in the ground electronic potential, which is strictly forbidden. The natural linewidth of such a transition is effectively zero, but it is made accessible in our system by using a Raman transition, a 2-photon (2-colour) transition via an intermediate excited state of two allowed transitions (see figure 1.3). As such, ultranarrow, sub-mHz linewidths should be achievable in our system, if we are able to overcome other technical limitations.

These special transitions emerge specifically in homonuclear dimers due to Laporte selection rules [22]. For homonuclear, centrosymmetric dimers, such as $^{88}\text{Sr}_2$, we can define whether a state or potential is *gerade* (g) or *ungerade* (u) which indicates the parity with respect to inversion about the centre. *Gerade* states have even parity, $\psi(-r) = \psi(r)$, while *ungerade* states have odd parity, $\psi(-r) = -\psi(r)$ [22]. The Laporte rule forbids electronic transitions that conserve parity. Allowed transitions in such molecules must involve a change in parity, in other words, either $\text{g} \rightarrow \text{u}$ or $\text{u} \rightarrow \text{g}$. Since all vibrational states in the electronic ground potential, $\text{X}^1\Sigma_g^+$ of $^{88}\text{Sr}_2$ are *gerade*, transi-

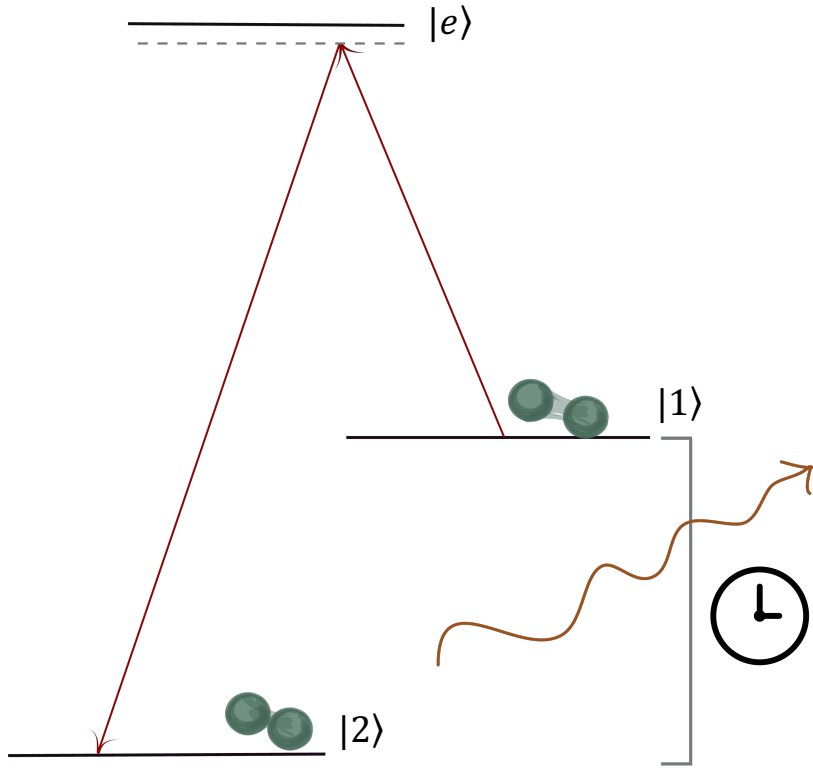


Figure 1.3: A simplified cartoon of our molecular clock system. The clock resonator is a transition between two vibrational states, $|1\rangle$ and $|2\rangle$, in the ground electronic potential $X^1\Sigma_g^+$. This transition is strongly forbidden since $g \rightarrow g$ transitions, which do not involve a change in parity, are Laporte forbidden. The transition is, therefore, accessed via an intermediate excited state $|e\rangle$ and two allowed transitions.

tions between these are Laporte forbidden.

States in the ground electronic state have even total angular momentum, and, in particular, we work with transitions between clock states that both have total angular momentum $J = 0$; these states are particularly desirable, since they are highly insensitive to magnetic fields. We know that these transitions are generally accessible with current laser technology with the majority of the clock probe laser and lattice wavelengths of interest found in the red or near-infrared range (be-

tween ~ 700 - 1100 nm).

It is important to note that Sr atoms have been studied extensively and are the basis for a number of high-precision atomic clocks. The cooling and trapping schemes, as well as the atomic structure, are well-studied and well-modelled with theory. This precedent provides a wealth of useful information for our own work. All told, $^{88}\text{Sr}_2$ presents a promising platform for a new type of metrological system, whose technical limitations rival those of atomic clocks.

1.5 Searches for New Physics

There are a number of applications for precision measurement of $^{88}\text{Sr}_2$ including tests for temporal drift of fundamental constants, sometimes referred to as μ -dot or α -dot tests, investigations into ultracold collisions and ultracold quantum chemistry, and searches for a fifth force or corrections to gravity. In this thesis, I focus primarily on proposed methods to place constraints on non-Newtonian gravity at nanometer scales, although much of the work promises the potential for other fundamental tests and provides a window into the quantum chemistry of our molecule. In particular, much recent focus has been placed on using Yukawa-type corrections to Newtonian gravity at short separations [11, 23], that is, the addition of a term $V_{\text{Yukawa}}(r)$ to the conventional Newtonian gravity $V_{\text{Newton}}(r)$ such that the gravitational potential between two point masses is

$$V(r) = V_{\text{Newton}}(r) + V_{\text{Yukawa}}(r) = -\frac{Gm_1m_2}{r}(1 + \alpha e^{-r/\lambda}) \quad (1.5)$$

where λ is called the range of the Yukawa potential, characterising the distance scale at which the effects of the correction become important, and α is an overall scale factor, the size of the correction. This correction impacts the depth of our molecular potential, and, therefore, precision measurements of this depth can provide insight into the size of this term.

Such corrections are a consequence of many extensions to the Standard Model, and arise due to

hypothetical light elementary particles or in extra- and compactified dimensions [24]. In this way, precision measurements of these constraints are integral to providing insight into these Beyond-the-Standard-Model theories, and motivate the work we present here.

In this thesis, I will first lay the groundwork for a molecular clock experiment (Chapter 2), describe the current state-of-the-art molecular clock (Chapter 3), and discuss scientific and technical directions for improved precision (Chapter 4). In the last chapter (Chapter 5), I project the precision required for a meaningful fifth-force measurement as motivation for our push towards a second-generation molecular clock. While there are benefits from pursuing ever-better quantum and technical control of our molecules, in this thesis, I also discuss the motivations for these improvements, specifically towards a high-precision measurement of constraints to Yukawa-type corrections to gravity at nanometer scales.

Chapter 2: Laying the Groundwork for a Highly Controlled Metrological System

When building a precise molecular clock, we need to have a thorough understanding of our molecule and our system. Here, I introduce our experiment and describe previous work that led to our first clock campaign. In particular, I focus on previous measurements, which allowed us to achieve higher resolution spectroscopy, quantum control and precise state selection and long lifetimes. Each of these milestones is crucial in laying the foundation for a high-precision frequency measurement.

2.1 Making Ultracold $^{88}\text{Sr}_2$

Theoretical modeling of the electronic potentials of $^{88}\text{Sr}_2$ allows us to estimate and predict the behaviour of our molecules. Much of the work in this thesis involves testing the validity of current quantum chemistry models against experiment; these models, in turn, are crucial to inform our experimental direction and guide future decisions. A bulk of this theoretical work is produced through collaborations with the Quantum Chemistry Laboratory at the University of Warsaw, specifically under the guidance of Robert Moszyński¹. The details of the theoretical work relevant to this thesis are primarily reported on in I. Majewska’s thesis [25]. Here, I will focus on the more relevant information.

Strontium dimers are a relatively simple molecule from a quantum chemistry perspective. For one, there is no hyperfine structure since the nuclear spin of ^{88}Sr is $I = 0$ [26]. Spin statistics forces the molecular wave function to be even upon the exchange of the bosonic nuclei in $^{88}\text{Sr}_2$. In

¹robert.moszynski@gmail.com

most of our work, we focus on transitions between the electronic ground state $X^1\Sigma_g^+$ — referred to throughout as X_g — and the singly excited Hund’s case (*c*) potentials $(1)0_u^+$ and $(1)1_u$ — referred to throughout as 0_u^+ and 1_u — that correspond to the 1S_0 - 3P_1 dissociation limit in the ^{88}Sr atom (see figure 2.1) [27]. We refer to individual states of our molecules as $X_g(v, J)$ (or in the corresponding excited potential) using the vibrational quantum number, v , and the total angular momentum J . Note that we interchangeably refer to weakly bound states by counting up from the ground state or counting down from threshold; that is, the least-bound state in the ground potential can be written as $X_g(62, 0)$ or by counting down as $X_g(-1, 0)$.

Our primary objective is to create a sample of ultracold ^{88}Sr dimers, but direct laser cooling of molecules can be incredibly challenging due to the complexity of their internal structure [28]. Therefore, in our lab, we opt to create molecules by laser cooling atoms as building blocks for our molecules. We cool our atoms via a conventional two stage magneto-optical trap (MOT) sequence to achieve a $\sim 2 \mu\text{K}$ ultracold atomic sample. We first cool and trap on the primary 1S_0 - 1P_1 blue MOT transition, with two additional repumps on the 3-P state, before transferring to the red MOT, performing narrow-line cooling on the $\sim 7 \text{ kHz}$ 1S_0 - 3P_1 transition. Once we have a red MOT, we transfer our atoms into a horizontal, 1D optical lattice. This cooling and trapping scheme is well-established and details can be found in C. Osborn’s thesis [29].

From these atoms trapped in a lattice, we create molecules in the electronic ground state via photoassociation of atom pairs. Specifically, we address the $1_u(-1, 1)$ state in the molecular excited potential, which strongly spontaneously decays to $X_g(-1, 0/2)$, the least-bound state; as such, we preferentially form weakly-bound molecules in the ground state. These weakly-bound molecules are the starting point for any experiment we perform in our lab. A visual depiction of our scheme for the cooling, trapping, and creation of our strontium dimers is shown in figure 2.2. A more detailed description of our molecule production is available in C.-H. Lee’s thesis [30].

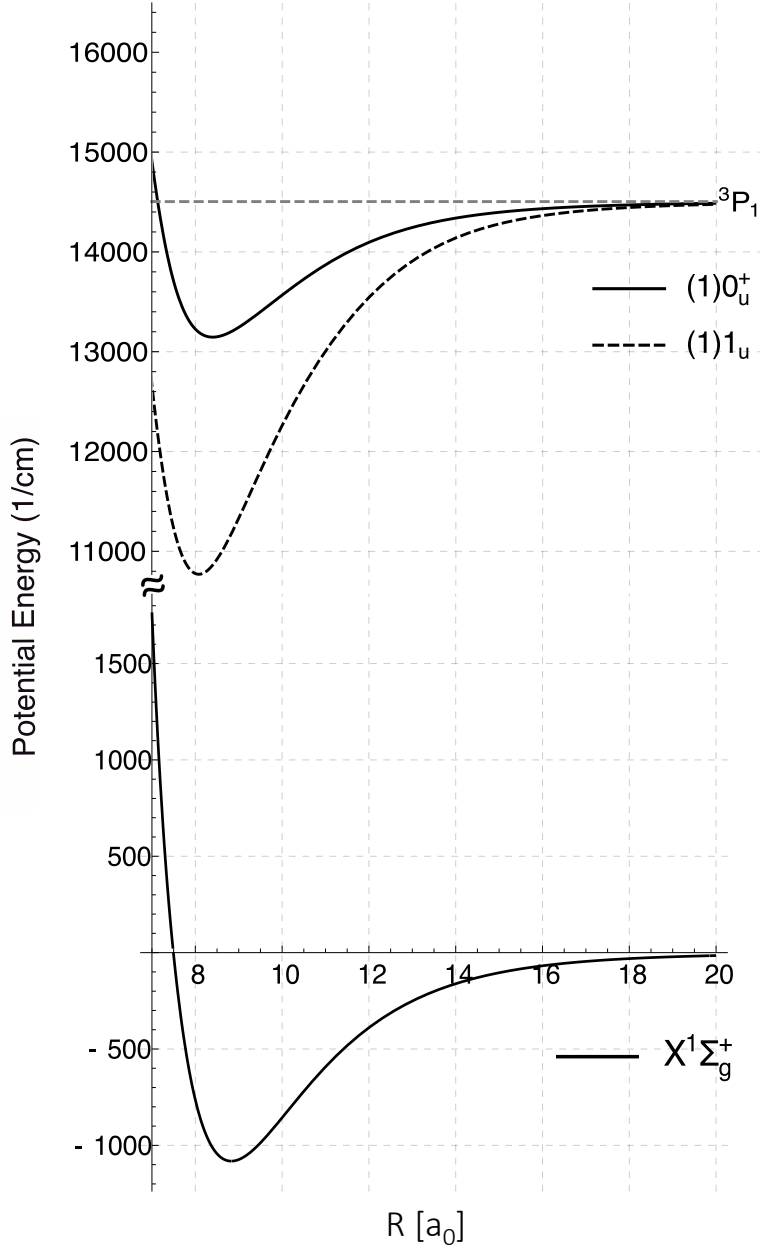


Figure 2.1: A subset of the molecular potentials in $^{88}\text{Sr}_2$. The ground state potential, $X^1\Sigma_g^+$, is taken from empirical data of the strontium dimer [31]. Also shown are the two most relevant excited Hund's case (c) ungerade potentials, 0_u^+ and 1_u , corresponding to atomic $^1\text{S}_0$ - $^3\text{P}_1$ dissociation energy. Models of these excited potentials are fit near-threshold to experimental data of weakly bound binding energies [20]. Adapted from [25].

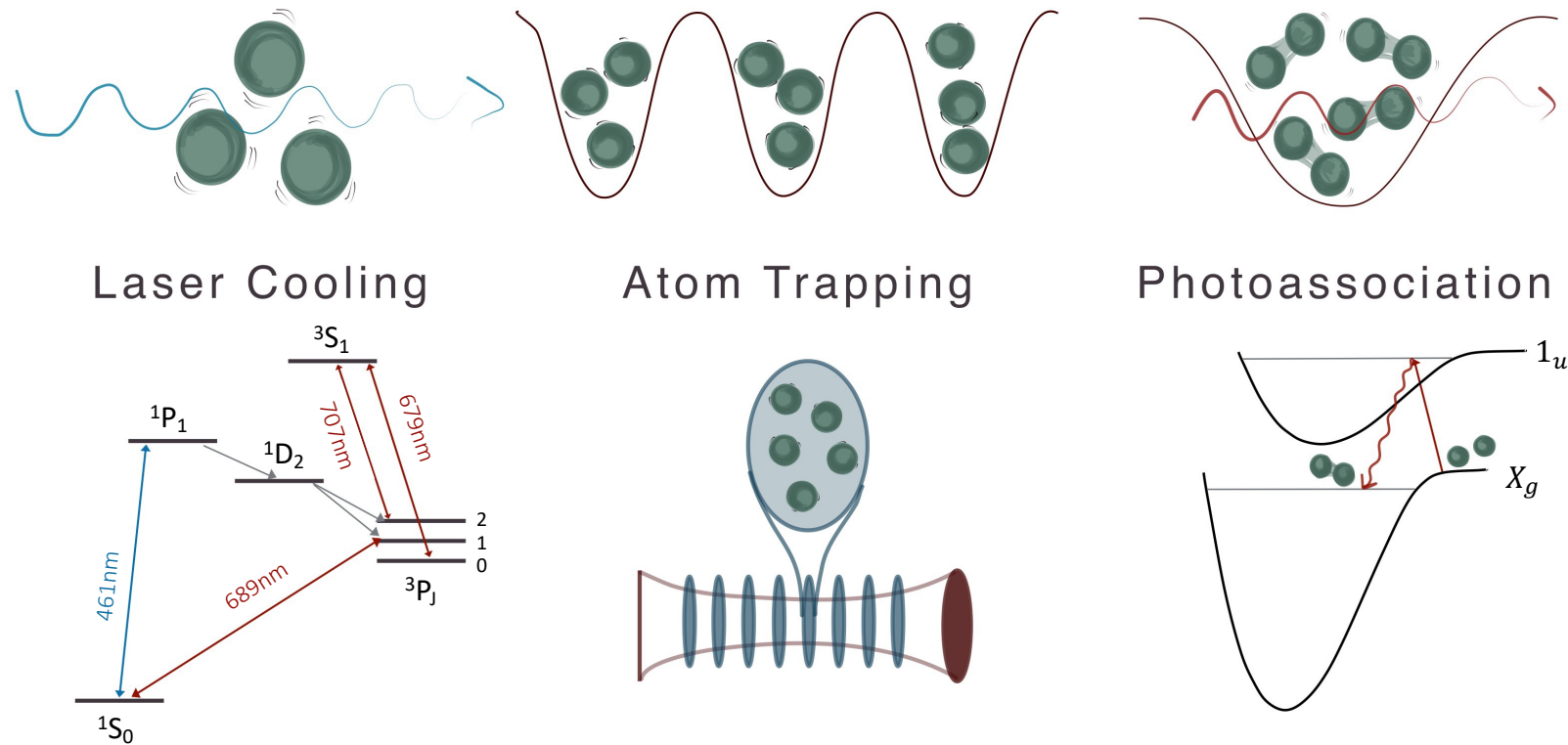


Figure 2.2: Simplified schematic of the process of forming $^{88}\text{Sr}_2$ from cooled ^{88}Sr atoms, chronologically from left to right. ^{88}Sr atoms are first laser cooled using a conventional two-stage MOT scheme. The blue MOT addresses the $^1\text{S}_0 - ^1\text{P}_1$ transition, while the red MOT addresses the narrow-line $^1\text{S}_0 - ^3\text{P}_1$ transition. We perform repumping on the 3-P states. The atoms are subsequently trapped in a 1D optical lattice. Trapped atoms are photoassociated to weakly bound molecules by coupling the atoms to the $1_u(-1,1)$ state in the excited molecular potential. This state preferentially decays to the least bound, $X_g(62,0)$ or $X_g(-1,0)$, state in the molecular ground, X_g potential.

From the least-bound state, we can address any number of vibrational states in the ground potential, X_g , and in the excited potentials, primarily 1_u and 0_u^+ . Regardless of the particular experimental run, for ease, we always measure the population in the least-bound state, $X_g(-1, 0)$. Specifically, after completing a particular experiment of interest, we photodissociate our least-bound molecules to atoms by coupling the $X_g(-1, 0)$ state to the $0_u^+(-1, 1)$ state. We perform absorption imaging on the primary, blue MOT cooling transition of the atoms to measure the number of molecules remaining in the least-bound state after our experiment (see figure 2.3). We measure molecule fragments from both $X_g(-1, 0)$ and $X_g(-1, 2)$, with higher momentum states spreading out more quickly on the camera after a finite time of flight. While we typically work with nearly equal mixtures of $J = 0$ and $J = 2$ ground state molecules, we can perform a purification step that removes the $J = 2$ molecules from our sample. In this way, we demonstrate high levels of specific quantum control of our system, which is crucial when building a reliable molecular clock.

2.2 State-Insensitive Trapping

2.2.1 Mechanism of magic trapping

State-insensitive trapping, also known as magic trapping, is essential for narrowing the linewidth of our clock transition and, in so doing, increasing the overall Q factor of our clock [32]. Holding atoms or molecules in a magic trap mitigates lattice induced light shift arising due to fluctuations in both intensity and frequency, which can artificially broaden the line.² State-insensitive trapping relies on selecting a magic lattice wavelength where the two states of interest — in our case, our two clock states — have the same polarizability. States at two different polarizabilities will experience different trap depths and, as a result, inhomogeneous broadening of the clock transition. By contrast, in a magic lattice, the ac Stark shift has no effect on the transition frequency between the two clock states [33, 34].

²I will further discuss in chapter 3 how, in our system, we cannot perfectly eliminate the effect of the lattice because of higher-order hyperpolarizabilities. However, we can significantly suppress these effects with very-near-magic lattices.

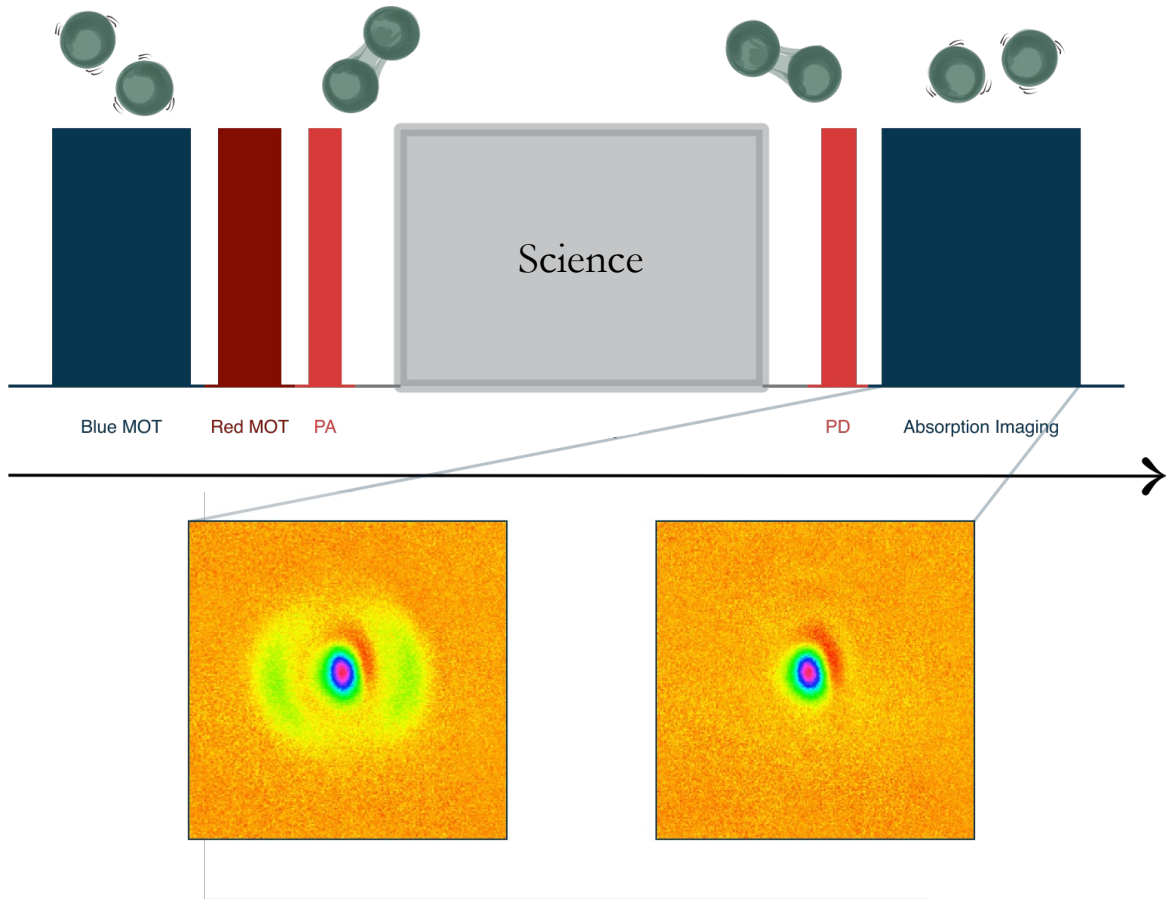


Figure 2.3: Our operational experimental protocol. Shown above is a cartoon representation of our sequence including two-stage blue and red MOT cooling and trapping, photoassociation (PA) of atoms to molecules, photodissociation (PD) of molecules back to atoms, and absorption imaging of atomic fragments on the 461 nm atomic transition. Shown below are examples of our absorption images after photodissociation of molecules in $X_g(-1, J = 0, 2)$. Ordinarily both $J = 0$ and $J = 2$ molecules are visible (left). $J = 2$ molecules, with larger momentum, appear as a ring around $J = 0$ molecules due to the finite time of flight during imaging. We can selectively remove $J = 2$ molecules from our sample (right).

In a non-magic lattice, the two clock states will experience thermal broadening due to their residual temperature and perceived trap differences. The linewidth is related to the temperature by

$$\Gamma_T \sim \left(\sqrt{\alpha_1/\alpha_2} - 1 \right) \frac{k_B T}{0.295 h} \quad (2.1)$$

where $\alpha_1 > \alpha_2$ are the polarizabilities of the two clock states [35]. We can fit the functional form $(\Gamma_T)^2 e^{-u\Gamma_T}$, where $u = h/k_B T \left(\sqrt{\alpha_1/\alpha_2} - 1 \right)$, to this asymmetric line shape, in order to estimate the temperature of our sample, or alternatively, to quantify the polarizability mismatch of our two states. When we approach the magic wavelength, such that $\alpha_1/\alpha_2 \rightarrow 1$, this asymmetric broadening is minimized. As we scan across the resonance, the width of the clock transition drops by a over three orders of magnitude (see figure 2.4) [32], with potential to narrow the line even further. Therefore, matching polarizabilities of clock states is essential as a first step towards achieving a

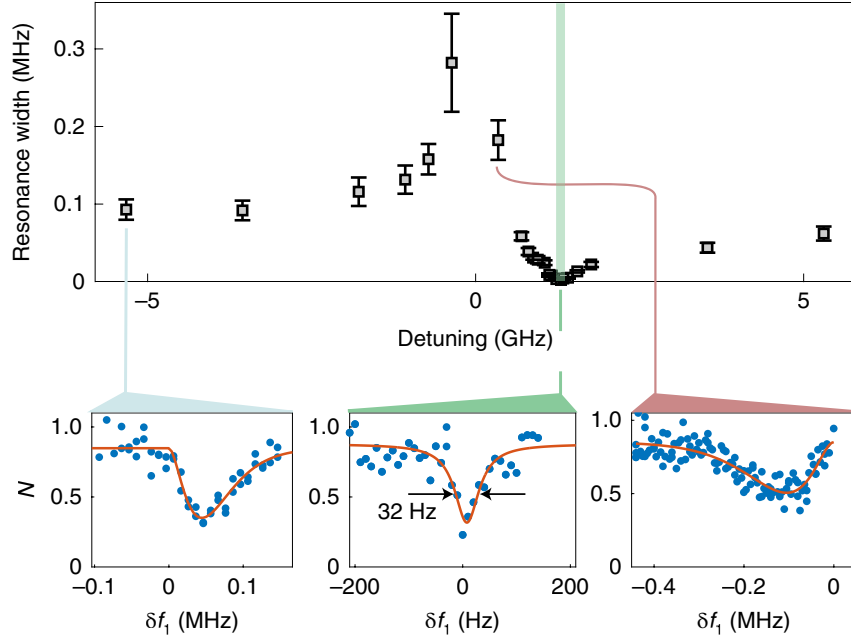


Figure 2.4: The resonance width of a Raman transition, a 2-photon transition via an intermediate state, at various lattice frequencies. The linewidth shrinks dramatically near magic, where lattice-induced and thermal asymmetric broadening are minimized (above). A sample set of the transition spectra at various lattice wavelengths (below). At magic, we find a trace showing a 32(3) Hz linewidth, more than three orders of magnitude narrower. Adapted from [32].

narrow linewidth on our transition.

2.2.2 Finding magic wavelengths in our molecular clock

In our system, we implement state-insensitive trapping by using the lattice to couple our deeply-bound clock state to a deeply bound 1_u vibrational level. As we tune the lattice near a 1_u resonance, the polarizability of the deeply-bound state follows a dispersive behaviour and a zero-crossing point with the weakly-bound clock state is induced (see figure 2.5). In order to determine the magic wavelength, we record the location of the peak centre at high and low lattice intensity (see figure 2.6) [32]. As we approach the magic wavelength, the location of the peak centre should become less sensitive to changes in the lattice intensity. Any lattice induced light shifts are amplified at larger trap intensities; when the difference between the two peak positions, or differential light

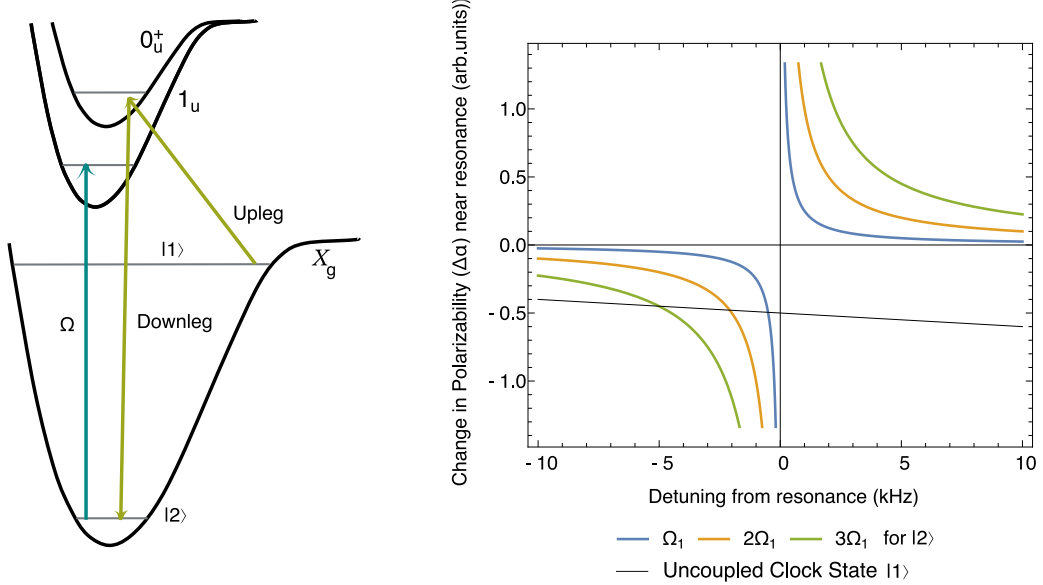


Figure 2.5: Mechanism for magic trapping. We implement a magic wavelength lattice for our Raman spectroscopy of two states in X_g (green) by coupling our lattice (blue) between the deeply-bound state and an excited state in 1_u (left). By tuning near resonance, we induce a dispersive behaviour in the polarizability of the deeply-bound clock state of the form $\Omega^2/4\delta$ modeled here for Ω_1 , $\Omega_2 = 2\Omega_1$ and $\Omega_3 = 3\Omega_1$ (right). This dispersive change in polarizability facilitates a zero-crossing point with the polarizability of the uncoupled, weakly-bound clock state.

shift, is zero, we are at the magic wavelength.

It is important to note that, since we are working near trap-induced resonances, there is a steep dependence of the differential light shift on lattice frequency, often many orders of magnitude more sensitive to lattice frequency than for atomic lattice clocks. For our current clock scheme, for instance, we expect ~ 1 Hz differential light shift per ~ 10 kHz lattice light shift, compared to the expected ~ 1 Hz differential light shift per ~ 1 GHz expected in atoms [32, 36]. Since we have much more restrictive constraints on lattice stability, it becomes increasingly imperative that we have absolute control over lattice frequency in order to mitigate these effects. Regardless, we can stabilise the frequency of our lattice at the magic wavelength by locking our lattice frequency either to our wavemeter (High Finesse WS7-60) or to our frequency comb (Menlo FC1500-250-ULN). While locking our lattice to the wavemeter as a reference, we can achieve linewidths on the order of \sim kHz with the addition of other methods of frequency stabilisation (ie. of the probe lasers). We can further narrow our clock transition down to the Hz-level by additionally locking our lattice to the frequency comb.

2.3 Preferential State-Selection for Magic Trapping

2.3.1 Understanding magic detunings

By design, the magic wavelengths we use in our molecular clock are constructed by parking the lattice near a transition between a deeply-bound clock state and a 1_u state. These near-resonant magic traps are, by nature, very sensitive to lattice detuning and frequency instability. Furthermore, the lifetime of molecules in this state is limited by lattice light-induced scattering near the resonance. The scattering rate near a transition is given by [37]

$$R_{sc} = \frac{\Gamma}{2} \frac{\Omega^2/2}{\Omega^2/2 + \delta^2 + (\Gamma/2)^2} \quad (2.2)$$

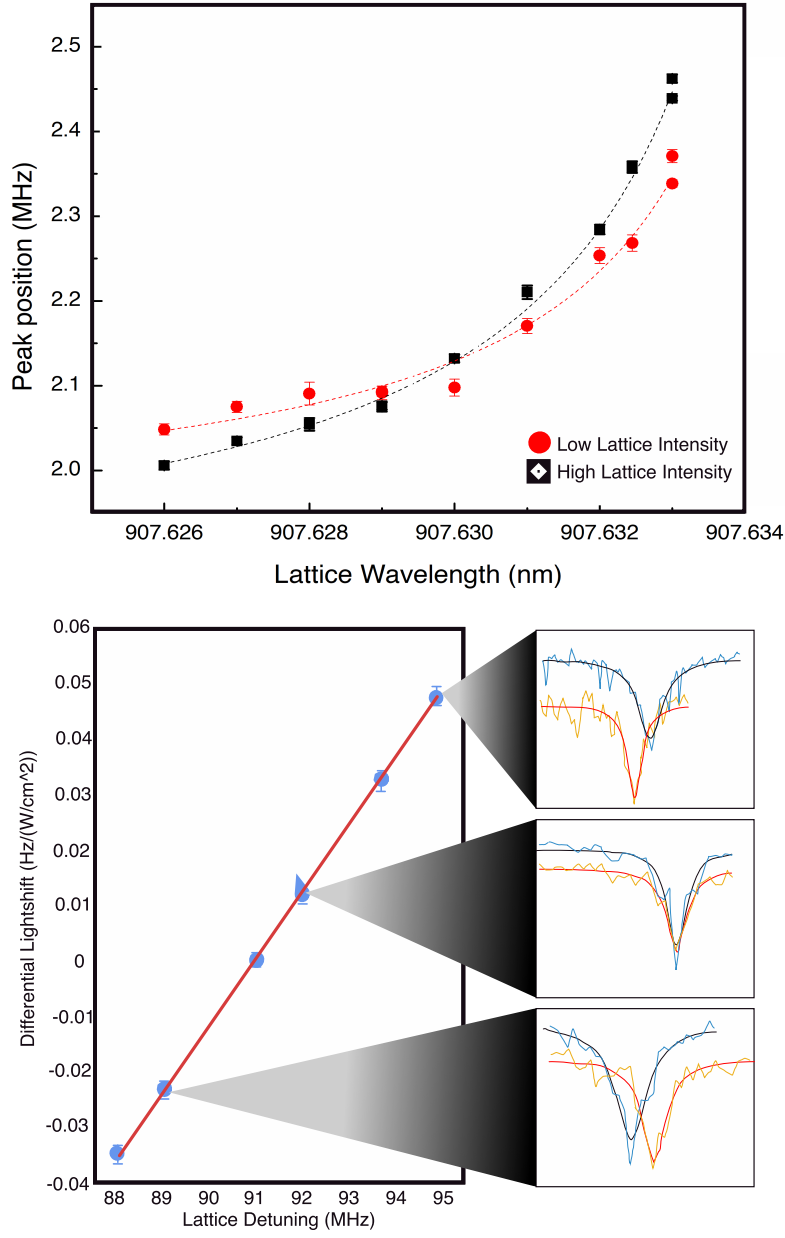


Figure 2.6: Finding magic lattice wavelength from transition peak centres at high and low lattice intensities. Above we plot individual peak positions fitting a dispersive curve (dashed) of the form $A/(x - x_0) + B$ to describe the polarizability behaviour (above). The region where the two fits intersect corresponds to the region where the magic condition is likely to be met. To quantify the magic wavelength, we plot the differential light shift, as in the shift in peak position between the high lattice and low lattice intensities (below). Sample datasets of individual peak traces show the transition in a high intensity lattice (black) as compared to the transition in a low intensity lattice (red) (right). We infer the magic wavelength by fitting a line to the differential light shift and predicting where it crosses zero.

where Γ is the natural linewidth, Ω is the Rabi frequency, and δ is the detuning from the transition.

If we assume that $\delta \gg \Gamma, \Omega$, as is the case in our clock transitions, we can write [30]

$$\tau_{sc} = \frac{1}{R_{sc}} \sim \frac{4\delta^2}{\Gamma\Omega^2} \quad (2.3)$$

As described in section 1.3.1, the lifetime of our molecules dictates the minimum linewidth we can achieve on our clock transition. The magic detuning, δ , is correlated to the lifetime such that larger detunings from resonance result in less scattering, and in longer-lived molecules.

The magic detuning can be seen as an indicator of how forgiving our system is to fluctuations of the lattice. The steeper the slope of the light shift, or the closer we sit to a particular resonance, the more susceptible we are to small frequency changes in the lattice. As such, we preferentially select 1_u excited states whose corresponding magic detunings sit further from resonance. This reduces the lattice-induced scattering of molecules, and scattering-related losses, extending the lifetime of our molecules and increasing the overall Q factor of our clock.

2.3.2 Electric-dipole transition strengths in molecules

In order to preferentially select 1_u states, we must first better understand how strongly these states couple to clock states. In a two-level system, the electric dipole line strength, S , is defined as

$$S_{12} = |\langle 2|er|1\rangle|^2 \quad (2.4)$$

It is important to note that transition strengths are inextricably linked to polarizabilities, such that the baseline polarizability of a state, α_v^{base} is perturbed near a transition

$$\alpha_v = -\frac{1}{h}\frac{S}{\delta} + \alpha_v^{\text{base}} \quad (2.5)$$

As we will see later, any prediction of polarizabilities improves our understanding of molecular structure, and vice versa. Line strengths are related to the Einstein coefficients, which describe the probability for spontaneous emission and stimulated emission / absorption, A_{21} , B_{21} and B_{12} respectively, as [38]

$$\begin{aligned} A_{21} &= \frac{16\pi^3 v^3}{3\epsilon_0 hc^3} \frac{1}{g_2} S \\ B_{21} &= \frac{2\pi^2}{3\epsilon_0 h^2} \frac{1}{g_2} S \\ B_{12} &= \frac{2\pi^2}{3\epsilon_0 h^2} \frac{1}{g_1} S \end{aligned} \quad (2.6)$$

These Einstein coefficients are intrinsic properties of an atom or molecule, which can be calculated from the state wave functions. In the case of diatomic molecules, the wave function is a product of the electronic and rovibrational components, in the Born-Oppenheimer approximation. For the particular states relevant in our experiment, we are interested in the rovibrational part of the wave function, which can be written as

$$\Psi_{\text{rovib}}(R) = \left| X_{n,\Theta}^{v,J}(R) \right\rangle \quad (2.7)$$

where R is the internuclear distance, n is the electronic quantum number, v is the vibrational quantum number and J is the total angular momentum [39]. The rovibrational wave function is projected onto the internuclear axis in the molecule-fixed frame, Θ . It is important to recall that the molecular electric-dipole moment is naturally described in the molecule-fixed frame, while any applied electric field or probe light will naturally be described in the lab frame. We, therefore, must transform our wave function between frames using a tensor rotation operator in order to calculate the transition strengths between two states under an electric field [40]. In this way, the line strength, or transition strength, for an electric-dipole transition between two rovibrational states described by the wave functions $\left| X_{n,\Theta}^{v,J}(R) \right\rangle$ and $\left| X_{n',\Theta'}^{v',J'}(R) \right\rangle$ is [39]

$$S \equiv \left| H_{J'M'\Theta'}^{JMQ} \left\langle X_{n',\Theta'}^{v',J'}(R) \middle| d_{\Theta'-\Theta}(R) \middle| X_{n,\Theta}^{v,J}(R) \right\rangle \right|^2 \quad (2.8)$$

where $d_{\Theta' - \Theta}(R)$ is the electronic transition dipole moment, and $H_{J'M'\Theta'}^{JMQ}$ are the Hönl-London factors associated with this transformation and are given by³

$$\begin{aligned} H_{J'M'\Theta'}^{JMQ} &\equiv (-1)^{M-\Theta} \sqrt{(2J+1)(2J'+1)} \\ &\times \sqrt{1 + \delta_{\Theta_0} + \delta_{\Theta'_0} - 2\delta_{\Theta_0}\delta_{\Theta'_0}} \\ &\times \begin{pmatrix} J & 1 & J' \\ M & 0 & -M' \end{pmatrix} \begin{pmatrix} J & 1 & J' \\ \Theta & \Theta' - \Theta & \Theta' \end{pmatrix} \end{aligned} \quad (2.9)$$

We can, with the help of our quantum chemistry collaborators, model the wave functions of each vibrational state in X_g , 1_u and 0_u^+ , and subsequently estimate the line strengths, or transition moments, between pairs of states. These models are crucial for future experiment design and clock state selection.

2.3.3 Using line strengths to predict magic detunings

As described in section 2.2, the polarizability of a state near resonance exhibits a dispersive behaviour, where the shape is governed by the expression

$$\Delta\alpha \propto \frac{\Omega^2}{4\delta} \quad (2.10)$$

when $\delta \gg \Omega$. Larger Rabi frequencies, Ω , push this dispersive behaviour further away from the resonance as shown in figure 2.5. The Rabi frequency, Ω , is simply related to the dipole transition moment, d and the applied electric field, E

$$\Omega = \frac{d \cdot E}{h} \quad (2.11)$$

³The Kronecker deltas appear in this equation because it is convention to construct total parity states, that is to construct pairs of states with opposite parity. The inclusion of the Kronecker deltas assures that we adequately double-count these pairs of states [41].

Since the dipole moment, d , can be expressed in terms of the line strength, S , we can rewrite equation 2.11 as

$$\Omega = \frac{1}{\hbar} \sqrt{\frac{2IS}{\epsilon_0 c}} \quad (2.12)$$

where I is the intensity of light coupling the transition, and S is the line strength associated with this transition. In other words, for a given clock state, by coupling it to an excited state with a larger Rabi frequency at the same light intensity — that is to a state with a stronger transition strength — we can engineer a magic condition at a larger magic detuning. If we can adequately model the line strengths for pairs of states in our molecules, we can preferentially select states that allow for these larger magic detunings and longer molecule lifetimes.

We experimentally measure a number of these transition strengths specifically between $X_g(6, 0)$ (one of our first experimentally-accessible deeply-bound clock states) and a number of deeply-bound $1_u(v, 1)$ states. In order to probe the shift in polarizability described by equation 2.10, we perform two-photon Raman spectroscopy from $X_g(-1, 0)$ to $X_g(6, 0)$, detuned from the intermediate state by 20 MHz. We measure the two-photon resonance frequencies at various detunings, δ , which reproduce the expected dispersive behaviour. By fitting to this dispersive shape, we can extract the Rabi frequency and convert these to absolute values of line strength, S [39]. As expected, pairs of states with higher transition strengths give rise to larger magic detunings (see figure 2.7).

Most importantly, by leveraging quantum chemistry models, we can rely on calculated transition strengths alone to predict optimal pairs of states for future clock experiments; these stronger transitions place less stringent constraints on the required frequency stability of the lattice, and allow us to achieve higher overall Q factors. A complete picture of X_g to 1_u transitions is described in figure 2.8.

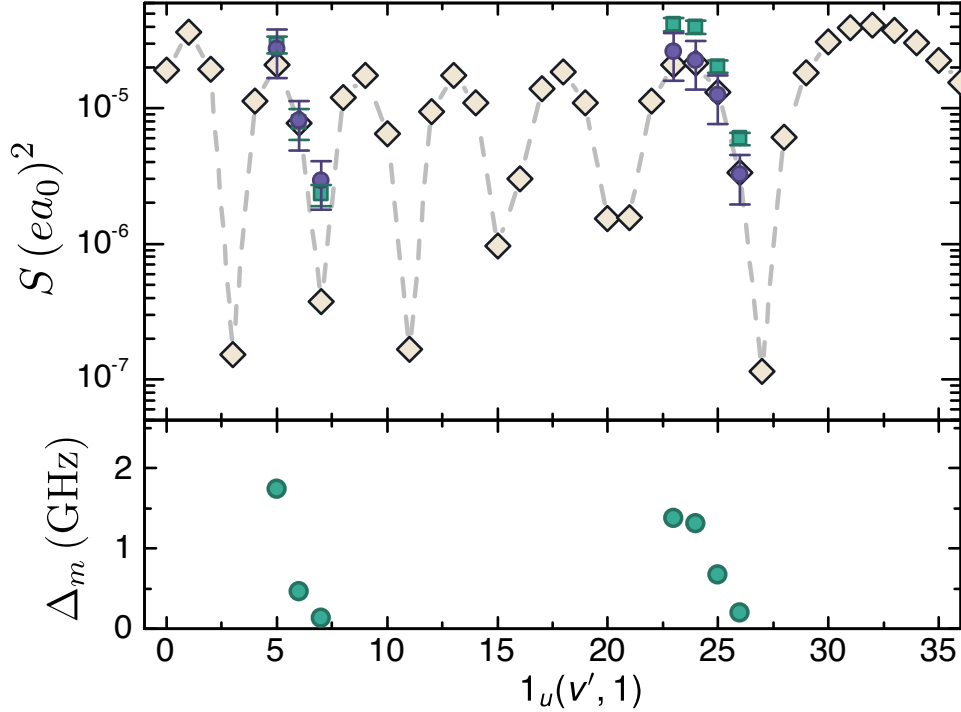


Figure 2.7: Line strengths and corresponding magic detunings for pairs of states from $X_g(6, 0)$ to different $1_u(v, 1)$ states. Larger transition strengths (S) are predictors for larger magic detunings (green circles). We show experimental results obtained using two different approaches to measure the lattice intensity: (1) using direct imaging of beam waist (purple circles) and (2) calibrating to the 1S_0 Sr atomic polarizability (green squares). Theoretical predictions from the Morse potential are shown (yellow diamonds) and trends match behaviour in experiment [39].

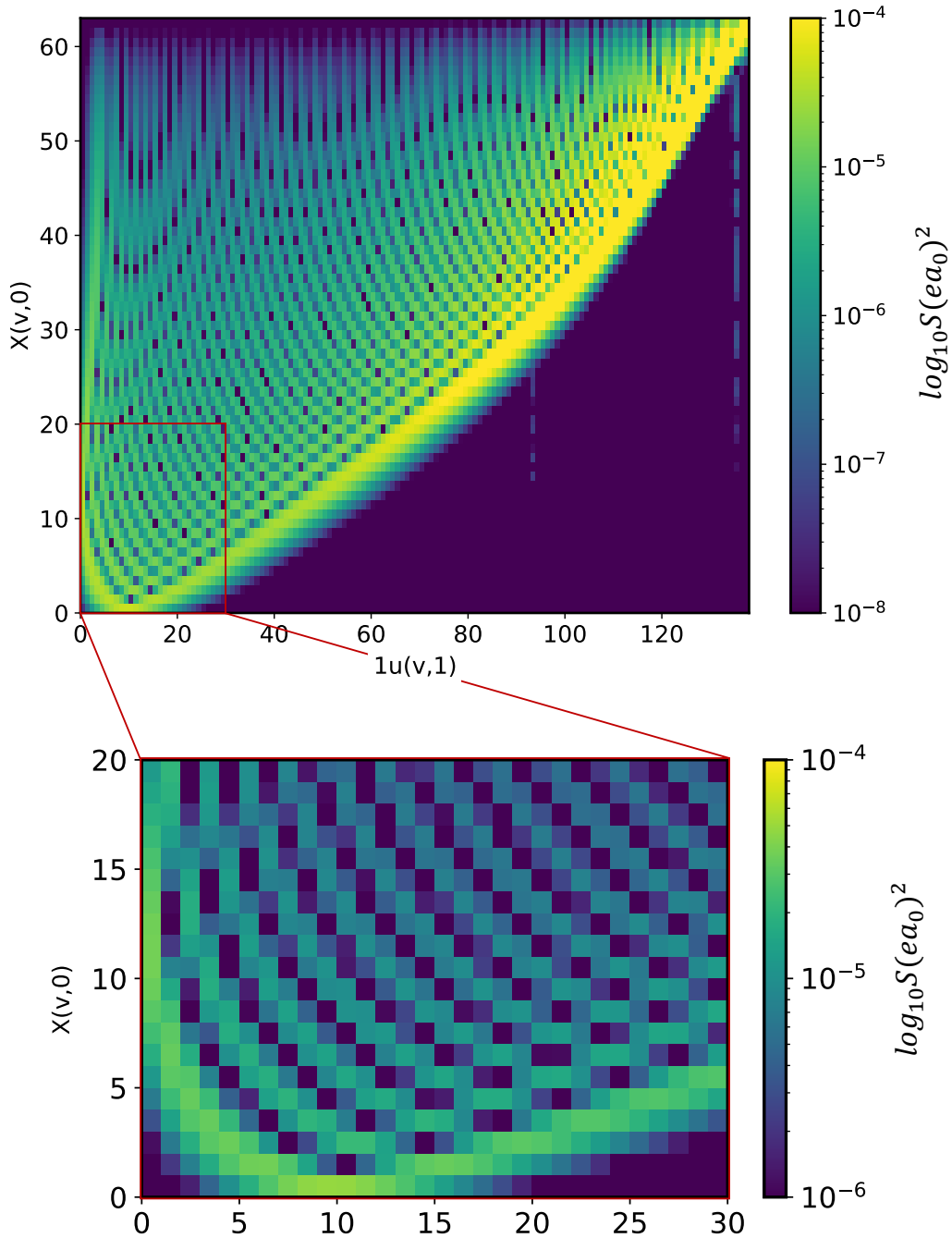


Figure 2.8: Transition strengths for pairs of vibrational states in the X_g and 1_u potentials. Below, we zoom in on a particular region of interest to design magic wavelength traps of possible deeply-bound clock states. Importantly, larger transition strengths offer favourable clock configurations. Note that upper (lower) bounds on colorbars represent the upper (lower) cutoffs for plotted transition strengths, and do not necessarily correlate with global maximum (minimum) values. Adapted from [39].

2.4 Quantum State Control

2.4.1 A complete map of the molecule

One of the other hallmarks of a high-precision clock is the ability to selectively populate specific states of the molecule. In order to achieve this level of control, we perform high-resolution spectroscopy to measure the binding energies of individual vibrational states in the ground and excited potentials.

The energy levels of a rotating vibrator — for a given vibrational state, v , with angular momentum, J , in a potential with electronic quantum number, n — can be described by the Dunham expansion [42, 43]

$$E_{v,J} = \sum_{k,l} Y_{lk} \left(\sqrt{\frac{\mu_0}{\mu_i}} \right) \left(v + \frac{1}{2} \right)^l [J(J+1) - n^2]^k \quad (2.13)$$

where μ_0 is the reduced mass of $^{88}\text{Sr}_2$, μ_i is the reduced mass of another isotopologue, and Y_{lk} are the Dunham parameters for strontium diatoms. Conventionally, we can simplify this expression by defining effective constants ω_e , $\omega_e x_e$, B_e , α_e , and D_e , known as the spectroscopic constants, which correspond to these Y_{lk} s [44]. We can, in turn, fit experimental measurements of the energy levels of the potential, particularly of the more deeply-bound states, as

$$E(v, J) = -D_e + \omega_e \left(v + \frac{1}{2} \right) - \omega_e x_e \left(v + \frac{1}{2} \right)^2 + \left[B_e - \alpha_e \left(v + \frac{1}{2} \right) \right] J(J+1) \quad (2.14)$$

where D_e describes the total potential depth, ω_e describes vibrational splitting of a harmonic oscillator, x_e corrects for the anharmonicity of the potential, and B_e and α_e represent the rotational and vibration-rotation coupling, respectively [45].

Since our clock Raman transition couples two ground potential states to the 0_u^+ potential, we experimentally determine the binding energies of all $J = 0$ vibrational states in the ground potential, and of the first 37 vibrational levels of 0_u^+ . From this study, we determine the spectroscopic

constants for both potentials, which can be found in tables 2.1 and 2.2. A complete evaluation of these critical potentials provides insight into the quantum chemistry of our molecule.

Table 2.1: Extracted spectroscopic constants of 0_u^+ in units of cm^{-1} . They are obtained by fitting equation 2.14 to the 11 most deeply-bound states. Note that since we only measure states of the same angular momentum ($J = 1$), we cannot separate the vibrational and rotational constants when fitting. Theoretical comparisons are from [43].

Spectroscopic constant	This work	Theory [43]
$-D_e + 2B_e$	-2791.21(11)	-2790.90
$\omega_e - 2\alpha_e$	81.032(47)	80.713
$\omega_e x_e$	0.3327(42)	0.2296

Table 2.2: Spectroscopic constants for X_g in units of cm^{-1} . They are obtained by fitting equation 2.14 to the deepest 8 bound states. We measure binding energies of $J = 0$ as well as rotational splittings from $J = 2$ states. Theoretical comparisons are taken from [31, 46].

Spectroscopic constant	This work	Theory [31, 46]
D_e	1081.6395(2)	1081.64(2)
ω_e	40.3210(5)	40.328
$\omega_e x_e$	0.39788(7)	0.3994
B_e	0.017577(6)	0.01758
α_e	$1.75(1) \times 10^{-4}$	1.68×10^{-4}

We spectroscopically locate the most deeply-bound vibrational levels of 0_u^+ , that is for $0_u^+(0, 1)$ to $0_u^+(37, 1)$, via one-photon excitation of molecules in $X_g(-1, 0)$ state. Again, transitions appear as depletion of the recovered atom signal from $X_g(-1, 0)$. Most interestingly, when plotting binding energy versus vibrational state, we observe a change in the trend of the measured binding energies near -1500 1/cm with respect to the ${}^1\text{S}_0 + {}^3\text{P}_1$ threshold, which corresponds to the signature of the spin-orbit perturbation and avoided crossing in 0_u^+ (see figure 2.9). This is of particular interest because it gives the 0_u^+ potential mixed singlet-triplet character, which improves the chances for large Franck-Condon overlap with both weakly- and deeply-bound vibrational levels. Large Franck-Condon factors are essential for easy transfer of our molecules between states.

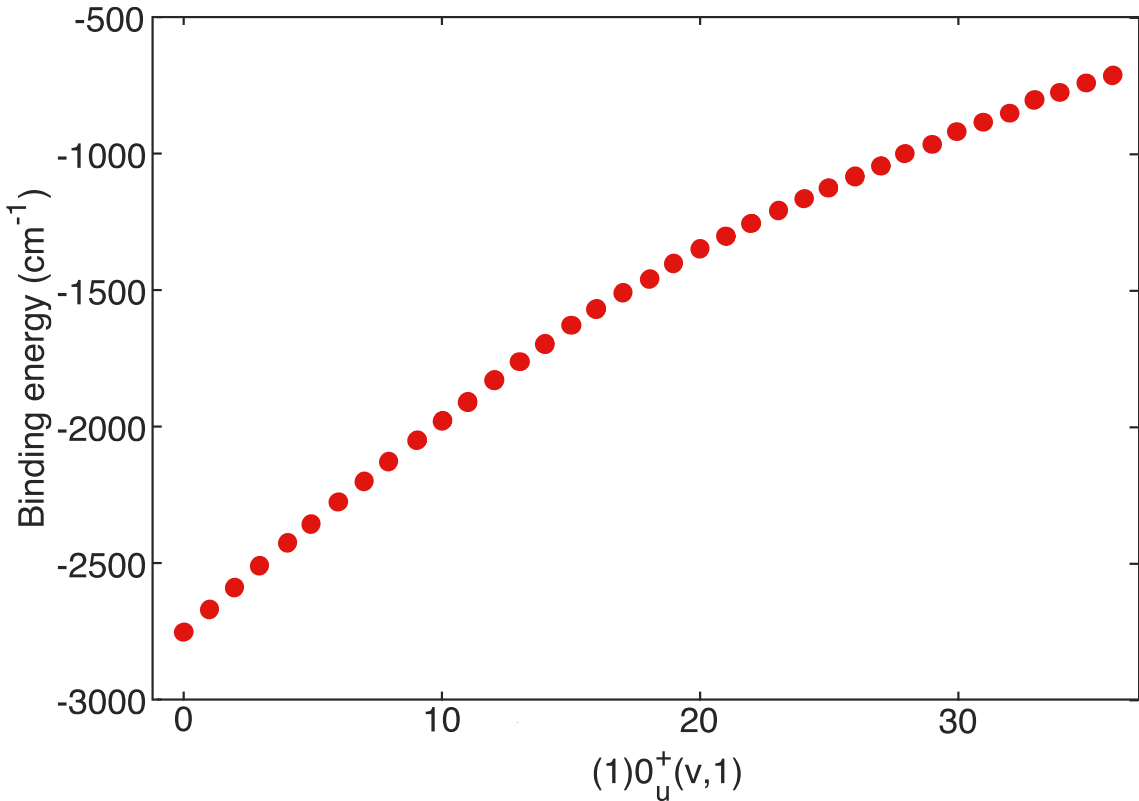


Figure 2.9: The first 37 (most deeply-bound) vibrational levels of the 0_u^+ potential. A kink in the trend near -1500 cm^{-1} is the result of the avoided crossing in 0_u^+ . Binding energies of the deepest 11 states are fit to equation 2.14, from which we extract the spectroscopic constants for the potential in table 2.1. Adapted from [47].

We leverage our measurement of the 0_u^+ potential to perform a complete study of our ground potential. Unlike 0_u^+ states, the states in the ground potential cannot be directly accessed from $X_g(-1, 0)$. We probe these states with 2-photon Raman spectroscopy via an intermediate state in the 0_u^+ excited potential. Specifically, we fix the first leg, or upleg, of our Raman beams on resonance with $0_u^+(11, 1)$, which strongly couples to both legs of the Raman transition, and scan the frequency of our second leg, or downleg, until we see electromagnetically-induced transparency (EIT). EIT is a coherent process that relies on the formation of a dark state, a superposition of the two states, which does not interact with either laser field. As a result, we no longer see depletion of $X_g(-1, 0)$ molecules and, instead, observe a resurgence of the molecule signal. By fixing the

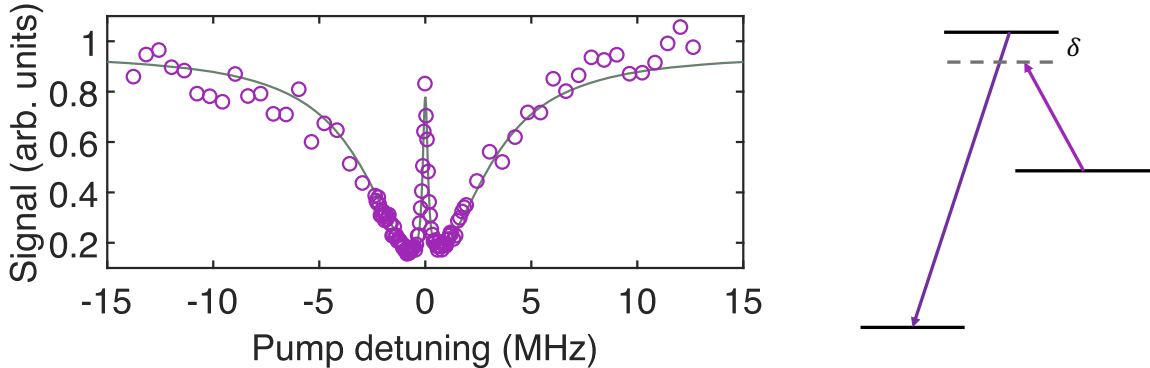


Figure 2.10: Scheme for locating ground vibrational levels. The EIT trace shows recovery of the $X_g(-1,0)$ signal when the detuning of the pump laser is zero (left). This corresponds to the formation of a dark state and indicates that we have located the transition. The two Raman beams are shown in purple (right), where the downleg is fixed on resonance, and the upleg is scanned across the resonance. Adapted from [47].

downleg at this frequency, and scanning the frequency of the upleg laser, we can confirm the EIT signature (see figure 2.10) [47].

Using this technique, we spectroscopically locate all 63 vibrational states of the ground potential for both $J = 0$ and $J = 2$ to an accuracy of $< 0.002 \text{ cm}^{-1}$, which is limited by the accuracy of the wavemeter used to determine the laser frequencies (see figure 2.11). By simultaneously fitting the binding energies and the $J = 0, 2$ rotational splittings of the first 8 vibrational levels, we extract the spectroscopic constants. A complete set of binding energies for both X_g and 0_u^+ is listed in KH Leung's thesis [19]. From this mapping of the ground and excited potentials, we can select states for future clock experiments.

2.4.2 Coherent transfer of molecules

The EIT signature confirms the formation of a dark state that is necessary for coherent transfer of our molecules from one state to another. It is not enough that we can locate each of these states; we want to be able to coherently and controllably transfer our weakly-bound $X_g(-1,0)$ molecules to any other state in X_g . To accomplish this in our experiment, we implement coherent transfer

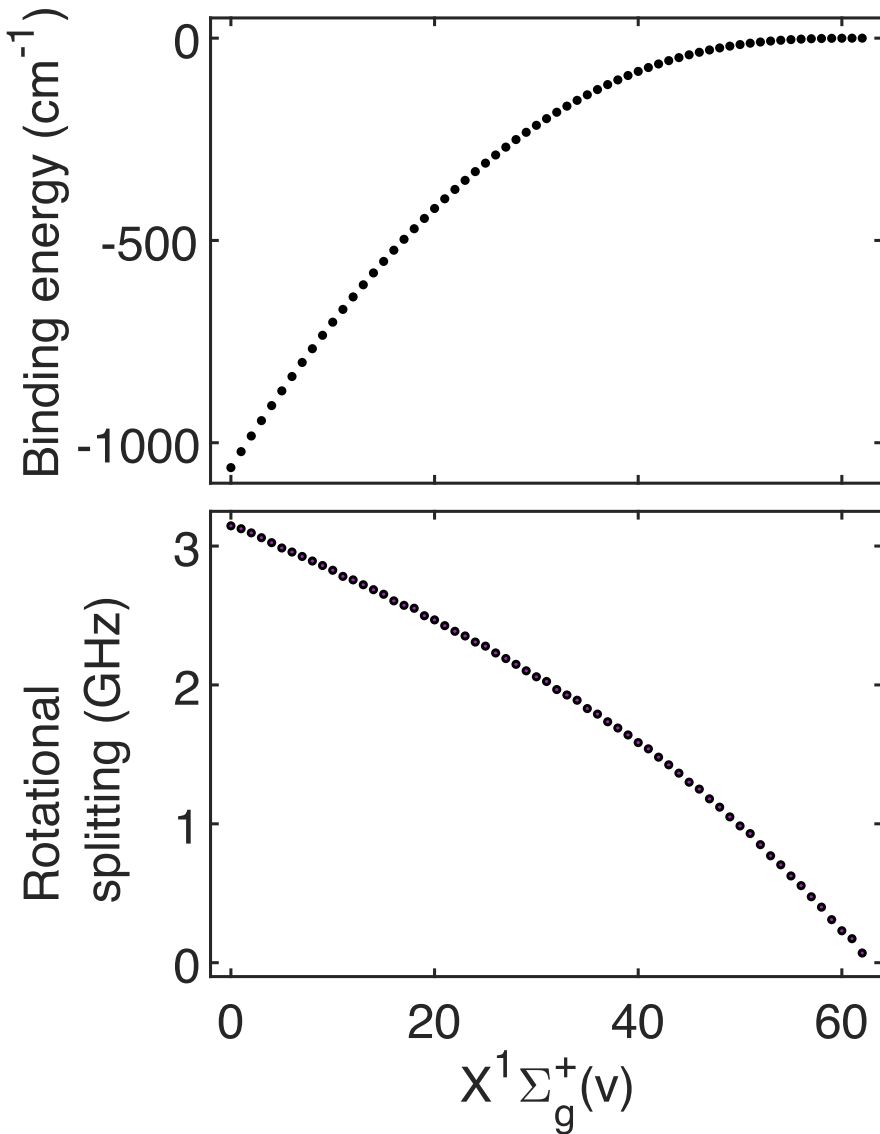


Figure 2.11: A complete map of the ground state X_g potential and rotational splittings between $J = 0$ and $J = 2$. Binding energies fit to equation 2.14 from which we extract the spectroscopic constants for the potential in table 2.2. Adapted from [47].

using a stimulated Raman adiabatic passage (STIRAP) scheme, and we successfully extend the robust state control offered by STIRAP to the entire ground potential of $^{88}\text{Sr}_2$.

STIRAP is a technique for efficiently transferring population between two discrete quantum states by coupling them with two radiation fields via an intermediate state. The STIRAP protocol is advantageous to other transfer schemes because it can (1) reduce loss from spontaneous emission through the intermediate state, and (2) be more robust against small variations in the experiment [48, 49]. In its simplest form in a three-level system, STIRAP allows for transfer from state $|1\rangle$ to state $|2\rangle$ via an intermediate state $|e\rangle$ by using two coherent-radiation fields, referred to as the pump and anti-Stokes lasers, which couple $|1\rangle$ and $|e\rangle$, and $|2\rangle$ and $|e\rangle$, respectively. The hallmark of STIRAP as compared to other transfer mechanisms is the time-dependence of the Rabi frequency of both the pump and anti-Stokes lasers. This eliminates loss from the intermediate state and facilitates smooth transfer of molecules (see figure 2.12) [47].

For coherent transfer within the singlet X_g ground potential, we ideally require intermediate states with marginal triplet admixture that favour strong Frank–Condon overlap with both the initial and final target states, and a narrow linewidth. We predict that these requirements can be satisfied in the vicinity of the 0_u^+ avoided crossing, where transition strengths with mid-to-low-lying states of X_g are predicted to be as large as $100 (ea_0)^2$, while simultaneously maintaining reasonable transition strengths with photoassociated weakly bound molecules [39]. $0_u^+(11, 1)$ offers one of the strongest coupling strengths and is, therefore, chosen as our intermediate state.

In figure 2.12, we show a representative trace of the population of molecules in $X_g(-1, 0)$ during a round-trip STIRAP run. If we assume that the forward and reverse transfer are equally efficient, we achieve one-way transfer efficiencies of $\eta = 89(2)\%$. The round-trip transfer efficiency is quantified as

$$\eta^2 = (N_3 - N_2)/N_1 \quad (2.15)$$

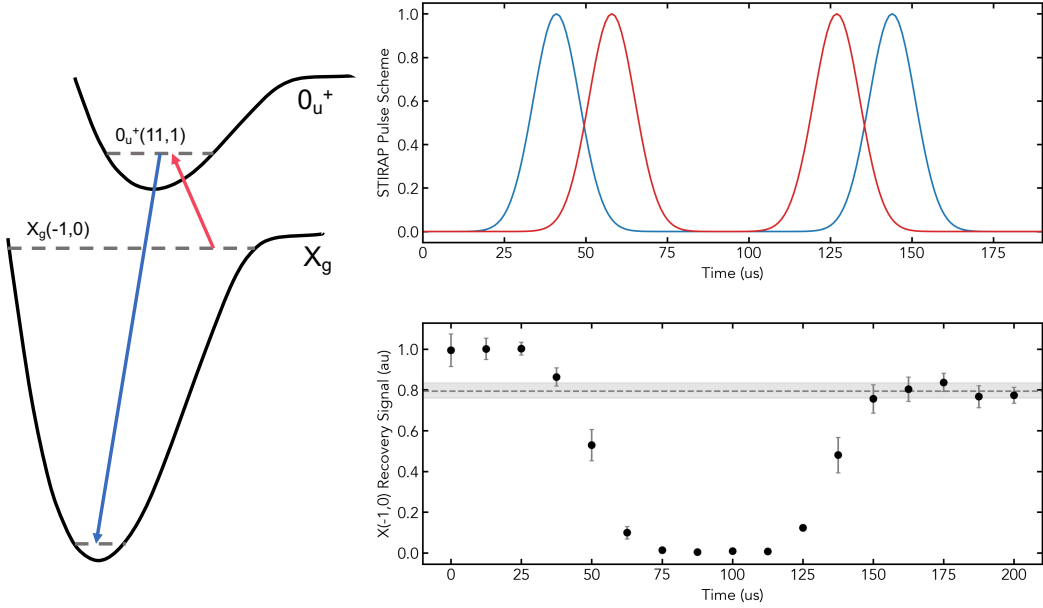


Figure 2.12: STIRAP transfer scheme. Red and blue arrows show the pump and anti-Stokes transfer lasers via the $0_u^+(11,1)$ intermediate state (left). We also show the STIRAP transfer scheme, with the conventional time-dependent Rabi frequencies (above), as well as a sample of the population of $X_g(-1,0)$ as a function of this transfer sequence (below). The one-way efficiency is $\eta = 89(2)\%$.

where N_1 and N_3 are the initial and final molecule number in $X_g(-1,0)$, respectively, and N_2 is the background molecule number in $X_g(-1,0)$ after the forward transfer [39]. Given our typical Rabi frequencies, we normally achieve full extinction such that $N_2 = 0$, except when the detuning of the pump laser is very large.

There are a few challenges in performing efficient STIRAP in our system. First of all, in our current configuration, we do not resolve the Zeeman structure of $0_u^+(11,1)$, making our setup sensitive to any finite relative angle between the polarizations of each of the Raman lasers. In essence, this will lead to an increase in the near-resonant scattering from $0_u^+(11,1)$, which decreases the overall transfer efficiency. We can, however, mitigate this issue by detuning away from the transition (see figure 2.13). STIRAP efficiency is also susceptible to the lattice wavelength and lattice-induced scattering. We can perform STIRAP with molecules in free-flight by temporarily turning off the lattice; the STIRAP protocol is reasonably short and we do not experience significant loss

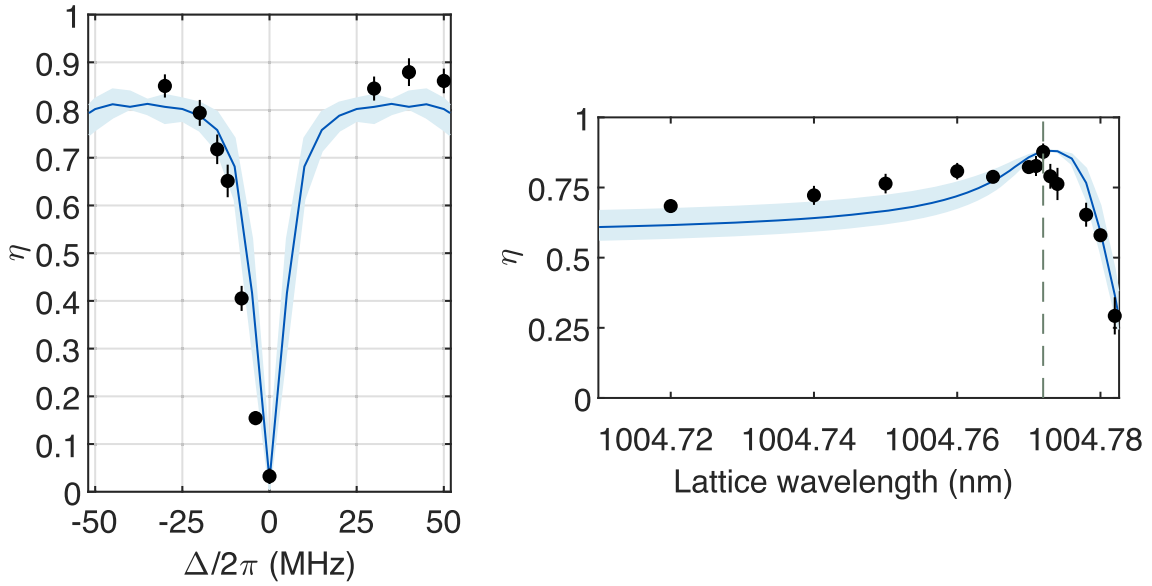


Figure 2.13: Efficiency of STIRAP transfer. As we detune away from resonance by Δ , we see an increase in efficiency, η , because of scattering near resonance arising from experimental imperfections in controlling probe laser polarization (left). As we tune the lattice to the magic wavelength (dashed line), we see an enhancement in the efficiency of the transfer (right). Adapted from [47].

of molecules during the transfer. We can alternatively perform STIRAP in a magic wavelength lattice and we observe enhancement of STIRAP efficiency in a magic trap due to suppression of thermal effects on the states (see figure 2.13) [39].

As a proof of concept, we perform STIRAP from the least-bound state $X_g(-1, 0)$ to the absolute ground state $X_g(0, 0)$, spanning the entire depth of the ground state potential. This technique, however, would allow us to prepare our sample in any vibrational ground state. State transfer using STIRAP is imperative for the level of flexibility and control we would like to have for future clock experiments and precision measurements of fundamental physics [50].

2.5 Long-Lived Molecular States

2.5.1 Coherent Rabi oscillations between ground states

To demonstrate coherent quantum state control of the molecular clock, we induce Rabi oscillations between the two clock states, which we will call states $|1\rangle$ and $|2\rangle$. A Rabi oscillation occurs when the population of a two level quantum system oscillates between the ground state $|1\rangle$ and an excited state $|2\rangle$ due to a driving field [37]. These Rabi oscillations are hallmarks of coherent quantum control and form a basis for metrological applications and precision measurements.

Since we ordinarily measure our molecules from the weakly-bound state, we monitor the time-dependent population in this state, $|1\rangle$, as we observe Rabi oscillations. We can more formally quantify the population in state $|1\rangle$ as

$$P(|1\rangle) = Ae^{-t/\tau_1} [1 + e^{-t/\tau_{\text{Rabi}}} \cos(\omega t - \phi)] \quad (2.16)$$

where τ_{Rabi} describes the lifetime of coherent Rabi oscillations, while τ_1 accounts for the overall loss of molecules due to a variety of scattering processes [39]. Again, we can demonstrate coherent Rabi oscillations in a specific pair of states, as a proof of principle. For example, we drive Rabi oscillations between $X_g(-1, 0)$ and $X_g(4, 0)$. From figure 2.8, one of the largest predicted transition strengths is between $1_u(25, 1)$ and $X_g(4, 0)$, which corresponds experimentally to a magic detuning, $\Delta_m = 2.298(41)$ GHz.

Using this pair of states as a test case, we demonstrate long-lived coherent two-photon Rabi oscillations with $\tau_{\text{Rabi}} = 77(6)$ ms and $\tau_1 = 127(8)$ ms (see figure 2.14). While this represents a significant improvement over previous work [32], there are still inherent limitations that affect the overall lifetime of these molecules. Specifically, these oscillations are predominantly damped by the one-body loss of $X_g(4, 0)$ molecules [39]. In particular, we note that this single-body loss is

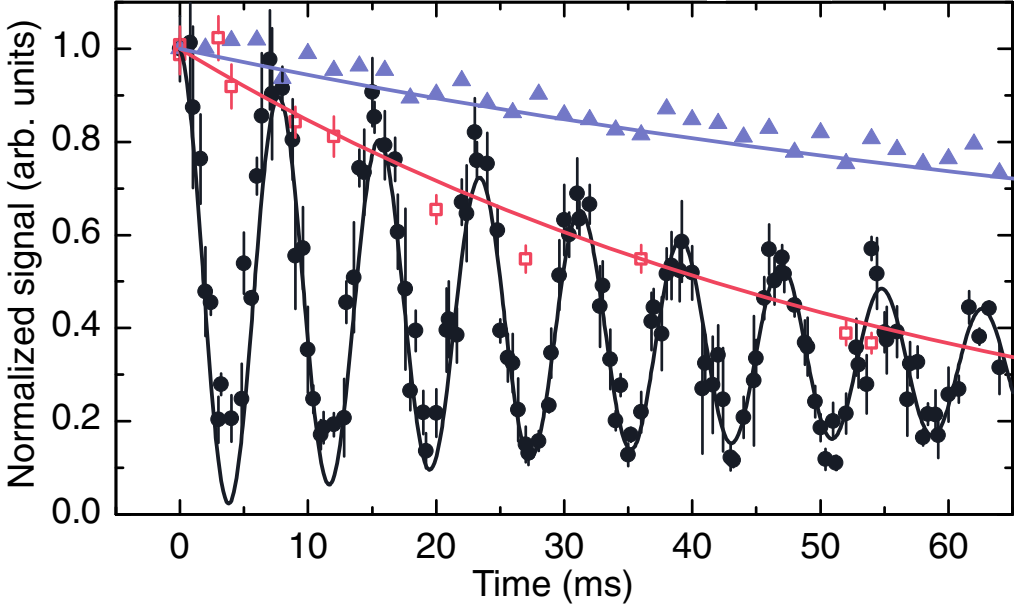


Figure 2.14: Two-photon Rabi oscillations between $X_g(-1, 0)$ and $X_g(4, 0)$ (black circles). Favourable magic trapping is achieved by tuning the lattice near the $X_g(4, 0)$ to $1_u(25, 1)$ transition. Also shown are the normalized population decay of $X_g(4, 0)$ (red squares) and $X_g(-1, 0)$ (blue triangles). Adapted from [39].

faster for deeper traps, which indicates that the large scattering originates from the lattice. These effects can be mitigated in other clock configurations by further detuning from 1_u transitions or by decreasing the lattice light intensity. Much of the later discussion in this thesis, in particular in chapter 4, will focus on ways to mitigate lattice-induced losses while balancing other contributions to the overall clock Q factor.

2.5.2 Lifetime of the absolute ground state

As we saw from our study of $X_g(4, 0)$ molecules, in these deeply-bound ground vibrational states there are both one-body (light-assisted) and two-body mechanisms for fast loss. Specifically, these processes include scattering through excited states and collisional losses. Loss rates are quantified as

$$\frac{dN}{dt} = -k_\gamma N^\gamma \quad (2.17)$$

with $\gamma = 1$ and 2 , respectively, for one- and two-body loss mechanisms, and where k_γ is a free parameter related to the loss rate coefficient. Near-resonance light-induced loss rates are given by equation 2.3, but in practice are much larger and non-linear in lattice intensity. In order to have a large Q factor clock, we want to have long-lived, narrow clock transitions. We are particularly interested in the behaviour of $X_g(0, 0)$ since it is an attractive candidate for a clock state in our system.

To obtain a sample of $^{88}\text{Sr}_2$ in the rovibrational ground state, we first prepare a purified $v = -1$ sample containing only $J = 0$ molecules, removing any $J = 2$ molecules from the initial photoassociated mixture. We transfer our $X_g(-1, 0)$ molecules to $X_g(0, 0)$ using a forward STIRAP sequence, holding them in the rovibrational ground state before reversing STIRAP to photodissociate and detect weakly-bound molecules again. As usual, we monitor $X_g(-1, 0)$ population via recovered atoms in order to gain information about the population of $X_g(0, 0)$. Knowing our STIRAP transfer efficiency, we can infer population in $X_g(0, 0)$ from population in $X_g(-1, 0)$.

In order to study the lifetime of molecules in $X_g(0, 0)$, we vary the hold time in a non-magic (non-scattering) lattice. To ascertain the loss mechanism, we can fit both a one body- and two-body loss function, $N_1(t) = N_0 e^{kt}$ and $N_2(t) = N_0 / (A - kt)$, solving equation 2.17. We find that the lifetime is dominated by two-body collisional loss mechanisms, and that molecules in the rovibrational ground state survive for ~ 200 ms before they are lost (see figure 2.15) [47]. In a sense, this sets an upper limit on the lifetime of molecules in our current experimental configuration since two-body losses are unavoidable in our high-density lattice trap.

Nevertheless, there are methods to mitigate these losses, and in particular the two-body loss mechanisms are strongly density dependent. Proposals to extend the lifetime primarily rely on reducing the current trap density; specifically, implementation of lower-density (larger) or 3D lattices can strongly suppress these types of collisional losses and enable much longer interrogation

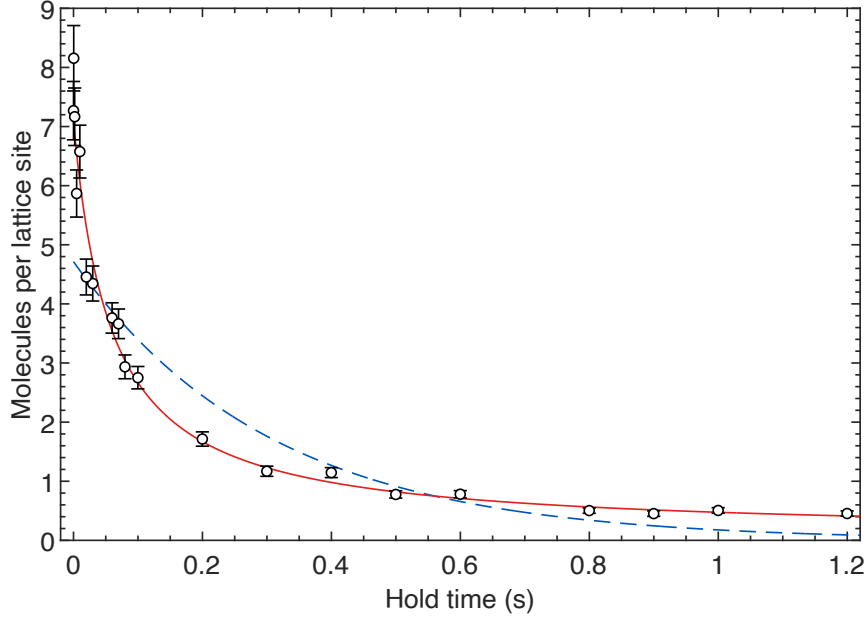


Figure 2.15: The lifetime of our absolute ground state molecules, $X_g(0, 0)$. The red curve represents a fit to a two-body loss differential equation, whereas the blue dashed curve represents a fit to a one-body, exponential decay. The decay behaviour clearly favours two-body loss mechanisms, with a lifetime of about 200 ms. Adapted from [47].

times [34, 51].

2.5.3 Understanding collisional losses

There has been a fair amount of work done with many other molecules to understand the origin of relatively fast loss in the rovibrational ground state. In fact, these kinds of inelastic collisional (loss) rates have been measured in many molecules, including in many bi-alkalis [52, 53]. Therefore, we hope to better understand the origin of the loss of our $^{88}\text{Sr}_2$ ground state molecules, and, specifically, how it does or does not fit into the body of other research done on ultracold chemistry of atoms and molecules.

In its simplest form, two-body collisional loss occurs when two atoms or molecules collide and one is effectively kicked out of the trap or becomes dark to imaging. The likelihood of colliding is related to the effective cross-section of the molecules. The decrease in molecule population, N ,

is accompanied by an increase in the temperature, T , of the sample, since any collisions are more likely to occur at the centre of the trap, where the density is higher; these molecules are usually colder and any process that preferentially kicks out these molecules, raises the overall temperature of the sample [54]. We can, therefore, quantitatively describe the rate of two-body loss as

$$\frac{dN}{dt} = -\beta A \frac{N^2}{T^{3/2}} \quad (2.18)$$

where $A = (m\bar{\omega}/4\pi k_B)^{3/2}$ is a constant that depends primarily on the mean trap frequency $\bar{\omega} = (\omega_{\text{ax}}\omega_{\text{rad}}^2)^{1/3}$, and β is the two-body loss coefficient [55]. For the sake of simplifying our analysis, we assume that the temperature remains the same at a given hold time [47].

We can extract the two-body loss parameter, β , by calibrating the density of our sample and fitting experimental measurements of the $X_g(-1, 0)$ population of our molecules to the two-body loss model (equation 2.18) [47]. Previous experiments have reported loss rates within a factor of unity of that predicted by universal loss models, where two molecules have unit probability of being lost when they are within a short range [52]. As with previous experiments, we are interested in comparing our measurements with predictions from universal loss models.

Universal loss models look to understand the basic aspects of ultracold chemistry. These models assume the special case where two interacting molecules have a unit probability of a chemical reaction or an inelastic collision if they approach one another within typical chemical interaction distances (usually ~ 1 nm or less) [56]. If we specifically consider two molecules interacting in the rovibrational and electronic ground state, then the elastic and inelastic collision rate constants, \mathcal{K}^{el} and \mathcal{K}^{is} , are given by

$$\begin{aligned} \mathcal{K}_{l=0}^{el} &= 4g \frac{\hbar}{\mu} k \bar{a}^2 \\ \mathcal{K}_{l=0}^{is} &= 2g \frac{\hbar}{\mu} \bar{a} \end{aligned} \quad (2.19)$$

with $\bar{a} = \frac{4\pi R_6}{\Gamma(1/4)^2}$, where $R_6 = \frac{1}{2} \left(\frac{2\mu C_6}{\hbar^2} \right)^{1/4}$, μ is the reduced mass, and k is the mean relative wave number. For our specific case, we assume that we have identical bosons ($l = \text{even}$) and that our identical species are in identical states, such that $g = 2$ [56]. Assuming that $p = \hbar k$, and that the velocity is roughly related to the temperature of our molecules, that is $v = \sqrt{\frac{2k_B T}{m}}$, we can write that $k = \frac{1}{\hbar} \sqrt{2k_B T m}$. For our molecule, we use $m = 87.905\,619$ a.u. and we find $C_6 = 15\,685$ a.u. for $^{88}\text{Sr}_2$ [47]. Our estimate for the isotropic van der Waals coefficient, C_6 , relies on a coupled-cluster computation [57, 58] and the best approximation XCCSD4 method [59, 60].

Overall, we predict the universal loss rate to be $1.22 \times 10^{-10} \text{ cm}^3 \text{s}^{-1}$, in agreement with the measured loss rate for $X_g(0, 0)$, which is $0.98(28) \times 10^{-10} \text{ cm}^3 \text{s}^{-1}$, and is unaffected by the absence or presence of $J = 2$ molecules in the sample (see figure 2.16) [47]. This suggests that our molecules react with near unity probability after a short-range collision. There are a number of possible mechanisms for this loss including the formation of stable trimers, or the formation of ‘sticky’ four-body complexes [61, 62].

We also measure two-body loss rates for our weakly-bound molecules in $X_g(62, 0)$. We find that the two-body coefficient, β , is $2.2(0.3) \times 10^{-10} \text{ cm}^3 \text{s}^{-1}$, slightly larger than the predicted universal rate. This further emphasizes that vibrational relaxation effects are non-negligible for the weakly-bound state.

All told, we have successfully demonstrated some key features necessary to build a high-precision metrological system. This includes achieving narrow clock linewidths, facilitated, in part, through state-insensitive trapping, precise quantum state control and specific state transfer via STIRAP, and, finally, long-lived molecules. These ingredients will be key as we move toward our first full clock systematic measurement with record precision.

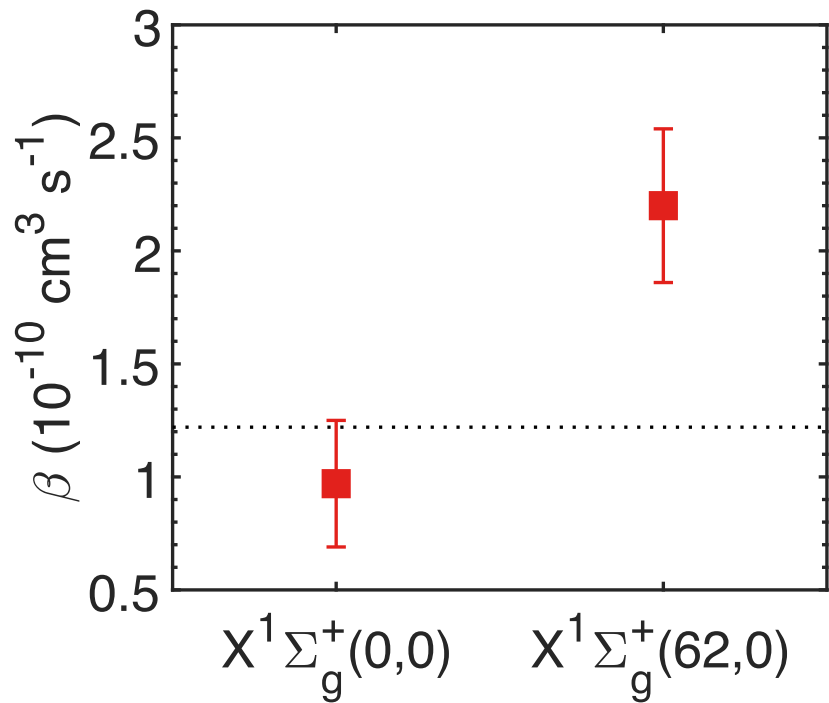


Figure 2.16: Two-body coefficients, β , for $X_g(0, 0)$ and $X_g(62, 0)$. We compare our results to the calculated universal loss rate, $1.22 \times 10^{-10} \text{ cm}^3 \text{s}^{-1}$ (dashed line), and see that our rovibrational ground state molecules collide with near unity probability after a short-range collision. The higher $X_g(62, 0)$ loss rate is suggestive of additional loss mechanisms. Adapted from [47].

Chapter 3: A Systematic Evaluation of Our First Generation Clock

The work presented in this chapter is primarily led by previous graduate student, KH Leung. I present this work here in order to contextualize our current work on this project, by highlighting important aspects of our previous work. A more complete description of this work is elaborated on in KH Leung’s thesis [19] and in the publication of our clock campaign [18].

3.1 A High-Precision Frequency Measurement in $^{88}\text{Sr}_2$

3.1.1 An overview of the clock scheme

Our current, first-generation molecular clock is based on the transition between $X_g(-1, 0)$ and $X_g(0, 0)$ (see figure 3.1). Leveraging our work in chapter 2, we preferentially select favourable magic wavelength lattice configurations, which minimize the impact of lattice-induced light shifts on our molecules, and choose intermediate states that strongly couple to our clock states. These states are preferred for Raman spectroscopy as they possess favourable Rabi frequencies. In particular, we couple our upleg and downleg lasers via $0_u^+(11, 1)$, which boasts large Franck-Condon factors, or large coupling strength, for each clock state. Moreover, we preferentially drive the transition at relatively large Raman detunings to the intermediate $0_u^+(11, 1)$ state in order to minimize any off-resonant scattering from the probes. We operate at a Raman detuning of +14.973 GHz, which is over 3 orders of magnitude greater than the 5 MHz natural linewidth of the intermediate state.

In our molecular clock, we require high levels of frequency control over our probe lasers. As such, the upleg clock laser at 793 nm is stabilized to a high finesse ultra-low expansion (ULE) reference cavity, which serves as a reference for stabilising all other lasers. The phase coherence

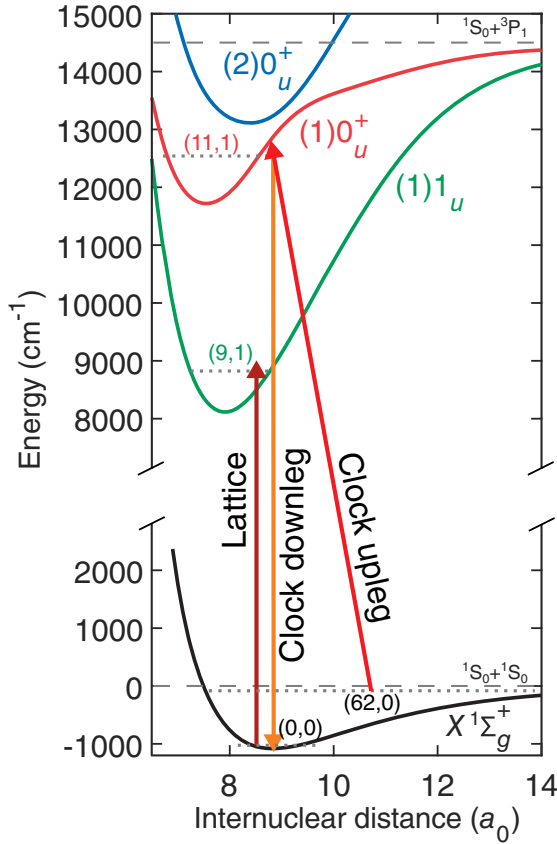


Figure 3.1: Our vibrational molecular lattice clock scheme. Raman lasers (upleg, red arrow; downleg, orange arrow) are detuned from an intermediate state, $0_u^+(11, 1)$ and probe the two-photon vibrational clock transition between $X_g(62, 0)$ and $X_g(0, 0)$. The optical lattice (brown arrow) is parked near resonance, addressing the $1_u(9, 1)$ transition to satisfy the magic condition. Adapted from [18].

of the upleg is transferred to the teeth of our frequency comb by using the ULE as a reference for the repetition rate (RR). The carrier-envelope offset (CEO) frequency of the comb is stabilized to a rubidium standard that also serves as the laboratory local timebase. In turn, the downleg clock laser at 731 nm is phase locked to the comb, inheriting phase stability from the upleg.

For our optical lattice, we select a magic wavelength that leads to one of the largest magic detunings (measured to be $\Delta = 4.494(1)$ GHz) as predicted by our previous work [39] (see figure 2.8). This magic lattice at 1004.7723(1) nm is blue detuned from the $X_g(0, 0)$ to $1_u(9, 1)$ transition, a transition with a relatively high measured transition strength of $1.335(35) \times 10^{-4} (ea_0)^2$, leading

to a large detuning and favourable magic lattice condition.

In order to mitigate any lattice-induced broadening of our linewidth, we ensure that we limit all extraneous scattering effects from the lattice. Specifically, since neighbouring $1_u(v, 1)$ rovibronic resonances are spaced at intervals of ~ 2 THz, we minimize any additional scattering through these states due to lattice light impurity such as amplified spontaneous emission (ASE), by using spectrally clean light derived from a Ti:sapphire laser. To suppress any additional ASE impurity at the magic detuning, the lattice light is filtered through a linear cavity with a finesse of 50, and free spectral range of 2.9 GHz, before reaching our experiment. Just like our probe lasers, the lattice light that is delivered to the molecules is phase-stabilized to the optical frequency comb by actuating on a voltage-controlled oscillator (VCO) that modulates the frequency of the lattice.

The experiment relies on dual-purpose acousto-optical modulators (AOMs) for both shuttering the light from our different laser sources and for modulation of our laser frequencies. Both the upleg and downleg lasers, as well as lattice, pass through AOMs, which help us set and stabilise desired frequencies while maintaining flexible control over the frequency during our measurement sequence. This is crucial in allowing us to repeatedly and consistently scan over the clock resonance, and fast AOM shuttering also allows us to control the total interrogation time of our clock.

3.1.2 Methods for technical stabilization of our system

It is imperative that we have high levels of technical control over our probe and lattice lasers, as these are the primary sources of light that interrogate our molecules. Specifically, we need to ensure control over their frequency, intensity and polarization.

The clock lasers are directed to our experiment via the same polarization-maintaining (PM), single-mode (SM) optical fibre. A laser will experience linewidth broadening due to fibre phase noise of up to ~ 100 Hz [18]. In order to combat this phase noise, we perform active fibre noise

cancellation (FNC); since the clock laser wavelengths are sufficiently different and laser beams likely follow non-identical paths in the fibre, we implement FNC on each laser, independently [63, 64].

A full scheme for FNC is shown in figure 3.2. Specifically, the laser beam is initially divided by a 50:50 non polarizing beam splitter; one beam path is retro-reflected on a reference surface toward a low-noise photodiode, while the other passes through an AOM driven by a VCO. The diffracted AOM order of interest is fed to the experiment via an optical fibre, which writes phase noise ϕ_{noise} on to the laser. We can detect this phase noise, by retro-reflecting part of the light back through the fibre and recombining it with the initial reference light on the beam splitter. Specifically, we expect to detect $2\phi_{\text{noise}}$ at a beat frequency shifted by $2\omega_{\text{AOM}}$ [18]. We mix down this beat frequency to create a reference error signal; a servo controller uses this error signal to actuate on the VCO and compensate for this phase noise preemptively by adding an additional phase, $-\phi_{\text{noise}}$, to the AOM. The laser light after the reference surface is, therefore, fibre noise canceled. When addressing the clock states it is imperative that we also have clean polarization. We use a Glan-Thompson prism to clean up the polarization of each probe beam after the phase reference surface.

In addition to stabilising the frequency of our lasers, we must adequately stabilise the intensity of light at our molecules. We do so by separating our clock beams on a (long-pass) dichroic, after which a small fraction of the light is picked off and its intensity is measured on a photodiode. Independent intensity stabilisation of each clock laser is performed by actuating on the RF power to the relevant AOMs. As for our lattice, a stable, weak reflection from the vacuum window is used for lattice intensity stabilization. After the pickoffs for intensity stabilisation, the clock lasers are recombined on another dichroic and further combined with the lattice before passing through the chamber to our molecules.

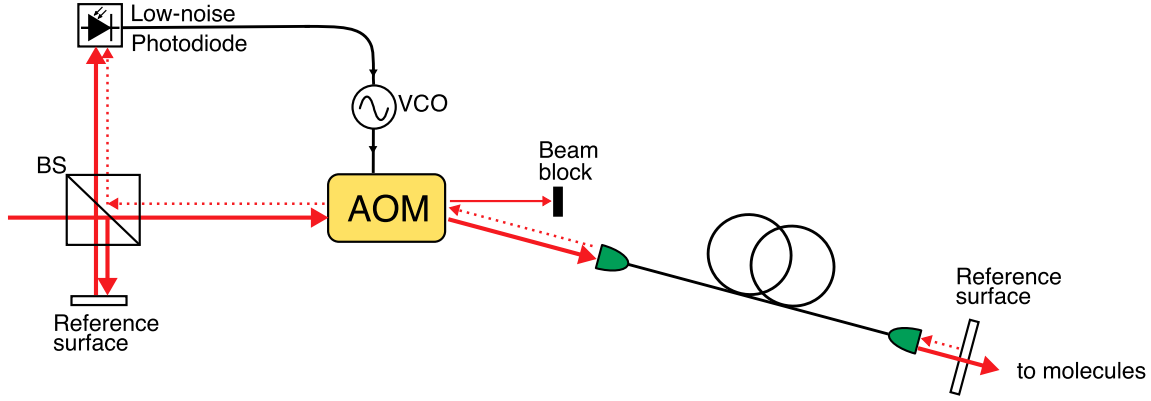


Figure 3.2: A scheme for fibre noise cancellation (FNC) of our probe beams. A laser beam is initially divided on a 50:50 non polarizing beam splitter (BS) cube, and one beam is retro-reflected as a reference, while the other is diffracted by an acousto-optic modulator (AOM) driven by a voltage-controlled crystal oscillator (VCO). Then, the diffracted order is injected into an optical fibre to the experiment. To combat phase noise written by the fibre, we perform active FNC, by retro-reflecting a small portion of the light back through the fibre and recombining it with the original reference light. Beat detection on a low-noise photodiode produces a reference error signal for active feedback on the VCO to preemptively cancel the fibre phase noise. Adapted from [19].

3.1.3 Comparison to local time standard

In order to directly compare any relative or measured frequency in our experiment to other frequency measurements, we reference all frequency counters and direct digital frequency synthesizers (DDSs) in our experiment to a free-running rubidium (Rb) microwave standard. The Rb clock standard is in turn calibrated by comparing an internal 1 pulse-per-second (PPS) output to that of a dual-band global navigation satellite system receiver on a time-interval counter (TIC) [18]. The Rb clock serves as a flywheel oscillator to access Global Positioning System (GPS) time [65]. In turn, GPS time is steered Coordinated Universal Time (UTC) in the United States (see figure 3.3) [66].

Any timing differences between UTC, International Atomic Time (TAI) and the standard (SI) second are routinely published, providing a global comparable standard for our clock measure-

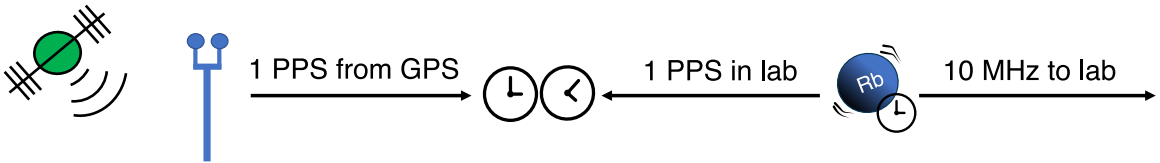


Figure 3.3: Comparison of our local time standard to global reference time standard. Our local time standard, a Rubidium microwave clock, acts as a flywheel oscillator, linking the molecular clock to GPS time for the absolute frequency measurement. Specifically, we compare our internal 1 pulse-per-second (PPS) from our lab to a reference 1 PPS from GPS via dual-band global navigation satellite system receiver on a time-interval counter. Our GPS time is steered by Coordinated Universal Time (UTC) and International Atomic Time (TAI) giving us a way to locally reference our clock measurements to absolute frequency standards.

ments [67]. We compare our local frequency measurement to the standard SI second as

$$\frac{f_{clock}}{f_{SI}} = \frac{f_{clock}}{f_{Rb}} \times \frac{f_{Rb}}{f_{GPS}} \times \frac{f_{GPS}}{f_{UTC}} \times \frac{f_{UTC}}{f_{TAI}} \times \frac{f_{TAI}}{f_{SI}} \quad (3.1)$$

It is important to note that the fractional uncertainty of the Rb standard is limited to 3×10^{-13} after $\sim 5 \times 10^3$ s of averaging time; this stability worsens for longer periods over 24 hours.

While our fractional uncertainty from systematic effects of our clock — after averaging — is 4.6×10^{-14} for relative frequency measurements [18], any absolute frequency measurement referenced to the Rb time base will inevitably be limited to fractional stabilities on the order of 10^{-13} . This proves a technical limitation on the absolute frequency measurement of our clock as a standard for the second. Any effort to push absolute frequency measurements beyond this level would require a different local time standard, such as a Cs fountain clock or hydrogen maser [68], as a comparison to our clock. Nevertheless, many precision measurements require only relative, internal comparisons, and, therefore, can still benefit from the higher levels of stability inherent in our clock.

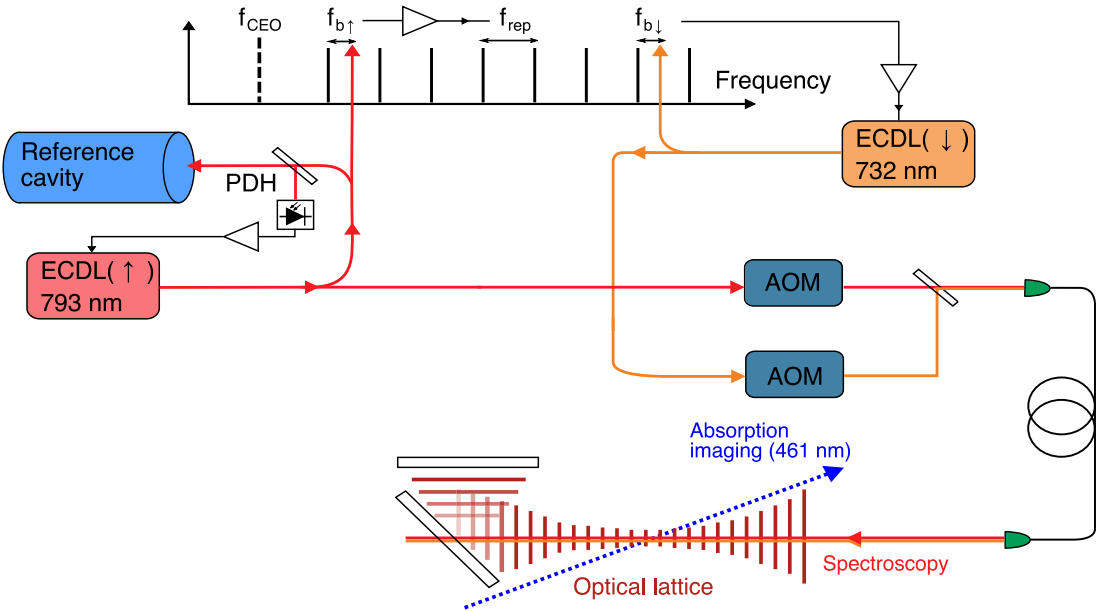


Figure 3.4: Frequency stabilisation of our probe lasers. We utilize a ULE cavity as a reference for our 793 nm upleg probe laser. The repetition rate (f_{RR}) of our frequency comb is phase locked to the upleg probe laser at a beat frequency $f_{b\uparrow}$, inheriting the cavity stability. The downleg 732 nm probe laser is phase locked to the frequency comb at a beat frequency $f_{b\downarrow}$ relative to a higher comb tooth number. The offset of the frequency comb (f_{CEO}) is referenced to the local 10 MHz reference from our rubidium microwave clock standard. Adapted from [19].

3.1.4 An absolute frequency measurement

Given our current clock scheme, the frequency of our transition is determined by precisely measuring the frequencies of the two probe lasers. Very simply, we measure the clock frequency as a difference between the frequency of the upleg Raman probe and the frequency of the downleg Raman probe. That is,

$$f_{meas} = f_{\uparrow} - f_{\downarrow} \quad (3.2)$$

Each of f_{\uparrow} and f_{\downarrow} are determined in reference to the frequency comb and any frequency modulation by AOMs. Specifically, as an example, we determine the frequency of the upleg to be

$$f_{\uparrow} = N_{\uparrow} f_{RR} + 2f_{CEO} + f_{b\uparrow} + f_{AOM} \quad (3.3)$$

where N_\uparrow is the comb tooth number of the frequency comb, f_{RR} is the repetition rate of the frequency comb, f_{CEO} is the offset of the frequency comb and $f_{b\uparrow}$ is the locking beat frequency difference between the laser and the nearest comb tooth. Any additional AOMs add a term f_{AOM} to the overall frequency of the probe light (figure 3.4).

In addition to the measured frequency of the individual probe lasers, we must account for the effect of any systematic shifts in the system (detailed in section 3.2). These shifts introduce a necessary frequency correction, f_{corr} , to the measured frequency, f_{meas} , in order to determine the true frequency, f_{clock} . The true clock frequency is given by adding these corrections to the measured clock frequency, as in

$$f_{\text{clock}} = f_{\text{meas}} + f_{\text{corr}} \quad (3.4)$$

In table 3.1, we show a budget for the largest contributions to the systematic correction of the measured frequency. Summing the uncertainties of all contributions to systematic corrections in quadrature, we report a total systematic uncertainty of 4.6×10^{-14} after ~ 3 hours of averaging per systematic effect [18]. Accounting appropriately for these systematic shifts is crucial for achieving high overall accuracy for our clock and for any future precision measurements. Since by far

Table 3.1: A systematic uncertainty budget for the strontium molecular clock. Frequency corrections (f_{corr}), with corresponding uncertainties ($\sigma_{f_{\text{corr}}}$), are listed for the primary contributions to the clock uncertainty. The true clock frequency f_{clock} is given by adding these corrections to the measured clock frequency (f_{meas}) (as shown in equation 3.4). All values are expressed in fractional units ($\times 10^{-14}$).

Systematic (δf)	Correction (f_{corr})	Uncertainty ($\sigma_{f_{\text{corr}}}$)
Lattice Linear Stark Shift	100.1	3.4
Lattice Quadratic Stark Shift	-50.8	1.9
Probe Stark Shift	31.5	2.2
Black-body Radiation Shift	-2.2	0.4
Density Shift	-0.6	0.3
Total Shift	77.9	4.6

the largest contribution to the uncertainty in our measurement is due to the lattice, we focus on improvements we can make in the lattice for our next generation clock.

In sum, we measure the absolute frequency of the transition between $X_g(62, 0)$ and $X_g(0, 0)$ in $^{88}\text{Sr}_2$ as [18]

$$f_{\text{clock}} = 31\,825\,183\,207\,592.8(5.1) \text{ Hz} \quad (3.5)$$

This result is the weighted average of 10 trials with an averaging time of $\sim 10^3$ s per trial (figure 3.5). Given a record clock linewidth of 10.5(1.2) Hz, we obtain a corresponding Q factor

$$Q_{\text{clock}} = (3.0 \pm 0.4) \times 10^{12} \quad (3.6)$$

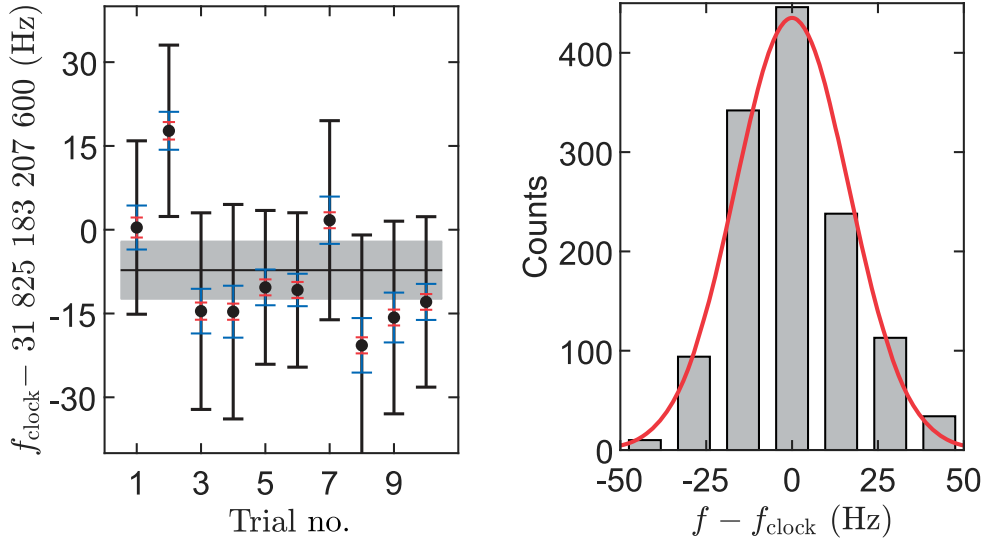


Figure 3.5: Absolute frequency of our clock transition measured over ten trials (left) with all known systematic frequency corrections and comparison to local Rb time base. Blue error bars are 1σ statistical uncertainties, dominated by determination of the comb repetition rate (RR). Red error bars are 1σ systematic uncertainties due to the inherent molecular clock uncertainty (see table 3.1). Black error bars are 1σ total uncertainties, where the uncertainties of the local time-base calibrations are added in quadrature with the statistical and molecular clock systematic uncertainties. The black horizontal line shows the weighted average, and the shaded gray area shows the associated 1σ standard error of the mean. Histogram (right) of all clock frequency measurements in the ten trials, relative to the weighted average of f_{clock} . The solid red line is a Gaussian fit to the histogram. Adapted from [18].

3.2 Systematic Corrections of our Clock Frequency

3.2.1 Systematic shifts from light sources

Any source of light will produce a Stark shift proportional to the intensity of the light. In our clock, the two primary sources of light, which are relevant to the measured frequency of the clock transition, are the probe (clock) lasers and the lattice. We measure and extrapolate the systematic shift imparted on the measured frequency in normal clock operation by each source of light.

Probe light shifts are an inherent aspect of any two-photon spectroscopy. The light shifts from our clock lasers scale linearly at low intensities and are directly related to the differential polarizability at the respective probe wavelength, that is

$$\delta f_{probe} = \frac{I}{2h\epsilon_0 c} (\alpha_0(\omega) - \alpha_{62}(\omega)) \quad (3.7)$$

where $\alpha_v(\omega)$ is the E1 polarizability for vibrational state v in the X_g potential, ω is the probe frequency and I is the probe laser intensity [69]. We can minimize the total probe light shift systematic by using so-called balanced intensity ratios satisfying the condition $I_\uparrow[\alpha_0(\omega\uparrow) - \alpha_{62}(\omega\uparrow)] = -I_\downarrow[\alpha_0(\omega\downarrow) - \alpha_{62}(\omega\downarrow)]$ [70]. We demonstrate this condition in our clock for blue detunings of the probes relative to the transition, where the baseline polarizability differences at the probe wavelengths have opposite signs as shown in figure 3.6.

We evaluate the probe shift, δf_{probe} , for each leg of the Raman transition independently. Using a motorized neutral density (ND) filter, we alternate between high and low intensity values for one leg, while keeping the intensity of the other leg fixed at its operational value. These measured shifts are then scaled by the intensity difference to obtain the clock corrections at the operational intensity, I_{op} ; that is, for each probe laser, we calculate

$$\delta f_{probe} = \frac{\delta f}{\delta I} I_{op} \quad (3.8)$$

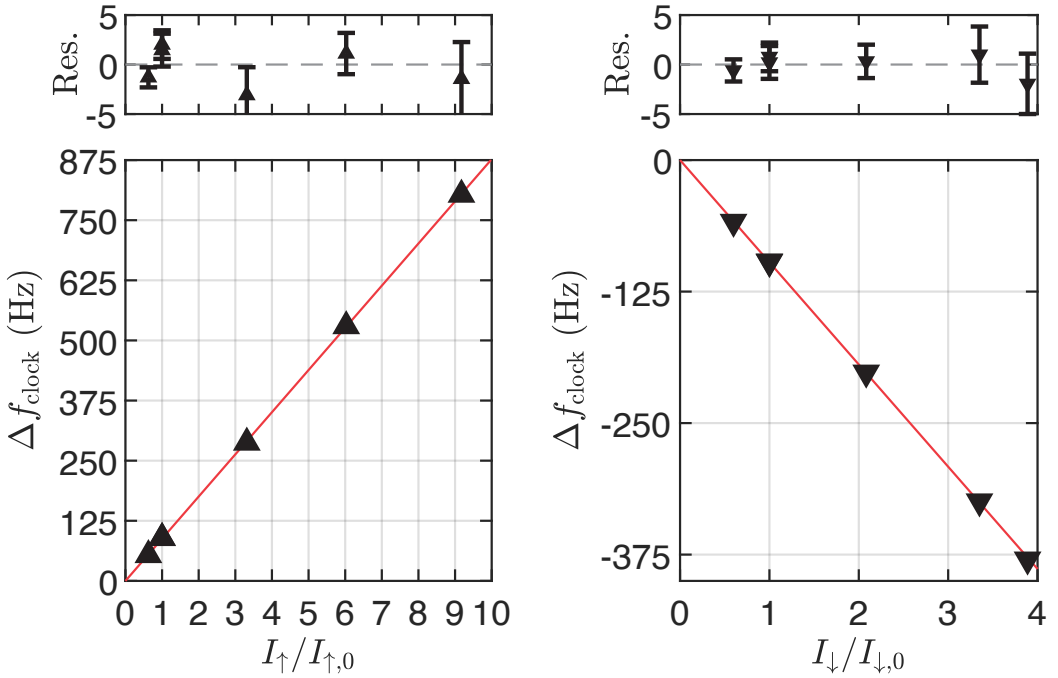


Figure 3.6: Light shifts from our Raman probe lasers as a function of the upleg laser intensity (left), and the downleg laser intensity (right). The horizontal axes are normalized to operational intensities, $I_{\uparrow,opt}$ and $I_{\downarrow,opt}$. Solid lines are linear fits to the data. Residuals are plotted in units of Hz. Adapted from [18].

Using this scheme, we find fractional corrections for the upleg to be $-277.5(1.4) \times 10^{-14}$ and for the downleg to be $309.0(1.7) \times 10^{-14}$ (see figure 3.6). This leads to an overall fractional correction of $31.5(2.2) \times 10^{-14}$ as reported in our uncertainty budget at operational intensities [18].

We investigate the lattice light shift for a range of lattice frequencies at several trap depths from 300 to 1100 E_r . We again use a motorized ND filter to alternate between high and low intensities during a clock run. Most importantly, we find non-linear light shifts due to molecular hyperpolarizabilities, a feature which may help explain quadratic lattice scattering rates and fast loss near resonance. We use a thermal model [71], which assumes a linear scaling of atomic temperature with trap depth, to characterise these lattice light shifts as

$$\delta f_{lattice} = -\alpha U_0 - \beta U_0^2 \quad (3.9)$$

where α and β are obtained empirically from parabolic fits to the measured differential shifts, such that α is related to lower-order electric-dipole (E1), magnetic-dipole (M1) and electric-quadrupole (E2) polarizabilities, while β is related to high-order hyperpolarizability effects (see figure 3.7).

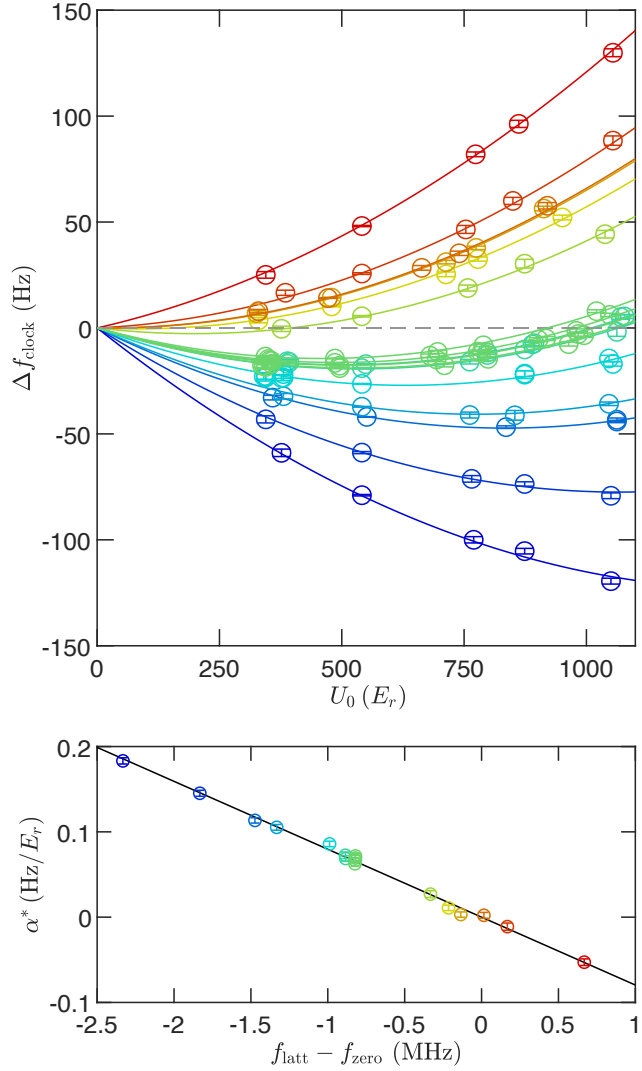


Figure 3.7: Clock shifts due to the lattice light. We show nonlinear shifts of the molecular clock frequency versus trap depth (above). For a given lattice frequency (color coded), we make interleaved measurements of clock shifts (open circles) with respect to a reference trap depth ($\sim 500 E_r$), and fit the data to parabolas (solid lines) with a global quadratic parameter, $-\beta$. We plot the linear light shift coefficient, α , versus lattice frequency (color code matches above), as extracted from the linear fit (black solid line) (below). Adapted from [18].

The evaluation of hyperpolarizabilities using this quadratic fit approximation hinges on a linear scaling of the sample temperature with U_0 , which we can verify using carrier thermometry (as in section 2.2.1) [71, 72]. Using the operating trap depth for our molecular clock, $U_{opt} = 487(4) E_r$, we find that the systematic correction for $\alpha U_{opt} = 31.8(1.1)$ Hz, a fractional correction of $100.1(3.4) \times 10^{-14}$, and find that the hyperpolarizability, non-linear component, contributes a correction $\beta U_{opt}^2 = -16.2(6)$ Hz, a fractional correction of $-50.8(1.9) \times 10^{-14}$ [18].

3.2.2 Temperature effects

As previously described, our molecules experience a Stark shift in the presence of any electric field, which depends on the particular state polarizability and the field intensity. More generally, the frequency shift between the states $|1\rangle$ and $|2\rangle$ of an atom or molecule is given by

$$\Delta\nu_{12} = \frac{-1}{2h} \int_0^\infty \Delta\alpha_{12}(\omega) E^2(\omega) d\omega \quad (3.10)$$

where $\Delta\alpha_{12}(\omega)$ is the frequency-dependent differential polarizability between the two states.

In particular, since our chamber is opaque to long-wavelength light ($\lambda > 2$ microns), we can effectively treat it as a blackbody radiator near room temperature, where the peak blackbody radiation (BBR) wavelength is ~ 10 microns. This inherent BBR electric field causes a temperature-dependent shift in the transition frequency of our molecules [16]. Therefore, we need to experimentally measure the effective temperature of the hardware surrounding the molecular cloud to appropriately characterise and correct for a BBR-induced Stark shift.

Given that the chamber temperature is normally $T \sim 300$ K, we can assume that our peak BBR frequency $\omega_{peak} \ll \omega_{ij}$ allowing us to simplify equation 3.10 as [73]

$$\Delta\nu_{eg} = -\frac{\Delta\alpha_{eg}(0)}{2h} \langle E^2(t) \rangle [1 + \eta(T)] \quad (3.11)$$

We know that a blackbody at a given temperature has the following spectral radiance, $B(\lambda, T)$, for a given wavelength, λ , and a given temperature, T [74]

$$B(\lambda, T) = \frac{2hc}{\lambda^5} \frac{1}{e^{\frac{hc}{\lambda k_B T}} - 1} \quad (3.12)$$

If we assume that this intensity is normal to the surface, we obtain the energy density of the blackbody as

$$u(T) = \int_0^\infty B(\lambda, T) d\lambda \int \cos \theta d\Omega = \sigma T^4 \quad (3.13)$$

Since we know that electromagnetic energy density is related to the RMS electric field by $u = \epsilon_0 E_{RMS}^2$, we can, therefore, write

$$\langle E^2(t) \rangle = \frac{4\sigma T^4}{c\epsilon_0} \quad (3.14)$$

In this way, we can completely describe the BBR electric field by measuring the effective temperature at the molecular cloud.

In order to simplify our evaluation of the BBR shift, we consider primarily the E1 component to the BBR shift, which contributes most significantly [73]. Specifically, we define the E1 BBR shift on a given state v as

$$f_{BBR}^{E1}(v) = -\frac{2}{15} \alpha_{fs}^3 \pi^3 T^4 \alpha_v^{E1}(0) (1 + \eta) \quad (3.15)$$

where α_{fs} is the fine structure constant and η is defined as the first order correction [73]

$$\eta = \frac{80\pi^2}{63\alpha_v^{E1}(0)} T^2 \sum_f \frac{|d_{ij}|^2}{\omega_{fi}^3} \left(1 + \frac{21\pi^2 T^2}{5\omega_{fi}^2} + \frac{336\pi^4 T^4}{11\omega_{fi}^4} \right) \quad (3.16)$$

where $\alpha_v^{E1}(0)$ is the static dipole polarizability. Here, every quantity is defined in atomic units, such that $1 \text{ K} = 3.16683 \times 10^{-6} \text{ a.u.}$ and $1 \text{ a.u.} = 1.51983 \times 10^{-16} \text{ Hz}$ (see Appendix E in [75] for

a more complete list). In this way, the BBR shift on our clock transition is

$$\delta f_{BBR} = f_{BBR}^{E1}(62) - f_{BBR}^{E1}(0) \quad (3.17)$$

Notably, the BBR shift depends on the temperature of the chamber. While the thermal environment surrounding the molecules is complex, we use a simplified model to determine the temperature at the centre of the chamber; we locate the areas with maximum (T_{max}) and minimum (T_{min}) temperature, and assume a rectangular (uniform) probability distribution between these temperatures [76]. We define the average, or rather representative, temperature, T_r , as

$$T_r = \frac{T_{min} + T_{max}}{2} \quad (3.18)$$

with an uncertainty given by¹

$$\sigma_{T_r} = \frac{T_{max} - T_{min}}{\sqrt{12}} \quad (3.19)$$

In order to measure the BBR shift with adequate precision, we use high-precision tools to continuously record the temperature of our chamber throughout a clock run. We measure the temperature to a precision of $\pm 0.05^\circ\text{C}$ using negative temperature coefficient (NTC) thermistors [10 k Ω MC65F103A Amphemol] and a Keithley DAQ6510/7700 model for fast switching, continuous temperature measurements of up to 20 individual channels. We implement remote control of our Keithley via a home-designed, python-based GUI which continuously records the temperature along the four primary faces of our chamber during a experiment run (see figure 3.8).

¹<https://www.bipm.org/en/committees/jc/jcgm>

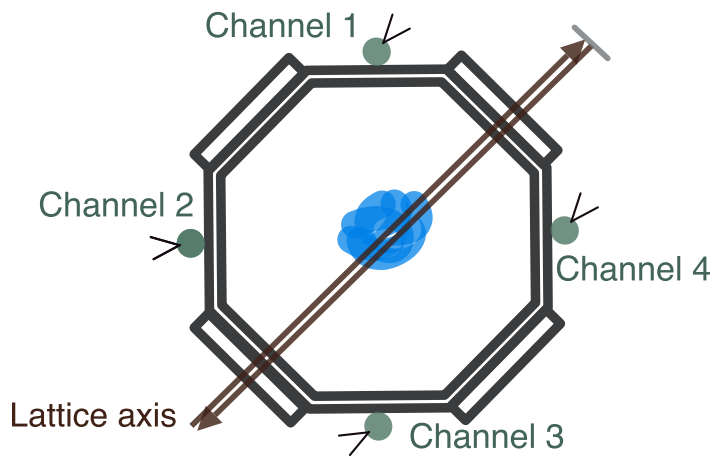
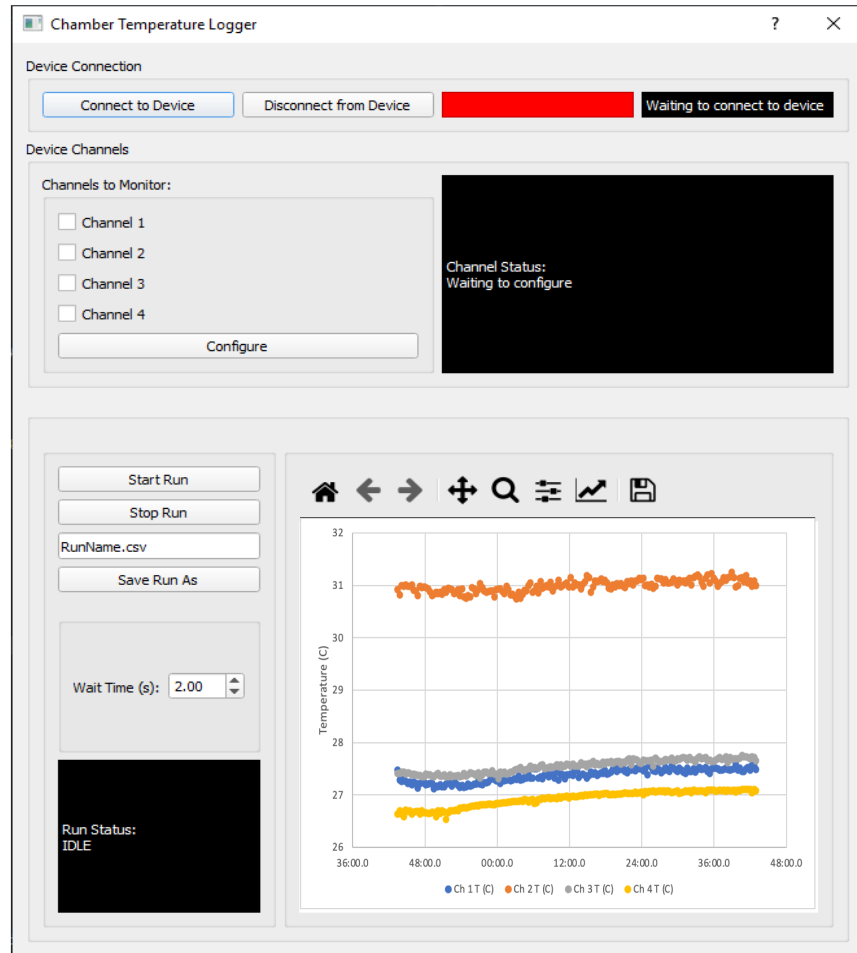


Figure 3.8: Chamber temperature logging scheme for BBR shift measurement. We measure the temperature of the stainless steel chamber on four faces using high-precision $10\text{ k}\Omega$ MC65F103A Amphenol negative temperature coefficient (NTC) thermistors (below). We continuously record the temperature using a Keithley DAQ6510/7700 system and a home-built, python-based GUI for remote control (above).

Using this min-max method, we estimate an effective temperature at the molecules of $T = 303(5)$ K, which corresponds to a correction from the BBR shift on our specified clock states of $\delta f_{BBR} = -0.70(14)$ Hz, a fractional shift of $-2.2(0.4) \times 10^{-14}$ (see figure 3.9). The uncertainty is dominated by *ab initio* calculations of the dc polarizabilities of the clock states [25]. Predictions of these polarizabilities show a non-monotonic behaviour, which suggests an attractive opportunity to design a near-zero BBR shifted clock (see figure 3.10) [25]. These predictions would, in theory, allow us to engineer a BBR-insensitive clock and have consequences for how we engineer our magic wavelength traps; they are largely the impetus for our most recent work and the subject of the following chapter.

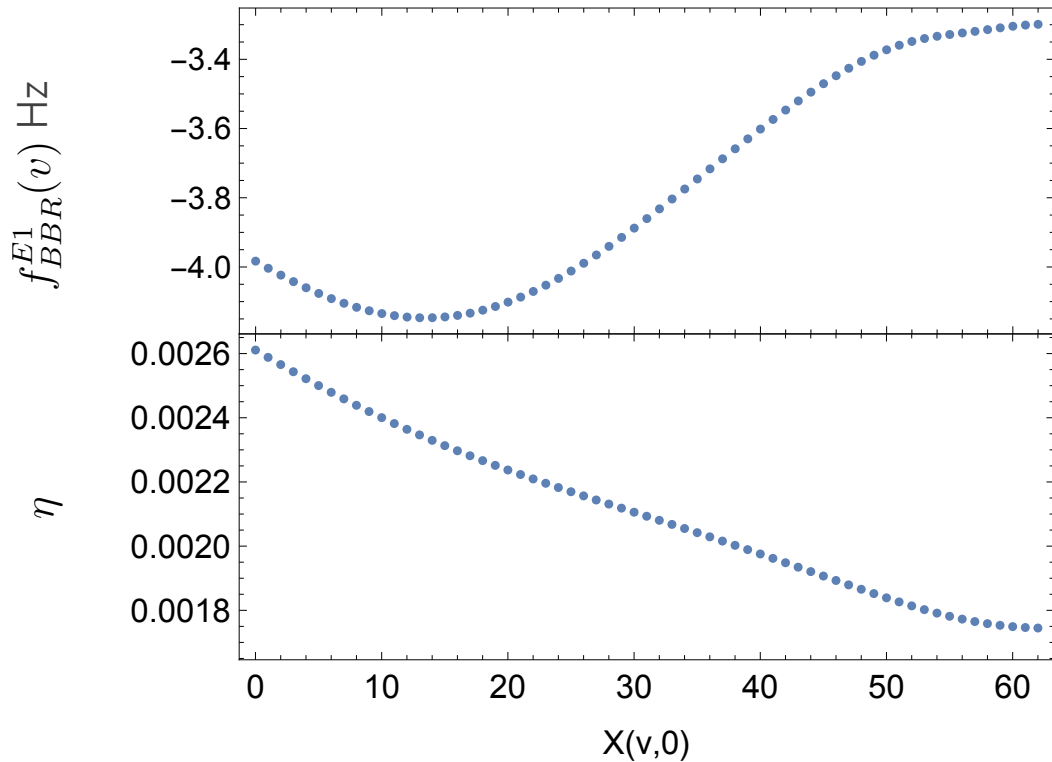


Figure 3.9: Modeled blackbody radiation shift on $X_g(v, 0)$ states at an effective environment temperature $T_r = 300$ K. For our current clock states, $X_g(0, 0)$ and $X_g(62, 0)$, the net BBR shift on the observed clock frequency is $\delta f_{BBR} = 0.70(14)$ Hz. The dynamic term η (equations 3.15 and 3.16) at T_r , included in δf_{BBR} , contributes less than 0.5% to the measured shift.

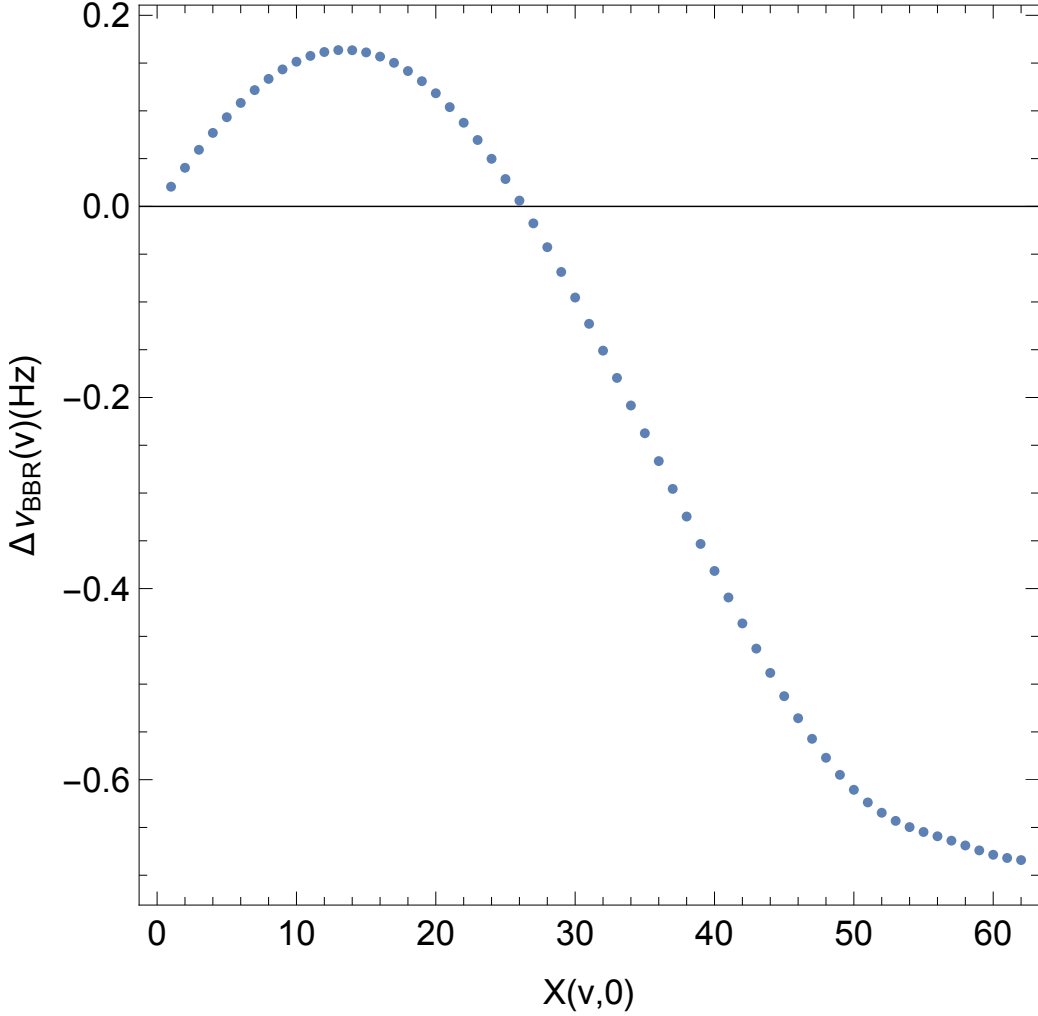


Figure 3.10: Differential BBR shift between $X_g(0,0)$ and other $X_g(v,0)$ states in the ground potential, as predicted by early theoretical models. These models show state pairs that may exhibit near zero BBR shift corrections at $T = 300$ K.

3.2.3 The impact of sample density

As in atomic clocks, we are also interested in investigating and characterising any density-dependent shifts arising from dimer-dimer collisions in our lattice [77]. As we saw in section 2.5.3, our $^{88}\text{Sr}_2$ molecules are highly susceptible to collisions. We probe the density shift by modulating the average number of molecules per lattice site (N_{mol} /site) at the beginning of the clock pulse.

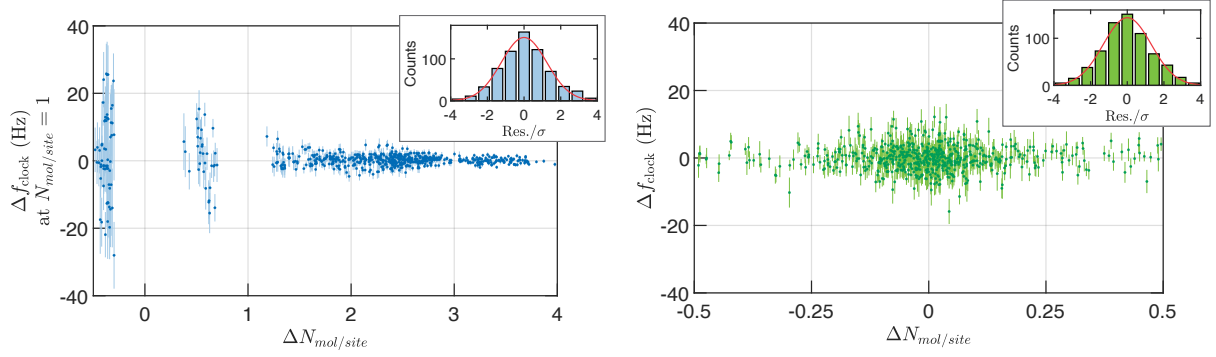


Figure 3.11: Evaluation of density-shift systematic. Clock shifts due to molecular collisions are compared to operating conditions (left). We find a small, non-zero correction of $\delta f_{density} = -0.20(10)$ Hz due to these density-dependent collisional shifts. In the same dataset, the shift between successive resonances taken under identical experimental settings serves as a control experiment to check for technical offsets. As expected, this averages to zero, $0.03(20)$ Hz (right). Both insets show the histogram of normalized residuals, and the solid red lines are Gaussian fits. Adapted from [18].

We find a correction of $\delta f_{density} = -0.20(10)$ Hz, or a fractional correction of $-0.63(31) \times 10^{-14}$, due to these density-dependent, collisional shifts (see figure 3.11). The magnitude of this shift is similar to analogous strontium optical atomic clocks [78]. In the future, we can suppress or eliminate collisional shifts by preparing our molecules in 3D or tweezer traps with low- or single-occupancy. Nevertheless, in this campaign, we already demonstrate clock measurements near $1 N_{mol}/site$ densities, suggesting this pathway towards collisional shielding. It is important to recall that lower-density traps, and fewer test molecules, result in a lower overall signal, a trade-off we must consider when designing a future clock.

3.3 Limitations of Our Current Clock

The nature of our molecular clock states promise long natural lifetimes and a corresponding high precision. Even still there exist technical challenges in the current iteration of the molecular clock that prevent us from achieving Q factors that are much better than our current $Q_{clock} = (3.0 \pm 0.4) \times 10^{12}$.

In particular, our clock Q factor is primarily limited by fast two-body losses and large light-induced scattering that scales quadratically with trap depth. At our current operational densities and trap intensities, these effects have significant ramifications on the spectroscopic signal for clock pulses as fast as ~ 60 ms. If we consider a conservative 30 ms pulse, we can expect to achieve Fourier-limited peaks of ~ 30 Hz linewidth. If we overcome these technical limitations, collisions in the ground state still limit our linewidths to 5 Hz, corresponding to a 200 ms molecular lifetime.

Strategies to address these effects rely on both structural, technical and scientific changes to our current system. On the technical side, we can implement different trapping schemes, namely moving towards a vertical lattice configuration, which naturally decreases the necessary trapping intensity, and, therefore, trap depth. We can further reduce collisional effects in the lattice by reducing the density of our sample; to do so, we can implement a larger trap beam or additional confinement such as in a 2D or 3D lattice, or tweezer-like trap.

By contrast, we can also leverage improved models and better understanding of the underlying quantum chemistry of our strontium dimers to design a fundamentally better clock. In particular, we can search for states which are naturally magic or near-magic, such that inherent BBR effects are nearly cancelled and the lattice-induced systematic effects are greatly reduced. Possible states like these are predicted in some early versions of our theoretical models [25].

In the following chapter, we consider practical ways to address both collisional losses and lattice-induced light shifts in our molecular clock. We suggest and quantify the advantages of each, in particular, highlighting potential trade-offs for a given experimental design, as we set the stage for a second-generation clock.

Chapter 4: Pathways Towards an Improved Clock

In our previous work, we demonstrated a record-breaking precision for our $^{88}\text{Sr}_2$ molecular clock, ushering in a new era for precision measurement with clocks. As described in the previous chapter, borrowing techniques from earlier atomic clock architectures, we measure a ~ 32 THz clock transition between two vibrational levels in the electronic ground state, achieving a Q factor of 3×10^{12} and a fractional uncertainty, after averaging, of 4.6×10^{-14} , in this new frequency regime.

This precision is comparable to the earliest realizations of optical atomic lattice clocks [79–81], which have since seen extensive technical improvement. Given that the Sr_2 vibrational transitions have very long natural lifetimes, we could expect to achieve higher Q factors in the long-term once we overcome many of these same technical challenges. Losses due to two-body collisions and lattice light scattering remain central impediments to better spectroscopic resolution in our molecular clock. Even in ultra-precise atomic clocks, BBR is a major contributor to the systematic error budget of conventional atomic clocks and is notoriously difficult to characterise and control. In this chapter, I discuss avenues towards overcoming these.

4.1 Combating Lattice-Induced Scattering

4.1.1 A new lattice configuration

Currently, the largest contribution to the systematic uncertainty of our molecular clock is the Stark shift from our optical lattice [18]. These large systematic effects arise in part due to the high trapping intensity of our current horizontal lattice, which is necessary to confine our molecules in the trap against gravity. Unfortunately, this high-intensity trap imparts a large systematic uncertainty on our current clock configuration.

One simple way to combat this issue is to move towards a vertical lattice geometry. Since confinement is tighter along the axial, rather than radial, direction of the lattice, we would benefit from orienting our lattice such that gravity points in the axial direction, reducing the overall intensity necessary in the trap [82]. A vertically oriented 1D lattice tightly confines along the axis of gravity and has the added advantage of suppressing tunneling due to the difference in gravitational potential energy between lattice sites [83].

Given the existing orientation of our MOT beams, we must find a way to combine our vertical MOT beams with other critical lasers along the same axis. These include the photoassociation (PA) and photodissociation (PD) beams, probe (clock) beams and the lattice. In this design, we opt to use dichroic beamsplitters to combine the light, as opposed to polarizing or non-polarizing beam splitters, so as to minimize any loss of power and maintain flexible control over the polarization of each distinct source of light. In order to combine each beam along the vertical axis, we need two pairs of dichroics, one which combines the probe beams (732 nm and 793 nm) with the lattice at 1005 nm¹, and another which combines the MOT light (461 nm and 689 nm) with the probe and lattice beams². We preferentially choose dichroics that transmit, rather than reflect, the probe beams in order to maintain cleaner polarization of these critical lasers (see figure 4.1). The PA and PD beams are combined with the MOT beams using polarizing beamsplitters and, therefore, care must be taken to ensure that we have sufficient power in each of these lasers prior to combining them. All common mirrors along the vertical axis must also be replaced with broadband coated mirrors³, which are highly reflective at all wavelengths of interest.

In order to accommodate this new design into our existing setup, in particular given the tight

¹Thorlabs DMSP820B 820 nm cutoff shortpass dichroic mirrors.

²We order Semrock 733.95 nm BrightLine single-edge image-splitting dichroic beamsplitters with custom high-temperature annealing; the cutoff band needs to be quite sharp, ~ 30 nm wide.

³Newport dielectric mirrors 20Q620BB.HR2 are high reflectors, broadband coated for 350-1100 nm.

space (\sim 3 inches) below our chamber, we design and machine⁴ custom mounts for mirrors and dichroics as shown in figure 4.2). The challenges of constructing a vertical lattice such as this are primarily engineering in nature, and rely on technical improvements and remodeling of our experiment. These changes, however, are beneficial in the long term, since they result in a more stable and robust setup overall.

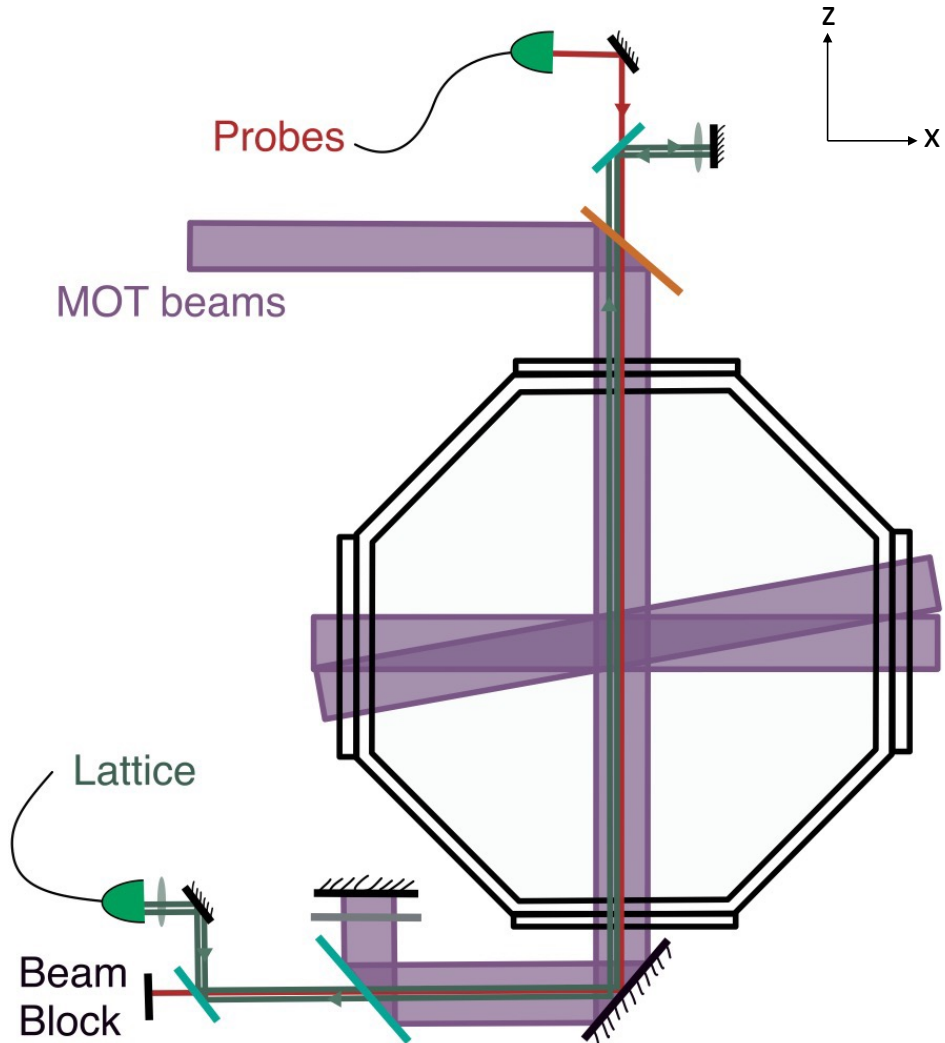


Figure 4.1: Design for a new vertical lattice configuration. Probe (clock) and lattice beams are combined along the vertical axis on dichroic beamsplitters (see main text for details). Probes are fed from above, while the lattice is counter-propagated from below.

⁴We have a lot of help and guidance from Clara Wilson in the Physics Design Lab, who consults and helps machine many of these custom parts.

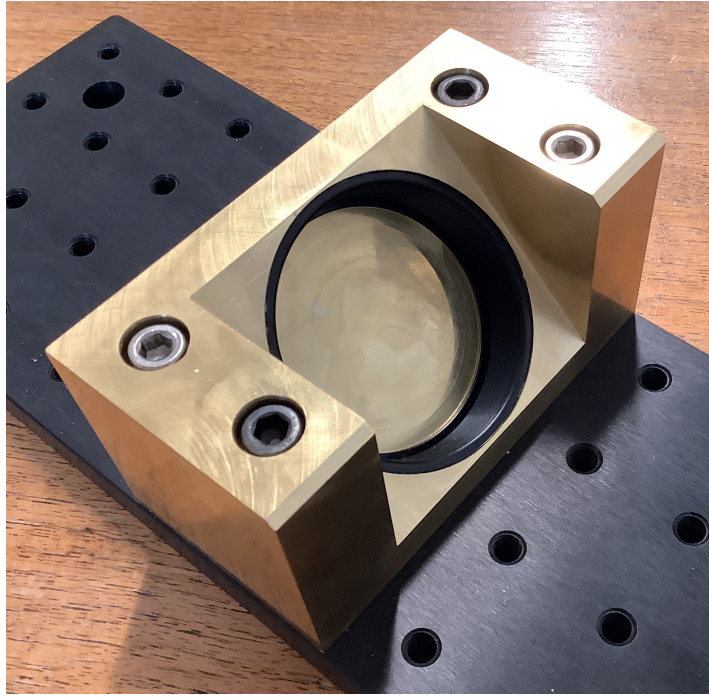


Figure 4.2: Home-designed and machined mirror mount for vertical lattice construction.

4.1.2 A search for a new kind of magic wavelength

In addition to larger systematic light shifts due to the lattice, we suspect that near resonant magic traps are responsible in part for large scattering rates, decreasing the lifetime of our molecules and limiting our fractional uncertainty [32]. In the past, we have seen evidence of nonlinear lattice scattering with intensity, which may suggest two-photon excitation loss of molecules from the lattice through nearby resonant states. This lattice scattering emerges primarily due to our current method for engineering magic-wavelength trapping. As described in section 2.2, we engineer a magic lattice by capitalising on the dispersive change in polarizability near a resonance to match polarizabilities and reduce lattice-induced broadening of the clock transition. As a result, however, our molecules are very sensitive to lattice frequency and intensity stability; since the polarizability changes very quickly near resonance, small changes in lattice intensity or frequency introduce a polarizability mismatch, which artificially broadens the clock transition linewidth [35]. While lower intensity traps begin to mitigate these issues, our reliance on resonant magic wavelengths in our current molecular clock remains a problem.

As noted in the previous chapter (3.2.2), early theories and quantum chemical models predict what we refer to as off-resonant magic polarizabilities (see figure 4.3) [25]. These off-resonant magic polarizabilities are much more similar in nature to those used in atomic systems and would relax our current constraints on lattice stability [84]. In this prediction, pairs of ground potential clock states have naturally occurring equal polarizabilities at lattice wavelengths $\lambda > 1000$ nm.

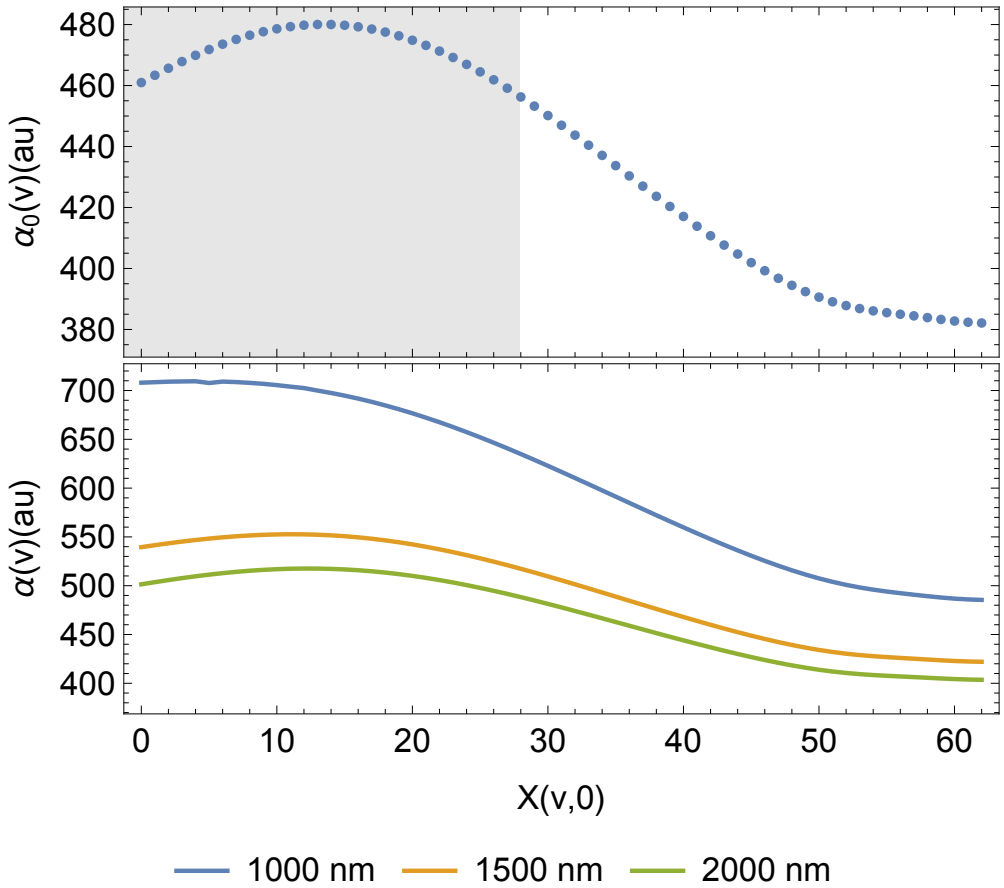


Figure 4.3: Polarizability of the electronic ground vibrational states, as predicted by early theoretical models. These models show potential preferable state pairs for vibrational states $v < 28$ with naturally occurring equal DC polarizabilities, $\alpha_0(v)$ (above). These pairs of states may present favourable clock conditions with near zero BBR shift corrections and significant suppression of lattice-induced scattering. This non-monotonic behaviour emerges at wavelengths longer than 1000 nm, and may offer alternative constructions of a magic IR trap (below).

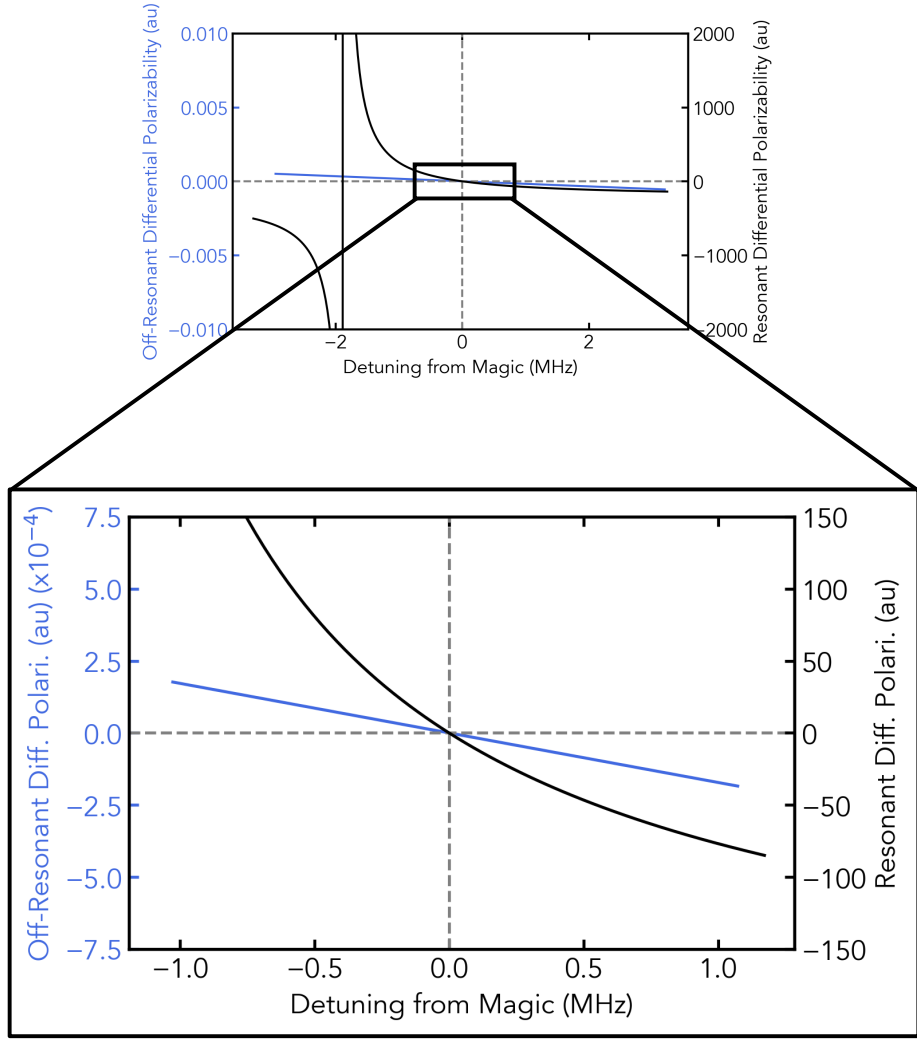


Figure 4.4: A comparison of two magic trapping schemes. Right axis (black) shows the differential polarizability around conventional near-resonant magic wavelength. Left axis (blue) shows the differential polarizability around predicted off-resonant magic wavelengths. The slope of each curve describes the sensitivity of our system to changes in the lattice frequency. Off-resonant magic wavelengths are 10^5 times less sensitive than our conventional traps. Below, we zoom in to region just around the magic condition, while, above, we show proximity to resonance [25].

We are particularly interested in investigating the dynamic polarizability behaviour of our molecules for lattices at $\lambda > 1200$ nm, wavelengths which probe below the 1_u potential and, therefore, do not address any single-photon excited resonances. These near- to mid-IR lattices are attractive candidates for future clock generations since they would strongly mitigate lattice induced scattering through these excited resonances. In particular, if we compare the differential polarizability of two representative examples in both magic wavelength schemes, we find that these new, off-resonant magic states are predicted to be over 10^5 times less sensitive than our conventional magic traps (see figure 4.4).

If we consider, for example, the telecom range (1450-1650 nm) — accessible with current laser technology — we find an array of clock states between $X_g(0, 0)$ and $X_g(21, 0)$ that offer potential attractive clock candidates, whose differential polarizability is naturally zero (see figure 4.5). In fact, our model predicts a potential magic condition to be satisfied every ~ 15 nm, which makes

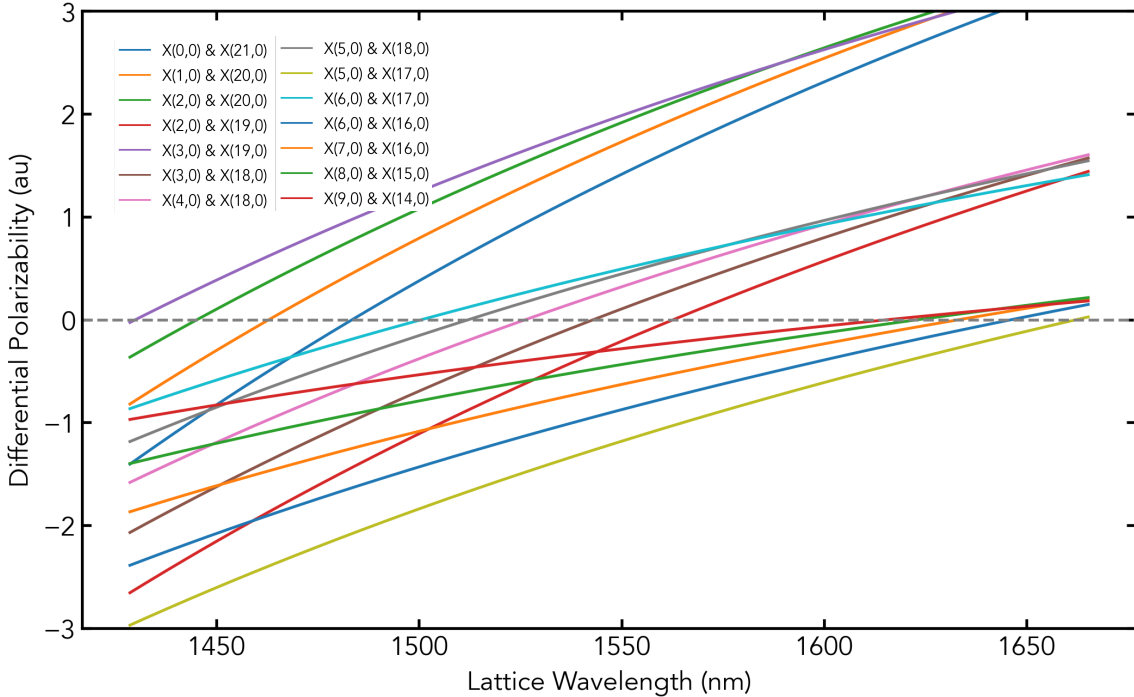


Figure 4.5: Differential polarizability of pairs of clock states in the telecom range (1450-1650 nm). Theory predicts an array of states between $X_g(0, 0)$ and $X_g(21, 0)$, whose differential polarizability is naturally zero. The magic condition is predicted to be satisfied every ~ 15 nm [25].

this region a rich area of study. Should this behaviour be real, it would present an entirely new avenue for a better molecular clock.

These predictions motivate an in-depth study of the polarizability behaviour of our ground state molecules, which I will describe in the following sections. While we ultimately find that these predictions do not match experiment, the results of this study are still important as we make future clock design choices, as well as lay the groundwork for techniques and strategies for more complex measurements. In particular, an improved picture of the polarizabilities leads to a deeper understanding of BBR shifts and uncertainties in the molecule. As we will see later, these future design decisions rely primarily on balancing the fractional uncertainty imposed by a mismatch in polarizability and resulting BBR shift, with the instability introduced by the near-resonant lattice.

4.1.3 A precise measurement of the dynamic polarizabilities of strontium dimers

In order to evaluate the polarizability behaviour of our ground state molecules, we use Stark shift spectroscopy to measure differential light shifts of narrow clock-like transitions in the presence of auxiliary high-intensity 1950 nm light. Specifically, we employ a simplified clock spectroscopy scheme [18] to probe the differential polarizabilities of rovibrational levels, $X_g(v, 0)$, relative to the most weakly-bound, $X_g(62, 0)$, state (see figure 4.6). At 1950 nm, we predict induced light shifts $> 1 \text{ kHz}/100 \text{ mW}$, which is definitively resolvable with our current clock.

As before, our clock-like transitions are two-photon transitions from the least bound vibrational state in the ground electronic potential, $X_g(-1, 0)$, to a more deeply bound vibrational state, $X_g(v, 0)$, via an intermediate state in the electronically excited 0_u^+ potential. The particular 0_u^+ state is selected based on favourable Franck-Condon factors with both the weakly-bound and deeply-bound clock states near the $A^1\Sigma_u^+$ and $C^3\Pi_u$ avoided crossing [39]. Both clock lasers are stabilized in reference to a high-finesse cavity and the frequency comb, while the lattice is locked to the wavemeter. As discussed in section 2.2.2, we can achieve $\sim 1 \text{ kHz}$ linewidths with this locking

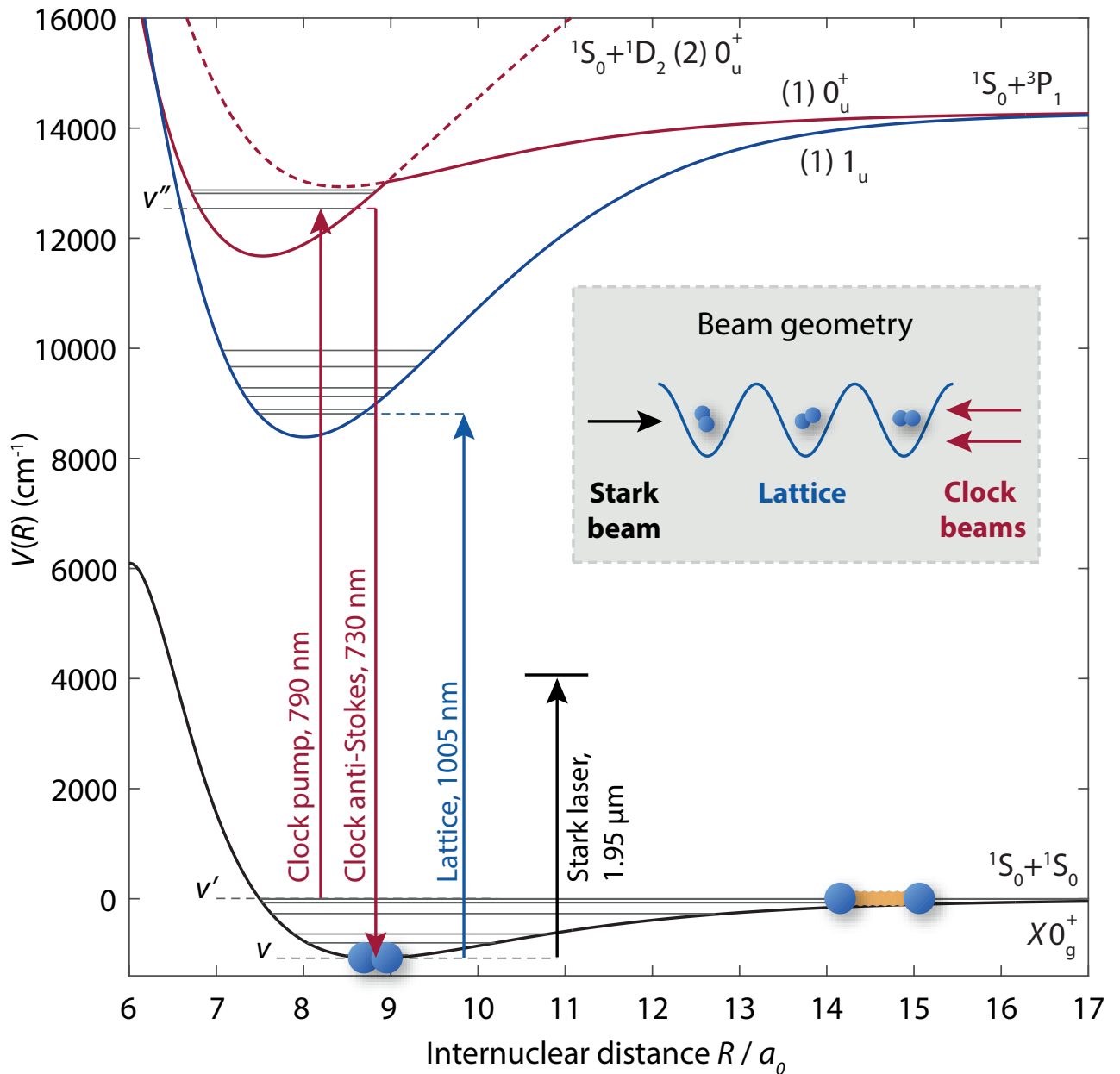


Figure 4.6: A scheme for probing the light shift on a clock transition from a auxiliary 1950 nm light source. We perform spectroscopy of our molecular clock transition using a two-photon Raman transition via an intermediate state in the 0_u^+ (red arrows) in a magic lattice that couples our deeply-bound clock state to an excited 1_u state (blue arrow). We induce Stark shifts to probe differential polarizabilities of ground rovibrational states with 1950 nm light (orange arrow).

scheme, which is sufficient for this investigation.

Our experiment design is fairly simple. We measure the light shift of a transition between $X_g(62, 0)$ and another ground state $X_g(\nu, 0)$ in a magic lattice at various intensities of 1950 nm light. For each state, we measure the light shift at three powers of the 1950 nm probe light. At each power, we scan our clock-like resonance, interrogating with our 1950 nm light for ~ 2 ms; to determine the shift at a given power, we interleave measurements of the transition position with the 1950 nm light on and the 1950 nm light shuttered, and average each peak position over 5 runs (see figure 4.7). Over the course of a light shift measurement, we find 1950 nm power drift up to ~ 10 mW, since we do not actively stabilise the frequency or power of this laser. This drift, however, does not contribute significantly to artificial broadening of our transition linewidth, which remains dominated by frequency instabilities of the lattice around the magic wavelength.

Since we do not have a reliable method for measuring the beam waist and power of 1950 nm

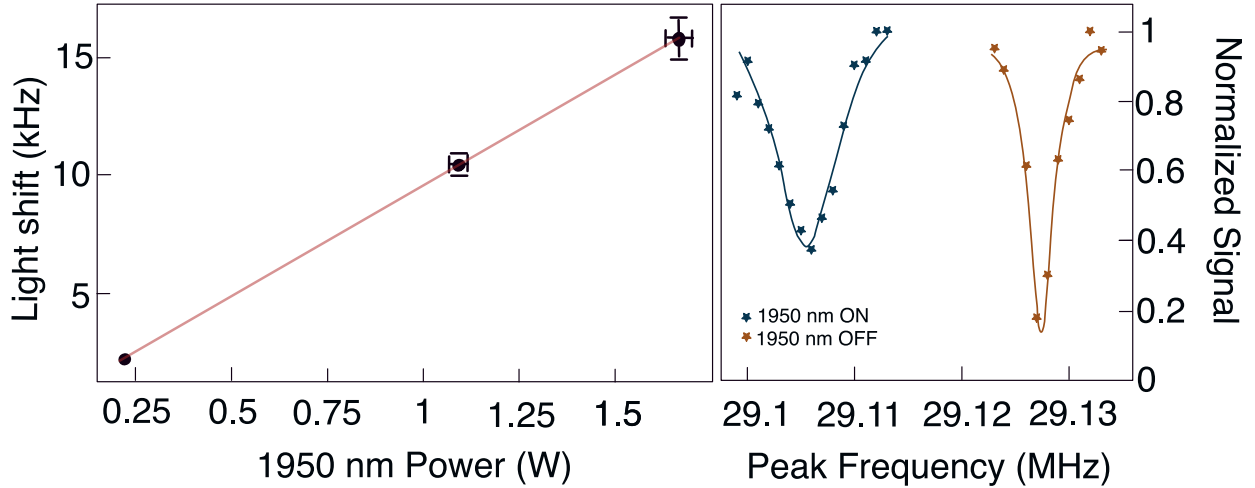


Figure 4.7: Light shift of the $X_g(0, 0)$ state with 1950 nm light. We measure the linear light shift as a function of 1950 nm laser power (left). Each point is measured by interleaving scans of the resonance with the 1950 nm light on and off, and averaging over five runs. An example scan at 1.1 W is shown (right).

light in the chamber, we calibrate the intensity of 1950 nm light at the molecules by measuring the light shift of a reference transition, namely $X_g(62, 0)$ to $X_g(27, 0)$. This transition is, in turn, calibrated to a known atomic line. We reference our light shift measurements to the intercombination line of ^{88}Sr , the $^1\text{S}_0 \rightarrow ^3\text{P}_1$ transition, whose polarizability is 326.16(3.59) a.u. [85]. By directly comparing the light shift on the intercombination line to that of the $X_g(62, 0)$ to $X_g(27, 0)$, we calibrate the effective intensity of 1950 nm light at the molecules (see figure 4.8). In this way, we perform a frequency-only measurement of the differential polarizability of our ground state molecules.

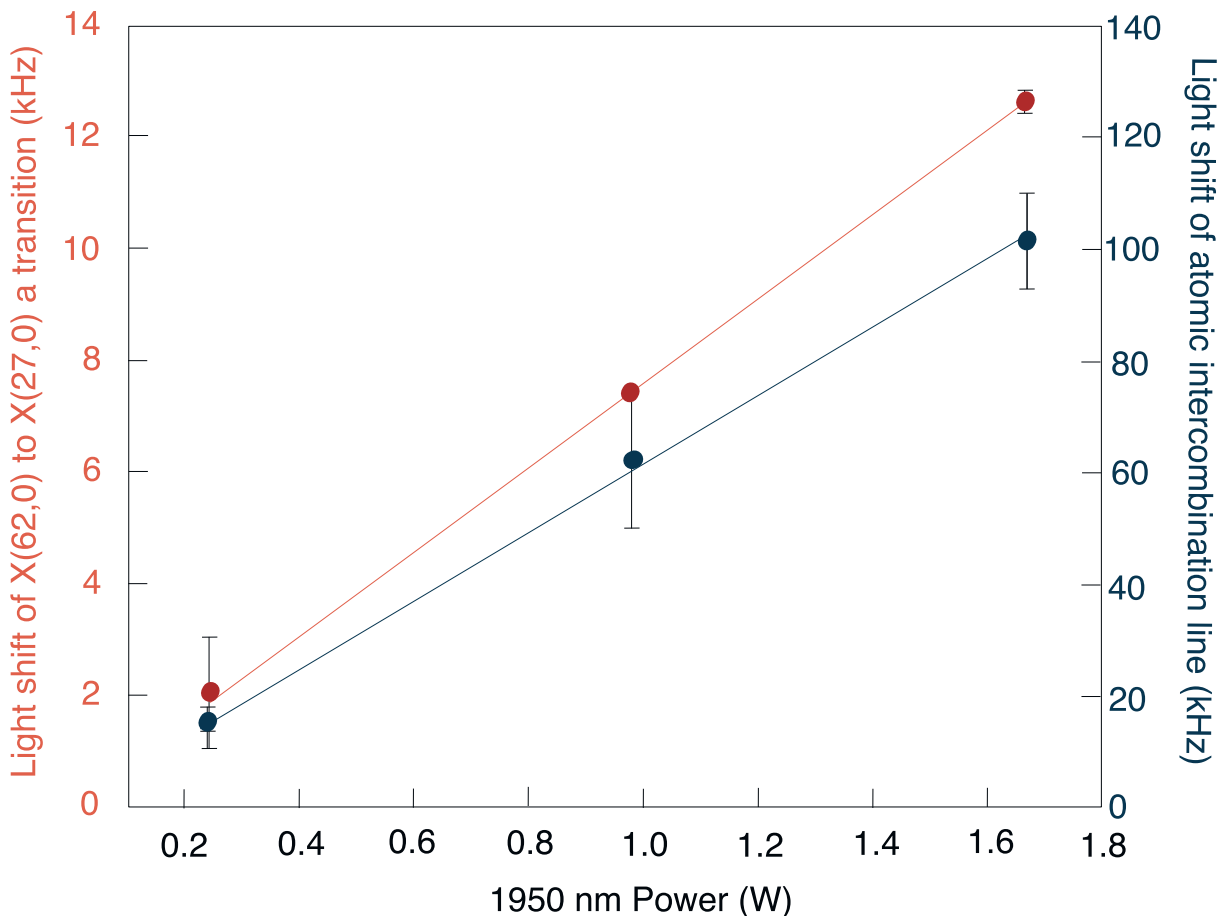


Figure 4.8: Calibration of the 1950 nm light intensity to polarizability of the $^{88}\text{Sr} \ ^1\text{S}_0$ to $^3\text{P}_1$ transition. We calibrate the light intensity by referencing the light shift on the intercombination line (right, blue) to the $X_g(62, 0)$ to $X_g(27, 0)$ transition (left, red).

Table 4.1: Probing the dynamic polarizabilities throughout the electronic ground state. Relevant states, $X_g(v, 0)$, with corresponding binding energies relative to $X_g(62, 0)$, intermediate transition, $0_u^+(v', 1)$ and magic wavelengths and corresponding 1_u states are listed.

$X_g(v, 0)$	$(E_{62} - E_v)/h$ (MHz)	$0_u^+(v', 1)$	λ_{magic} (nm)	$1_u(v', 1)_{\text{magic}}$
61	1 263.680(76)	15	–	–
55	108 214.221(78)	15	–	–
41	2 177 876.735(88)	11	996.4379	23
27	8 075 406.28(10)	11	1006.5787	19
12	19 176 451.65(11)	16	1007.7634	14
7	24 031 492.42(12)	15	1007.1334	12
1	30 640 159.75(12)	11	1016.9714	8
0	31 825 183.17(13)	11	1004.7720	9

We probe a host of vibrational levels sampling the entire electronic ground state potential (see table 4.1). This flexibility requires us to build several different probe lasers, spanning 730-800 nm, and leverage various intermediate states in 0_u^+ excited potential. Additionally, we measured all binding energies to \sim 100 kHz precision, which improves on the precision previously set by our experiment for several of the vibrational states. All told, these measurements span all regimes of the ground potential and help paint a complete picture of dynamic polarizabilities of our molecule.

In order to perform this measurement, we must first spectroscopically locate our states of interest and demonstrate two-photon Raman spectroscopy via a favourable intermediate state. To do so, we use EIT spectroscopy to initially locate the Raman transition frequencies to \sim 100 kHz precision (see section 2.4.1), and then detune both of our clock lasers by +30 MHz to scan our narrow Raman transition. We engineer magic traps by selecting preferable 1_u transitions (see section 2.3.3), and by measuring the lattice light shift near this 1_u transition. We scan the transition at high and low lattice intensities to locate the magic wavelength, which we stabilise to our wavemeter (\sim 100 MHz precision). In order to have long enough clock interrogation times, we require transition strengths $\gtrsim 10^{-5}$ a.u., such that scattering lifetimes are long enough to reach Fourier-limited \sim 1 kHz linewidths.

Probing these dynamic polarizabilities to \sim kHz precision, we find that the results do not agree with the predictions of this early theory [25], but rather show a monotonic behaviour as a function of binding energy (see figure 4.9). As a consequence, we find that these predicted off-resonant magic wavelength conditions cannot be satisfied at 1950 nm, and suggests that these types of naturally-occurring, atom-like polarizability crossings do not exist in our molecule in the IR regime. As I will discuss next, the experimental values are well described by a new, simpler *ab initio* theory.

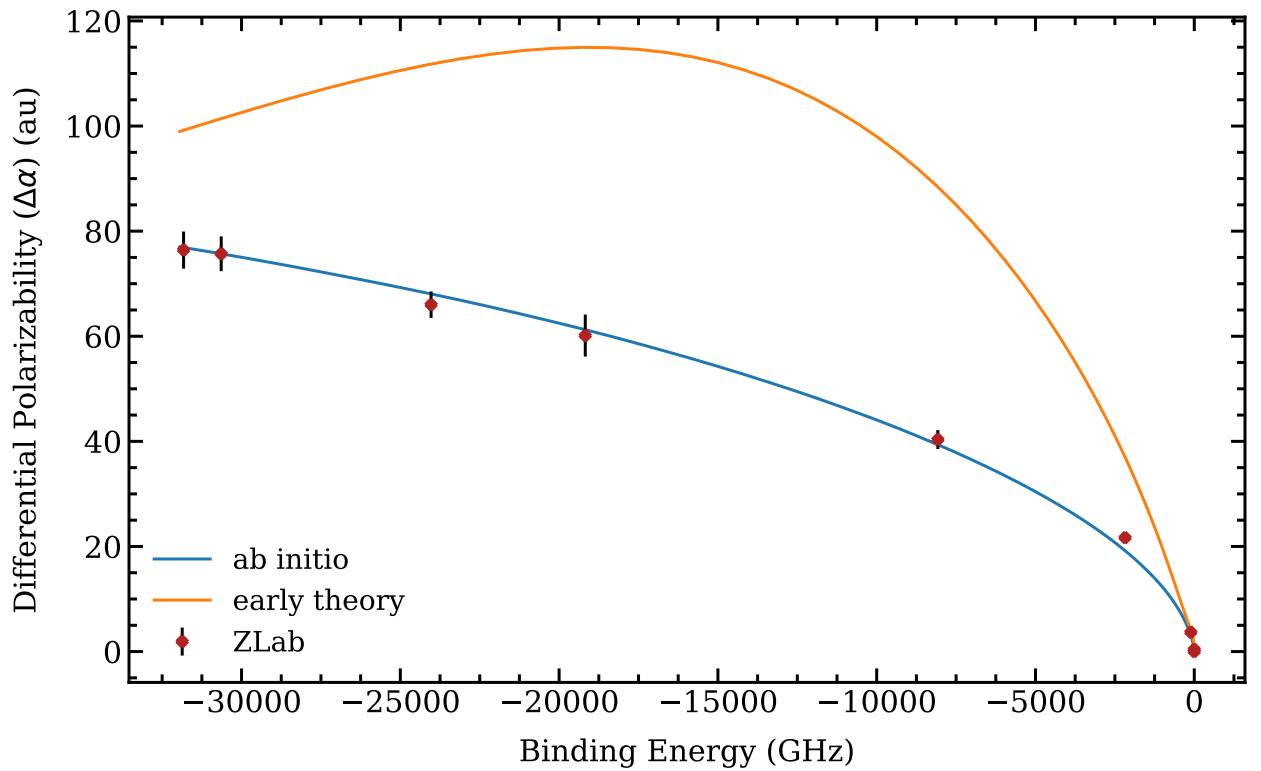


Figure 4.9: Differential polarizability of a set of $X_g(v, 0)$ states with respect to $X_g(-1, 0)$. The states in the ground state show a monotonic behaviour with binding energy, contrary to previous theoretical predictions (orange), which largely overestimate the polarizability difference in our ground state molecule. Comparisons to *ab initio* theory (blue) are in good agreement with experiment (see section 4.1.4 for details).

4.1.4 An improved theoretical picture

The previous polarizability model was derived from a sum-over-states calculation. Conventionally, the polarizability of a state i can be calculated from

$$\alpha_i(\omega) = \frac{2}{\hbar} \sum_{i \neq j} |d_{ij}|^2 \frac{\omega_{ij}}{\omega_{ij}^2 - \omega^2} \quad (4.1)$$

where d_{ij} is the dipole-moment matrix element and ω_{ij} is the transition frequency between state i and state j [86]. The previous model performs the summation over all electronic, vibrational, and rotational quantum numbers, including the rovibrational continua of different, higher-lying excited electronic potentials, and including the spin-orbit coupling contribution between the lowest electronic potentials [25]. In this way, it is a fairly complete study, but it, crucially, relies on precise calculations of excited state binding energies. Contributions of the non-monotonic behaviour come primarily from higher-lying excited potentials, which are notoriously difficult to describe [25]. This may partially explain why the predictions do not adequately reproduce experimental data.

We instead use *ab initio* models⁵ to calculate the dynamic polarizabilities of $^{88}\text{Sr}_2$. While this model does not incorporate any vibrational state-specific information, in homonuclear molecules, the polarizability behaviour is inherited from the electronic structure of the molecule. For any given lattice light frequency ω , we first calculate the interaction-induced polarizability of Sr_2 molecules,

$$\alpha_{ij}^{\text{int}}(\omega; R) = \alpha_{ij}(\omega; R) - 2\alpha_{\text{atom}}(\omega) \quad (4.2)$$

where $\alpha_{ij}(\omega)$ are tensor components of the total molecular polarizability and $\alpha_{\text{atom}}(\omega)$ is the atomic polarizability at frequency ω . Since we are working only with isotropic $J = 0$ states, we take the trace polarizability $\alpha^{\text{int}}(\omega; R) = [\alpha_{zz}^{\text{int}}(\omega; R) + 2\alpha_{xx}^{\text{int}}(\omega; R)]/3$ [90, 91]. We extend the

⁵The *ab initio* model we employ is based on asymmetric analytical derivative of the coupled-cluster energy with single and double excitations (CCSD) [87], as implemented in the Q-Chem 5 package [88]. We use the ECP28MDF pseudopotential together with its dedicated valence basis set [89].

model for large R using a fitted long-range form [92]

$$\alpha^{\text{int}}(\omega; R) \sim A_6(\omega)R^{-6} + A_8(\omega)R^{-8} + A_{10}(\omega)R^{-10} \quad (4.3)$$

Figure 4.10 shows the isotropic component $\alpha^{\text{int}}(\omega; R)$ at $1.95\text{ }\mu\text{m}$ as a function of R . The results are in excellent agreement with the experimental values and show that the induced polarizability is dependent on the wavefunction and chemistry of the particular vibrational state. The R-centroid approximation allows us to estimate the interaction-induced polarizability at the mean internuclear distance \tilde{R}_v of state v using the differential polarizability of a $v \leftrightarrow 62$ transition:

$$\alpha^{\text{int}}(\omega; \tilde{R}_v) \approx -\Delta\alpha_{v \leftrightarrow 62}(\omega), \quad (4.4)$$

where $\tilde{R}_v = \int_0^\infty |\Psi_v(R)|^2 R dR$. This formula neglects the small interaction-induced polarizability of the $v' = 62$ state. Thus, different vibrational transitions effectively serve as probes of polarizabilities, each at a different internuclear separation, as shown in figure 4.10.

Interestingly, we find a sharp increase in the polarizability as we move towards smaller internuclear separations, which can be interpreted as corresponding to some global change in the molecular structure or chemistry. Upon closer inspection, we find that the onset in the sudden change in polarizability corresponds to the LeRoy radius [93, 94], which is defined as

$$R_{LR} = 2[\langle r_A^2 \rangle^{1/2} + \langle r_B^2 \rangle^{1/2}], \quad (4.5)$$

where r_A and r_B denote the radii of the two atoms. In this way, for $r > R_{LR}$, the molecular potential can be reasonably approximated by the component atomic distributions, while for $r < R_{LR}$, a classical or semi-classical picture is no longer valid, and we must consider a full molecular model [93, 95, 96]. More generally, we can interpret the LeRoy radius as corresponding to the formation of a molecular bond and the onset of molecular chemistry.

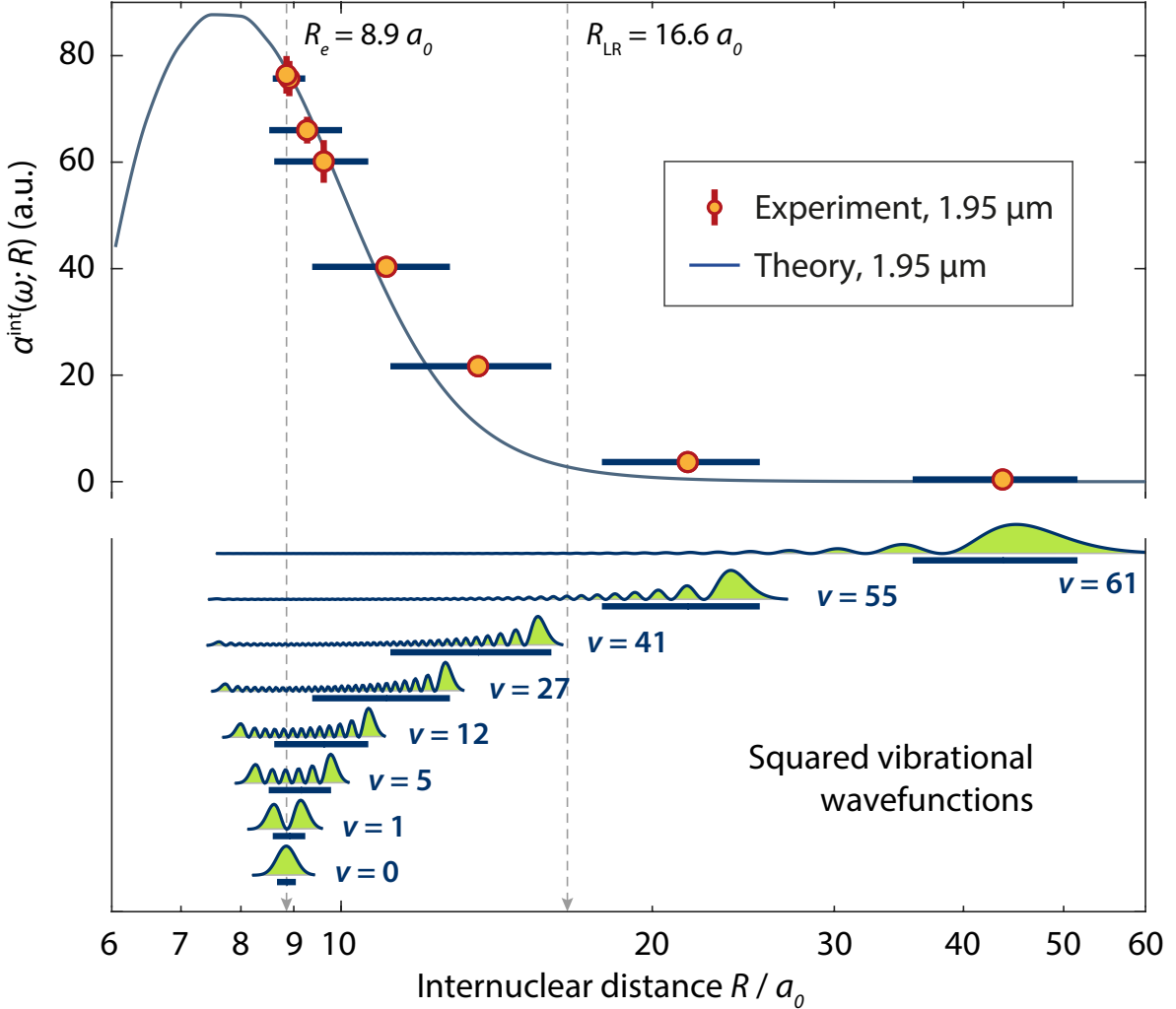


Figure 4.10: Interaction-induced ac polarizability at $\lambda = 1.95 \mu\text{m}$. In addition to the *ab initio* result we show absolute experimental polarizabilities in relation to mean internuclear distances \tilde{R} . Horizontal bars indicate the range $[\tilde{R}_v - S_{R_v}, \tilde{R}_v + S_{R_v}]$ of internuclear distances probed by the vibrational wavefunctions shown in the lower panel. Here \tilde{R}_v and S_{R_v} are the mean and standard deviation internuclear distances for wavefunction squared treated as a probability distribution. R_e and R_{LR} are, respectively, the equilibrium distance and the LeRoy radius [93, 94].

To model the polarizability of each vibrational level v and extend this picture to all infrared wavelengths (see figure 4.11), we average the electronic polarizability $\alpha^{\text{int}}(R)$ over the level's vibrational wavefunction $\Psi_v(R)$:

$$\alpha_v^{\text{int}}(\omega) = \int_0^\infty |\Psi_v(R)|^2 \alpha^{\text{int}}(\omega; R) dR \quad (4.6)$$

where the differential polarizability for a transition $v \leftrightarrow v'$ is

$$\Delta\alpha_{v \leftrightarrow v'}(\omega) = \alpha_{v'}^{\text{int}}(\omega) - \alpha_v^{\text{int}}(\omega) \quad (4.7)$$

We obtain the vibrational wavefunctions by solving the radial Schrödinger equation, $[-\frac{\hbar^2}{2\mu} \frac{d^2}{dR^2} + V(R)]\Psi_v(R) = E_v \Psi_v(R)$ using a matrix discrete variable representation (DVR) method [97, 98].

We use an accurate molecular potential $V(R)$ derived from Fourier-transform spectroscopy [31], and the reduced mass μ equals half the mass of a Sr atom.

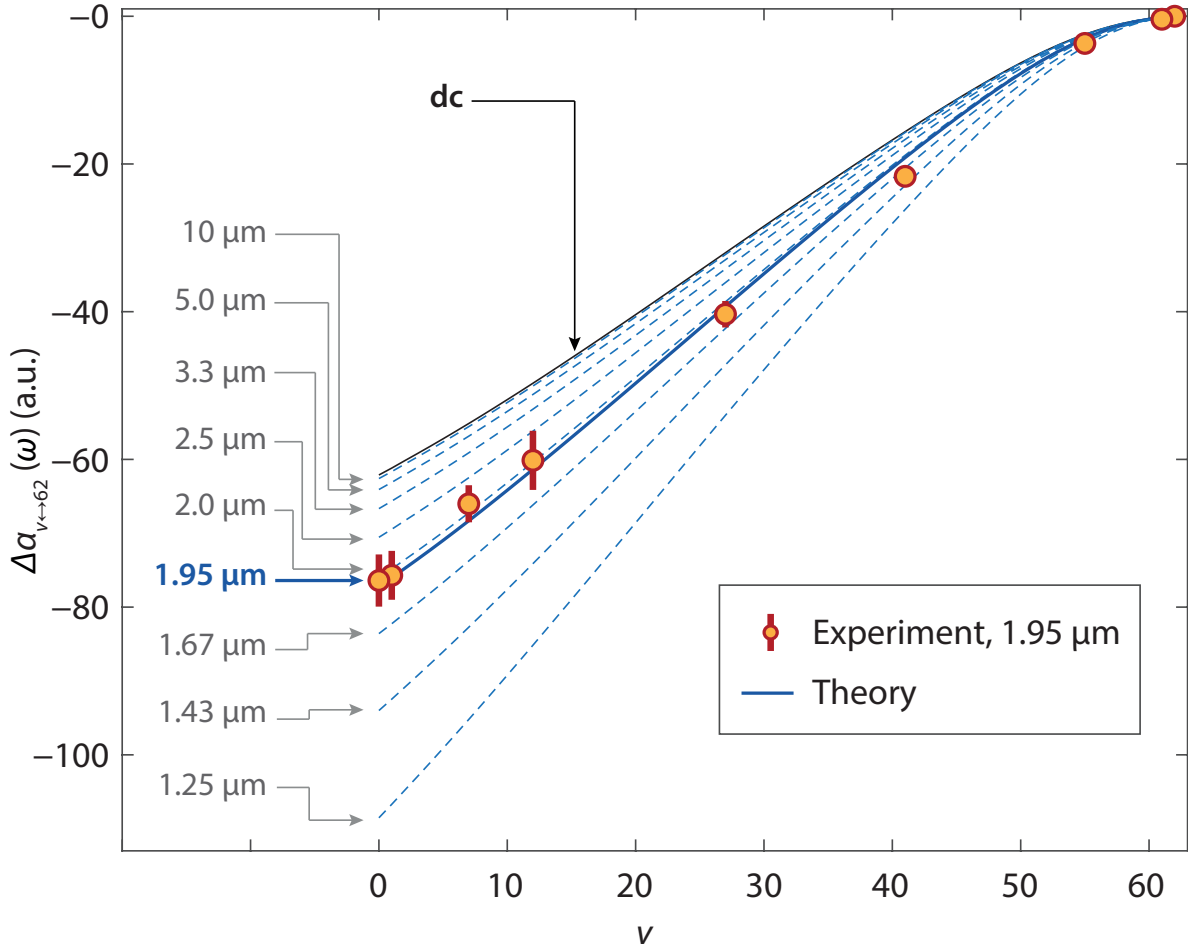


Figure 4.11: Differential polarizability with respect to the least-bound $v = 62$ state in ground state Sr_2 . Points denote experimentally measured ac polarizabilities at $\lambda = 1.95 \mu\text{m}$. Lines are *ab initio* polarizabilities from dc to $\lambda = 1.25 \mu\text{m}$.

Again, the calculated differential dc and ac polarizabilities for $v \leftrightarrow 62$ transitions match experimental values at 1950 nm (figure 4.11). Importantly, the monotonic behaviour seen experimentally persists at all IR wavelengths. It should be noted that this approach to theoretically extend our model is valid only when the adiabaticity condition is maintained, that is, that the ground-state potential does not cross any of the excited-state potentials if shifted upwards by the lattice photon energy. In Sr_2 , the adiabaticity requirement limits the photon wavenumber to about 8000 cm^{-1} ($1.25 \mu\text{m}$). Both our ac Stark shift measurements 5128 cm^{-1} ($1.95 \mu\text{m}$) and the dominant spectral energy density of room temperature BBR are well within this margin.

This model provides us with two complementary descriptions of the ground state dynamic polarizabilities: (1) as a function of vibrational state, and (2) as a function of internuclear separation, or effective bond length. As we experimentally probe various vibrational states, we explore various depths of the ground potential. While this new picture does not predict off-resonant magic lattices, it reproduces our experimental data remarkably well (see table 4.2) and, as a consequence, we have gained a more complete understanding of our molecule through this study. In particular, we can more definitively predict the size of the fractional uncertainty, or broadening, of the clock linewidth that we expect in a non-magic lattice. Since it is technically simpler to confine our molecules in a non-magic trap, depending on the size of this fractional uncertainty and the particular experiment of interest, we may still benefit from leveraging this strategy. I will further discuss these implications in the final section of this chapter.

Table 4.2: A comparison of experimental differential polarizabilities to *ab initio* theory.

$X_g(v, 0)$	$\Delta\alpha_{v,62}^{\text{exp}}$	$\Delta\alpha_{v,62}^{\text{th}}$
61	-0.41(0.52)	-0.13
55	-3.68(0.38)	-3.01
41	-21.67(0.88)	-19.10
27	-40.4(1.8)	-39.3
12	-60.1(4.0)	-61.3
7	-66.0(2.5)	-68.3
1	-75.7(3.3)	-76.0
0	-76.4(3.6)	-77.2

4.2 Suppressing BBR Shifts in Homonuclear Molecules

The overwhelming majority of the BBR spectral energy density, the light radiation that contributes to the BBR shift, falls below $2 \mu\text{m}$. As such, in order to determine the corresponding BBR shifts of our molecule, we leverage this model of the differential polarizabilities at all wavelengths from dc to infrared. While we cannot experimentally probe this entire range of wavelengths, we rely on close agreement between theory and experiment at $1.95 \mu\text{m}$ to validate and extend theoretical models to provide a full description of the BBR shift.

The key test of our model relies on a direct comparison and strong agreement of measured molecular differential polarizability at $1.95 \mu\text{m}$ with the calculated values (see table 4.2). For example, the theoretical differential polarizability for the $0 \leftrightarrow 62$ clock transition, $\Delta\alpha_{0\leftrightarrow 62}(\omega)$, is -77.2 a.u. compared to the experimental value of $-76.4(3.6) \text{ a.u.}$. As we move to more deeply bound target states, the differential polarizabilities increase monotonically as they pick up additional polarizability induced by molecular interactions and chemistry.

The range of investigated target levels from the ground $v = 0$ state to the second-to-least bound $v = 61$ state spans internuclear distances from $8.86 a_0$ (approximately the equilibrium distance R_e) to $43.6 a_0$. To estimate the relative uncertainty of our theoretical model, we fit it to the experimental data by simple scaling. The best least-squares fit is achieved by scaling the model up by $+1.8(2.4)\%$. This, however, is compatible with zero, implying that no model scaling is necessary.⁶ Nevertheless, to estimate the accuracy of our theoretical model, we combine the 2.4% uncertainty from the scaling factor with an additional 1.8% possible systematic error to obtain a “Type B” uncertainty [99] of 2.6% .

In order to adequately characterise the BBR shift on our clock line, we need to fully consider

⁶In fact, the reduced chi-square $\chi^2/\text{dof} = 1.78$ for the scaled model ($\text{dof} = 7$) is worse than $\chi^2/\text{dof} = 1.69$ ($\text{dof} = 8$) for the original, unscaled model.

the shift induced at all wavelengths of the BBR spectrum. The BBR-induced shift $\Delta f_{v \leftrightarrow v'}$ can be expressed as an ac Stark shift integrated over the BBR spectrum [73, 100, 101]:

$$\Delta f_{v \leftrightarrow v'} = -\frac{1}{2h} \int_0^\infty \frac{4\pi}{\epsilon_0 c} B_\omega(T) \Delta \alpha_{v \leftrightarrow v'}(\omega) d\omega, \quad (4.8)$$

where the spectral radiance of the BBR field at temperature T is

$$B_\omega(T) = \frac{\hbar \omega^3}{4\pi^3 c^2} \frac{1}{\exp(\hbar \omega/k_B T) - 1}. \quad (4.9)$$

Typically, BBR shifts for atomic clocks are determined using a sum-over-states approach to calculate the static and dynamic terms [36, 86, 100–102], but here we already have computed the dynamic polarizabilities, so we can directly integrate the BBR shift. Since most of the BBR spectral energy density falls below any resonance frequencies in our system, we expand the polarizability in terms of Cauchy coefficients [86]: $\Delta \alpha_{v \leftrightarrow v'}(\omega) = \Delta \alpha_{v \leftrightarrow v'}^{(0)} + \Delta \alpha_{v \leftrightarrow v'}^{(2)} \omega^2 + \Delta \alpha_{v \leftrightarrow v'}^{(4)} \omega^4 + \dots$ that we fit to tenth order to numerically calculated polarizabilities [figure 4.12(a)]. This allows us to express the BBR shift as a series:

$$\Delta f_{v \leftrightarrow v'} = \sum_{n=0,2,\dots} \Delta f_v^{(n)} = \sum_{n=0,2,\dots} -\frac{c_n \Delta \alpha_{v \leftrightarrow v'}^{(n)}}{4\pi^3 \epsilon_0 c^3} \left(\frac{k_B T}{\hbar} \right)^{4+n}, \quad (4.10)$$

where the Planck integrals $c_n = \int_0^\infty u^{3+n}/(e^u - 1) du$ are given in table 4.3. The leading term is the well known static contribution to the BBR shift [36, 73], while further terms constitute a dynamic correction η on the order of 0.5–0.6 % (table 4.3). Terms beyond the second order are negligible.

Table 4.3: Contributions to the BBR shift at 300 K for the $0 \leftrightarrow 1$ and $0 \leftrightarrow 62$ transitions.

n	c_n	$\Delta f_{0 \leftrightarrow 1}^{(n)}$ (Hz)	$\Delta f_{0 \leftrightarrow 1}^{(n)}/f_{0 \leftrightarrow 1}$	$\Delta f_{0 \leftrightarrow 62}^{(n)}$ (Hz)	$\Delta f_{0 \leftrightarrow 62}^{(n)}/f_{0 \leftrightarrow 62}$
0	$\pi^4/15$	+0.0081	$+6.8 \times 10^{-15}$	+0.53	$+1.7 \times 10^{-14}$
2	$8\pi^6/63$	$+6.1 \times 10^{-5}$	$+5.1 \times 10^{-17}$	+0.0033	$+1.0 \times 10^{-16}$
4	$8\pi^8/15$	$+6.5 \times 10^{-7}$	$+5.5 \times 10^{-19}$	$+6.3 \times 10^{-5}$	$+2.0 \times 10^{-18}$
η (%)		0.54		0.62	

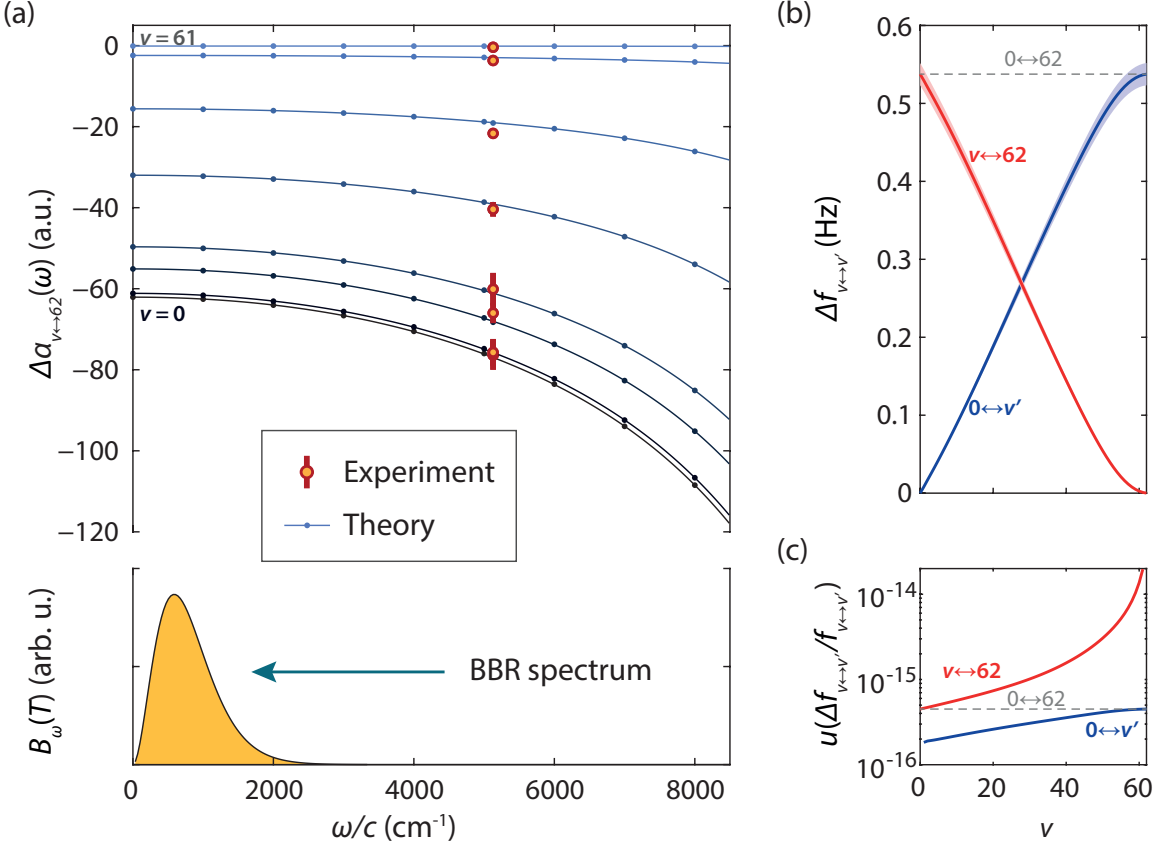


Figure 4.12: (a) Differential polarizabilities for the selected clock transitions. Below, a plot of a BBR spectral radiance $B_\omega(T)$ at 300 K. (b) Absolute BBR shift for $0 \leftrightarrow v'$ clock transitions. (c) Relative BBR uncertainty for the same clock configurations.

Since the molecular clock uniquely provides an array of available clock states, we calculate the BBR shift for other clock transitions. In figure 4.12(b), we plot the BBR shift for $v \leftrightarrow 62$ transitions, $\Delta f_{v \leftrightarrow 62}$ (red line). The BBR shift for our previously measured clock transition [18], $\Delta f_{0 \leftrightarrow 62}$, is +538 mHz with a fractional uncertainty of 4.7×10^{-16} . We further find that the fractional uncertainty of the BBR shift can be reduced by strategically selecting $0 \leftrightarrow v'$ clock transitions (blue line) between deeply bound vibrational states [figure 4.12(c)]. This configuration could allow the fractional uncertainty to be as low as 1.8×10^{-16} , a factor of ~ 2.5 lower than the $0 \leftrightarrow 62$ transition. This provides a promising pathway toward a BBR-suppressed clock configuration.

4.3 Shielding Against Collisional losses

In addition to constructing a new vertical lattice and suppressing the BBR effect, we still need to contend with the inherent two-body losses from molecular collisions in the trap. Currently, our linewidths are Fourier-limited to 5 Hz due to our ~ 200 ms lifetime in the ground state [47]. The key to mitigating shortened molecular lifetimes from collisions is to reduce the density or increase confinement volume of molecules in our experiment. We, however, must consider methods to reduce trap density, while still maintaining large enough signal-to-noise to make a compelling clock measurement.

In our previous clock experiment, we already demonstrated a near $1 N_{mol}/\text{site}$ measurement [18]. We can further shield our molecules from collisions by implementing a wider 1D vertical lattice, that is, by expanding the lattice beam width, such that we have larger, less dense pancakes of molecules. This can be easily implemented in conjunction with the construction of a new vertical lattice. Future iterations of the clock may implement even tighter confinement to shield against collisions, including 3D lattices or tweezer-like traps.

Many other groups have implemented these strategies with success. For instance, by directly loading molecules into a deep 3D optical lattice, two-body losses are suppressed resulting in trapping lifetime of nearly 25 s in a low filling lattice [51]. This suggests that we could easily improve our lifetimes by an order of magnitude, which would allow us to access sub-Hz precision on our molecular clock.

4.4 A Proposal for an Improved Molecular Clock

As we seek to combat these issues in our current clock system, we turn our focus primarily to the design of our lattice and our choice of clock states. One crucial limitation to this magic wavelength configuration is that our clock state lifetimes are limited due to lattice-induced scattering,

which imposes a Fourier limit on the clock linewidths [18]. In order to increase our clock state lifetimes, we hope to engineer our lattice further away from excited transitions, while, additionally, lowering the overall intensity and density of the trap.

While we cannot perfectly satisfy a magic condition with an off-resonant lattice, one approach is to build magic wavelength traps away from resonances between deeply bound vibrational states with *similar enough* polarizabilities in an IR lattice, such as a 1550 nm or 1950 nm lattice. Again, this wavelength sits well below any vibrational states in excited electronic potentials, and so, at this wavelength, the lattice-induced scattering would be greatly reduced. Nevertheless, the clock will suffer thermal broadening in this non-magic trap due to the mismatch in polarizability of the two states, given that there are no natural polarizability crossings at this wavelength. Previously, we demonstrated that, if molecules can be trapped and probed in the Lamb-Dicke (LD) and resolved-sideband (RSB) regimes of an optical lattice, the temperature, T , is determined from the linewidth of the main carrier transition [35]. Assuming the temperature of our sample, we can, in turn, infer the resulting inhomogeneous broadening of the linewidth of our transition, given the polarizabilities of the two states.

A deeply bound $X_g(0, 0)$ to $X_g(\nu, 0)$ clock requires us to initialise the population in the absolute ground state, $X_g(0, 0)$, via STIRAP [47], and then scan the two-photon transition to an excited vibrational state, $X_g(\nu, 0)$. The $X_g(0, 0) \rightarrow X_g(1, 0)$ transition is the best candidate for this clock configuration since it has the smallest natural polarizability mismatch, $\Delta\alpha \sim 0.7(0.1)$ a.u. We simulate the expected lineshape of such a clock transition, accounting for the inhomogeneous broadening due to the difference in polarizability to gain insight into the precision of this clock. Specifically, we are interested in probing whether this inhomogeneous thermal broadening is more significant than near-resonance effects in our conventional clock.

Using the results from *ab initio* theory for the polarizabilities of the $X_g(0, 0)$ and the $X_g(1, 0)$

states, as given in table 4.2, we predict the size of this inhomogeneous broadening. At our operational temperature of $2 \mu\text{K}$, the projected linewidth of an $X_g(0, 0) \rightarrow X_g(1, 0)$ clock in a non-magic lattice would be ~ 100 Hz. Given a transition frequency of 1.185 THz between these two states, the fractional uncertainty of the clock transition ($1/Q$) is 8.439×10^{-11} . We compare this precision to the current record for the $X_g(62, 0)$ to $X_g(0, 0)$ transition at near-magic condition (as configured in [18]), which gives a fractional uncertainty of 3.39927×10^{-13} before averaging. In fact, this new clock only outperforms our current clock at very low, $\sim \text{nK}$, temperatures, which are inaccessible in our system (see figure 4.13).

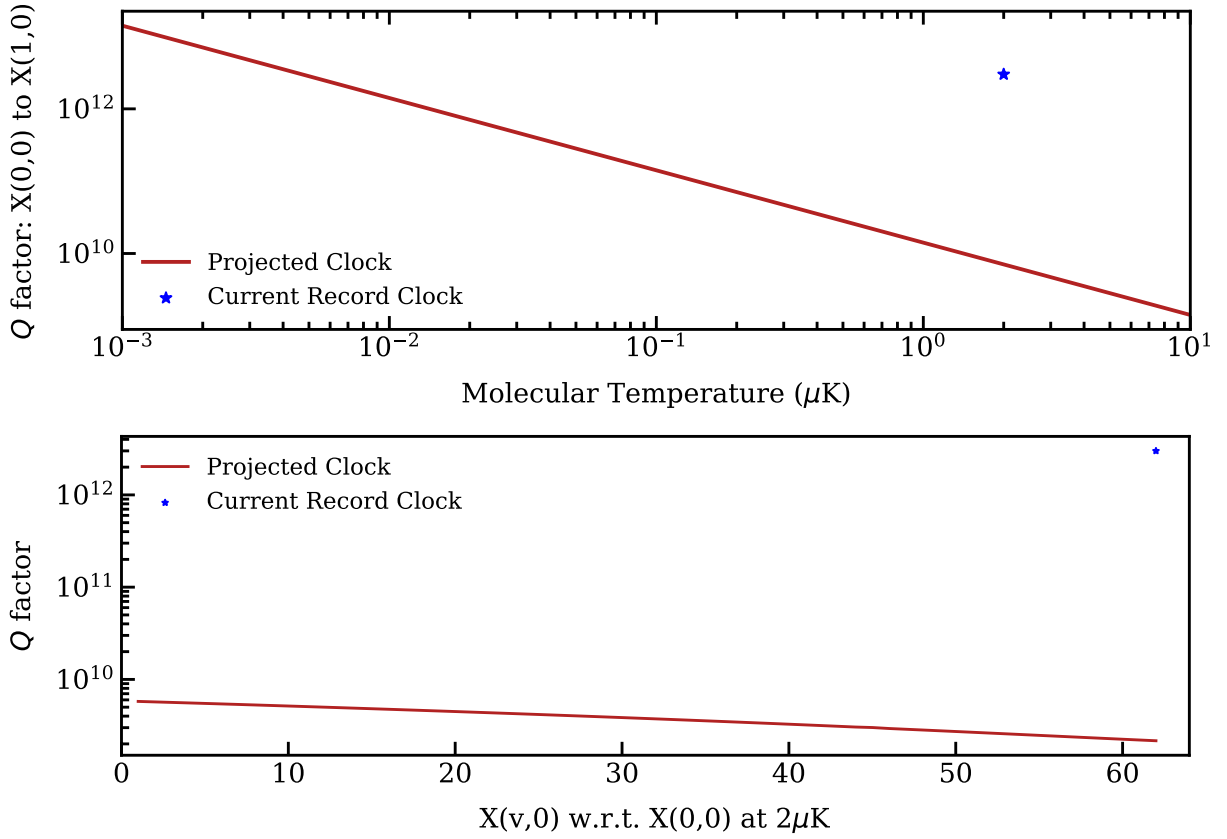


Figure 4.13: Projected Q factor for a non-magic deeply-bound clock construction. We compare the Q factor of a non-magic $X_g(0, 0)$ to $X_g(1, 0)$ with our current record clock at various temperatures (above). This new clock only outperforms our current clock at very low temperature, $\sim \text{nK}$. At $2 \mu\text{K}$, the $X_g(0, 0)$ to $X_g(1, 0)$ clock, which has minimum polarizability mismatch, offers the best Q factor, still orders of magnitude lower than our current clock. We conclude that non-magic clocks are not a viable option for the highest-precision experiments.

Additionally, we can extend this study to all other $X_g(0, 0)$ to $X_g(v, 0)$ clock transitions. We calculate the Q factor for a range of possible pairs of states in the off-magic configuration assuming molecules at 2 μK , and find that the fractional uncertainty is significantly worse than that for our current configuration. This indicates that the increase in inhomogeneous broadening of the line-shape due to the difference in polarizability is greater than the linewidth narrowing due to longer scattering lifetimes (see figure 4.13).

While these results may seem dire, clocks with a non-magic, off-resonant lattice can still allow for sub-kHz spectroscopy, but at a fraction of the technical challenges. In fact, many complex clock measurements that probe interesting concepts or aspects of our molecules can be carried out at this level. The polarizability measurement already described is just one example of this type of measurement, which did not require the level of technical control described in chapter 3. In some cases, the gain in technical simplicity outweighs the loss in precision from the instability and inhomogeneous broadening introduced by the non-magic trap. Particular experiments may, therefore, favour this approach, at least at a first pass.

Finally, we leverage our new theoretical picture to consider alternative resonant magic clock configurations. Using a fairly naive picture as an extension of our 1950 nm model at 1000 nm, we can infer the behaviour of the polarizabilities and predict magic wavelengths and corresponding scattering rates. Specifically, we estimate the polarizability of other clock states in this region by using our measured differential polarizability, $\delta\alpha_{62,0}$, between $X_g(0, 0)$ and $X_g(62, 0)$ at 1000 nm, and assume a linear dependence on polarizability with vibrational quantum number, $\delta\alpha/\delta v$ (see figure 4.14). This decision is motivated by our measurements at 1950 nm, where the polarizability of vibrational states shows a hockey-stick-like behaviour (see figure 4.11), but which can be adequately approximated by a line, especially for weakly-bound states.

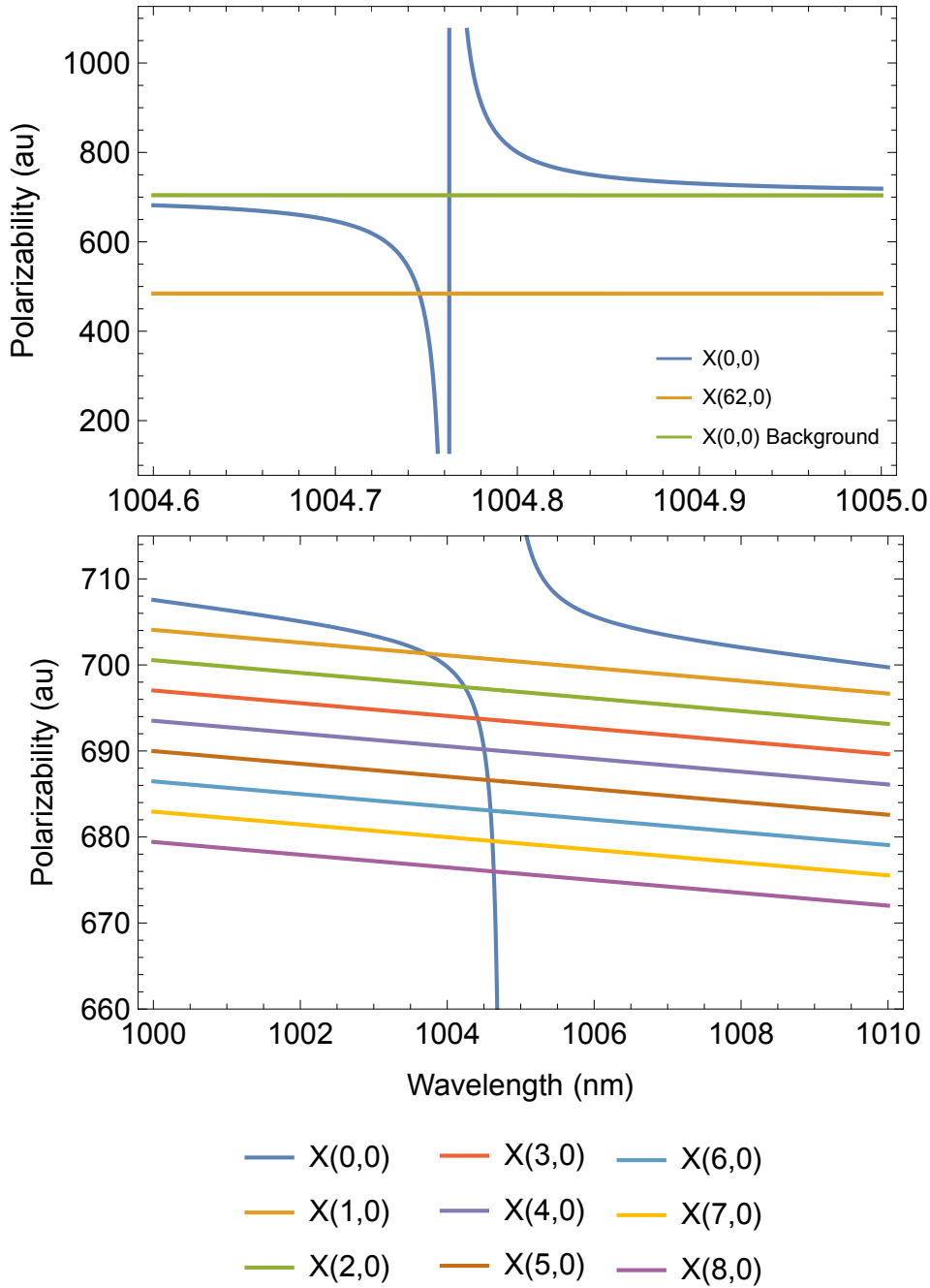


Figure 4.14: Modeling the polarizability behaviour of $X_g(0, 0)$ and $X_g(v, 0)$ in near-resonant magic traps. We plot the resonant behaviour of $X_g(0, 0)$ polarizability around the $1_u(9, 1)$ excited resonance and fit a line to model the background polarizability (above) [25]. The intersection with the $X_g(62, 0)$ occurs at 4.49 GHz detuned from resonance as measured in our experiment [18]. We estimate the polarizability of other clock states in this region using $\delta\alpha_{62,0}$ and assume a linear $\delta\alpha/\delta v$. Since $R_{scatt} \sim 1/\Delta^2$, we predict magic detunings for other clock states in order to capitalise on improvement in molecular lifetime.

As described in section 2.3.1, since $R_{scatt} \sim 1/\Delta^2$, if we simply double the size of our magic detuning, Δ , we should expect a factor of 4 improvement in the scattering rates. There is a lot of potential stability to be gained by using more deeply bound states, despite the tradeoff in the overall size of the transition. In fact, we find two orders of magnitude improvement in the Q factor of a resonant magic $X_g(0, 0)$ to $X_g(1, 0)$ clock (see figure 4.15). This clock configuration has the added advantage of the smallest overall BBR shift and smallest corresponding fractional uncertainty. What is more, a variety of deeply bound state pairs promise an order of magnitude better Q factors due to these larger magic detunings that mitigate lattice scattering. This construction, in combination with other proposed improvements, serves as a promising pathway forward towards our second generation molecular clock.

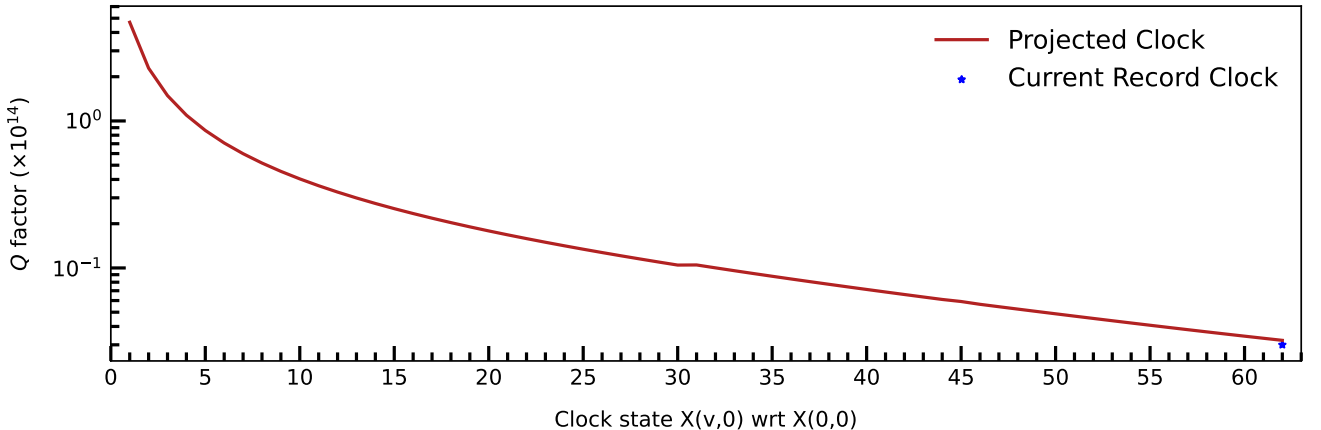


Figure 4.15: Projected Q factor of $X_g(0, 0)$ to $X_g(v, 0)$ in near-resonant magic traps. We find two orders of magnitude improvement in the Q factor of a resonant magic $X_g(0, 0)$ to $X_g(1, 0)$ clock over our current clock.

Chapter 5: Improving Constraints on Non-Newtonian Gravity

5.1 Probing Mass-Dependent Interactions

5.1.1 Isotopologues of strontium as a testbed for ultrashort-range gravity

In our entire discussion, we have focused on methods to better understand the spectroscopic landscape of our molecule. These spectra are, in a way, the characteristic signature of each atom and molecule. We use spectroscopy, and changes in the spectra, as a way to probe fundamental physics because they are highly sensitive testbeds for the environment or any changes in it. What is more, atoms and molecules offer a flexible lego-like platform for tailor-made and designed experiments to investigate new physics at low energies.

When searching for extensions or corrections to mass-dependent forces, such as gravity, leveraging different isotopes or isotopologues, that is atoms or molecules with a different number of neutrons and a different mass, is a natural solution. Specifically, since these isotopes all have the same number of electrons and, therefore, share a similar electronic structure, different isotopes exhibit nearly identical chemical and spectroscopic features. Of course, changes in the neutron number of an atom affects both the nuclear size and mass of a particular isotope. These changes result in shifts in the spectra of the atom, although these shifts can be quite subtle, particularly for heavier elements. Regardless, we can quantify the isotope shift for two isotopes of an atom with total atomic mass A' and A as

$$\delta\nu_{IS}^{AA'} = \delta\nu_{FS}^{AA'} + \delta\nu_{MS}^{AA'} \quad (5.1)$$

where the overall isotope shift (IS) is comprised of a field shift (FS), a shift that arises due to the

volume change and resulting change in charge distribution, and a mass shift (MS), which arises from the additional mass in heavier isotopes [103]. We conventionally write this as

$$\delta\nu_{IS}^{AA'} = F\delta\langle r^2 \rangle^{AA'} + K \frac{M_{A'} - M_A}{M_{A'} M_A} \quad (5.2)$$

where F and K are the field shift and mass shift factors, where these factors are related to the change in atomic radius and the relative mass difference [104]. In reality, it is difficult to separate these terms from one another and isolate or quantify extra shifts due solely to mass-dependent forces on an atom or molecule. King linearity, or King plot analysis, is one proposed method to quantify non-linear isotope shifts that could indicate new forces [105].

In our case, we plan to begin with a different approach to understand these extra shifts in the spectra of our molecules. We will treat these corrections to gravity as small perturbations in the potential energy component of the Hamiltonian that governs the system. We can, therefore, describe small changes in the energy of specific eigenstates of the Hamiltonian, which arise from this perturbation. As mentioned previously, there is particular interest currently on Yukawa-type corrections to Newtonian gravity at short separations [11, 23], wherein the gravitational potential between two point masses experiences an additional large exponential term at short ranges (as in equation 1.5).

In order to quantify the energy shift that results from this perturbation, we consider a Hamiltonian \mathcal{H} governing the overall behaviour of the system and add a perturbative potential due to the Yukawa-type correction, \mathcal{H}_1 , where

$$\mathcal{H}_1 = V_{\text{Yukawa}} = -\frac{Gm_1m_2}{r}\alpha e^{-r/\lambda} \quad (5.3)$$

In our specific system, we have robust theoretical models, as previously shown, that describe the wavefunctions of the ground rovibrational states of our molecules to a good approximation [57].

These models can provide the wavefunctions for all bosonic isotopologues of strontium, which we would be interested in studying in our system. Given these state wavefunctions, we can define the first-order perturbation of the energies of each vibrational state, v , as

$$\Delta E_v = \langle v | \mathcal{H}_1 | v \rangle = \langle v | V_{\text{Yukawa}} | v \rangle \quad (5.4)$$

This state-specific change in energy imparts an overall shift in the clock frequency measured between two vibrational ground states. If we consider two states, v and v' , the overall shift in the measured clock frequency from a Yukawa-type correction is

$$\delta f_{\text{Yukawa}} = (\Delta E_v - \Delta E'_{v'})/h \quad (5.5)$$

In this way, we define the *extra* shift — that is, any anomalous shift in addition to the expected isotope shift — between two isotopologues of strontium with total atomic mass A' and A as the frequency difference of the shift between the same clock transitions in the two isotopologues

$$\delta \nu_{IS}^{\text{Yukawa}} = \delta f_{\text{Yukawa}}^A - \delta f_{\text{Yukawa}}^{A'} \quad (5.6)$$

In other words, by performing a clock measurement for two or more different isotopologues of strontium, we can search for any additional shifts as indicators of a fifth-force or correction to gravity. In so doing, we can continue to constrain the size of such corrections by pushing the limits of the precision and accuracy of our molecular clock.

5.1.2 Making ${}^{86}\text{Sr}_2$ molecules

Before we can measure the isotope shift in strontium, we need an ultracold sample of ${}^{86}\text{Sr}_2$. In our system, we have already successfully demonstrated high levels of quantum control over ${}^{88}\text{Sr}$ dimers, have measured a molecular clock transition to record precision and have described avenues for improved precision in subsequent clock constructions. With this established architecture, we

can now design a protocol for cooling and trapping ^{86}Sr , the next most abundant bosonic isotope, as we move towards making an isotope shift measurement of our clock transition as a mechanism towards improving the constraints set on Yukawa-type corrections to gravity.

First and foremost, we need to establish a new cooling and trapping scheme that accounts for isotope shifts in the atomic spectra. As described in section 5.1.1, the spectrum of the atom will change as a result of both field and mass shifts from the change in neutron number. The spectrum of bosonic isotopes of strontium has been extensively studied [106–108], which provides a starting point for our experiment design. We are particularly interested in quantifying the isotope shifts for the main and narrow-line cooling transitions, corresponding to the formation of the blue and red MOTs. Isotope shifts on repump transitions are ~ 100 MHz, but are less of a concern for our experiment design, since our blue MOT capture number is relatively insensitive to the frequency of the repumps. These shifts, listed in table 5.1, are accessible by conventional AOMs [106, 107].

We have already observed successful trapping of ^{86}Sr in a blue MOT, although the overall MOT size is significantly reduced due to the relative abundance of ^{88}Sr versus ^{86}Sr . There are methods to increase the number of atoms in the MOT, which include switching our strontium source out for an isotopically enriched sample of strontium and implementing additional transverse cooling in order to capture a larger fraction of hot atoms in our MOT (see figure 5.1). Regardless, there exist defined pathways towards achieving a sample of ultracold ^{86}Sr , as has already been demonstrated in many other experiments [109, 110].

Transition	^{88}Sr (nm)	^{86}Sr (nm)	$\delta\nu_{IS}$ (MHz)
$^1\text{S}_0 - ^1\text{P}_1$	460.862369	460.862457	-124.80
$^1\text{S}_0 - ^3\text{P}_1$	689.449098	689.449357	-163.81

Table 5.1: Isotope shifts between ^{88}Sr and ^{86}Sr for the primary cooling and trapping transitions. Shifts on repump lines are ~ 100 MHz, but are not listed here since the blue MOT capture number is relatively insensitive to frequency changes in the repumps at the level of the isotope shift [106, 107].

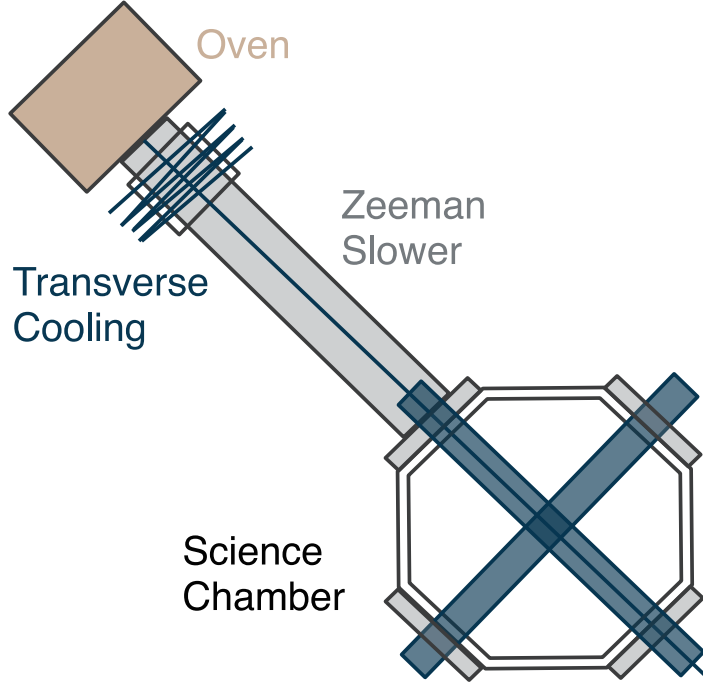


Figure 5.1: A scheme for transverse cooling in our molecular clock. We pick off a small amount of light from our Zeeman slower for additional cooling along the transverse direction, just after our strontium oven. Our current apparatus accommodates transverse cooling through two existing windows. We can achieve adequate trapping of ^{86}Sr and ^{84}Sr in the blue MOT with a 10 cm interaction region.

Once we have cooled and trapped ^{86}Sr , we are again interested in photoassociating atoms to form molecules. In order to create $^{86}\text{Sr}_2$ molecules with high efficiency, we will need to find a favourable pathway for photoassociation, just as in $^{88}\text{Sr}_2$. As already mentioned, our existing theoretical models of strontium atoms and bosonic dimers can be adapted to predict the wavefunctions and corresponding Franck-Condon factors between states in the ground potential and low-lying excited potentials of the molecule.

Theoretical models can predict preferable states for molecule preparation. For instance, early work with $^{88}\text{Sr}_2$ used the $0_u^+(-4, 1)$ state to photoassociate atoms to $X_g(-1, 0/2)$ molecules with high efficiency [39], while later work increased the photoassociative efficiency using the $1_u(-1, 1)$ state, whose Franck-Condon overlap to the molecular ground state is significantly larger [18].

These favourable states are informed by theory. Adequate theory is, therefore, crucial when it comes to future experiment design [39]. Our theoretical models are a useful tool when developing a strategy towards making ultracold $^{86}\text{Sr}_2$. Our current models predict that favourable transitions are ~ 1 GHz detuned from current PA and PD lines [111]. If we plan to interleave our measurements between isotopologues, these isotope shifts are no longer accessible via AOMs and will require additional, phase-locked lasers.

As a first step, we can demonstrate successful formation of $^{86}\text{Sr}_2$ molecules in our experiment, and perform the same spectroscopy of the ground potential and coherent transfer to the rovibrational ground state as we have previously demonstrated in $^{88}\text{Sr}_2$. These studies would be integral to our work towards developing a competitive molecular clock based on $^{86}\text{Sr}_2$ for comparative precision measurements across isotopologues.

Ultimately, to perform a measurement that would allow us to constrain the Yukawa term, we would ideally like to interleave clock measurements between $^{86}\text{Sr}_2$ and $^{88}\text{Sr}_2$. Given our current sequence, which is built using Cicero and Atticus [112], we can design a protocol for interleaving measurements of both isotopologues with relative ease. In particular, we can alternatively cool and trap ^{88}Sr and ^{86}Sr using TTL-controlled AOMs and 5V TTL fibre switches¹, to selectively send light of a given frequency to our experiment (see figure 5.2). Using both the 0 and -1 order deflected light from the AOM, we can span the isotope shift for both the $^1\text{S}_0$ - $^1\text{P}_1$ and $^1\text{S}_0$ - $^3\text{P}_1$ transitions. In order to selectively photoassociate (and photodissociate) ^{86}Sr and ^{88}Sr atoms, we add two additional 689 nm lasers since, in this case, the isotope shift is too large to bridge with AOMs. We phase-lock the ^{86}Sr PA (PD) laser to our ^{88}Sr PA (PD) laser and again selectively direct light via TTL-enabled fibre switches to our chamber to create isotopologues of strontium (see figure 5.3).

¹e.g. OSW12-633E from Thorlabs or OS-2-1-C-55 from Brimrose

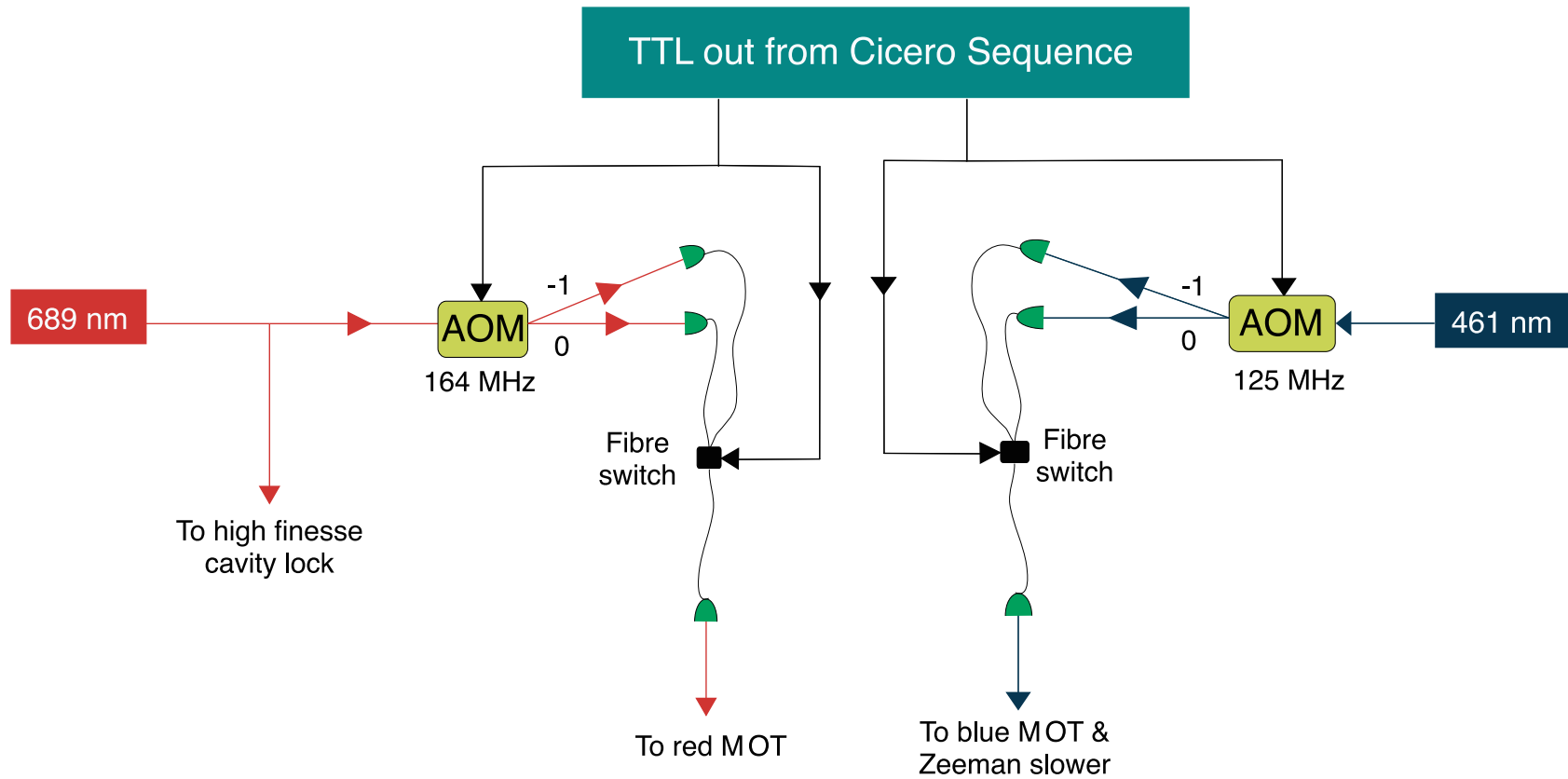


Figure 5.2: A protocol for interleaved cooling and trapping of ^{86}Sr and ^{88}Sr atoms in our system. We use TTL-enabled AOMs to selectively modulate light at a frequency matching the isotope shift for a given transition. An additional AOM (AOMO 3200-125) is included in the red MOT optical path to shift the frequency of light by ~ 164 MHz and another AOM (AOMO 3110-120) is included in the blue MOT optical system to shift the frequency of blue light by ~ 125 MHz before it is distributed to the Zeeman slower and 3 MOT arms. We can switch between input from modulated (-1 order) light and unmodulated (0 order) light using a TTL-enabled fibre switch.

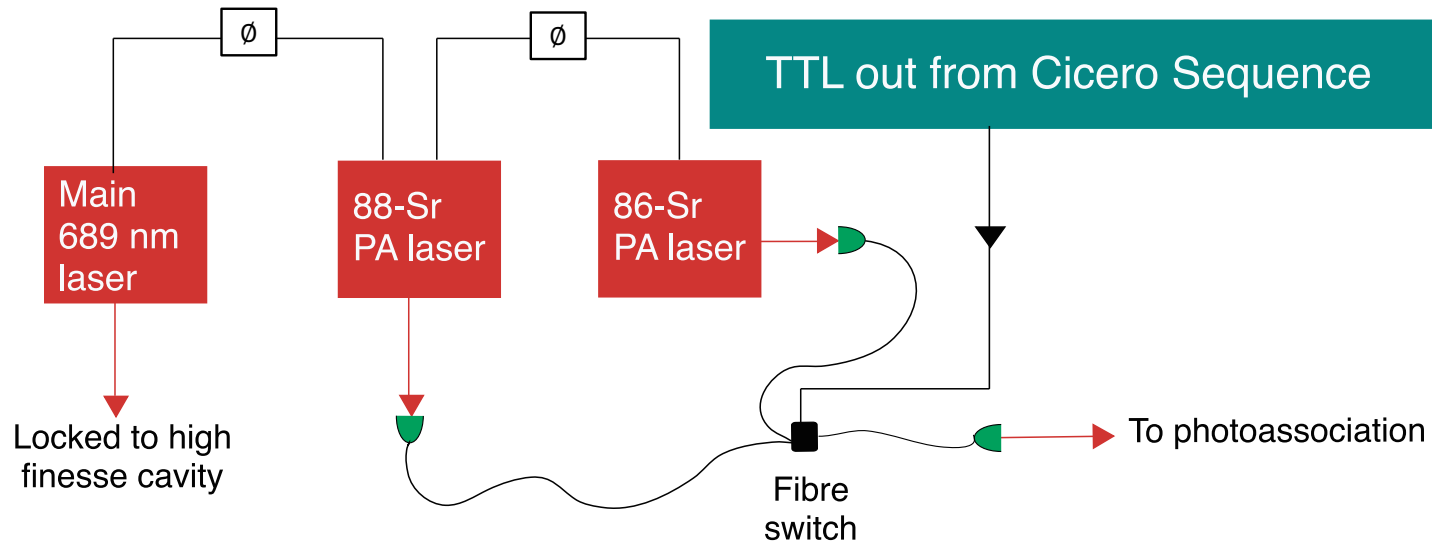


Figure 5.3: A protocol for interleaved creation of weakly-bound $^{86}\text{Sr}_2$ and $^{88}\text{Sr}_2$ molecules. We use a TTL-enabled fibre switch to selectively send photoassociation light to the experiment from two separate, phase-locked lasers. We phase lock the two lasers at ~ 1 GHz, a frequency which matches the isotope shift of the PA line relative to $^{88}\text{Sr}_2$.

In this way, we demonstrate a clear pathway towards selectively and controllably creating $^{86}\text{Sr}_2$ molecules for high-precision spectroscopy and tests of fundamental physics. We propose an interleaved clock measurement at the precision of our current record clock (or better) to probe *extra* frequency shifts in our molecular spectra corresponding to a Yukawa-type correction to gravity, and, in particular, aim to improve constraints on the size of this correction by a few orders of magnitude.

5.2 Setting New Constraints on the Yukawa Term

5.2.1 Current constraints on α

We are particularly interested in constraining α in equation 5.3, effectively the size of this correction, for a given range, λ . Some experiments prefer to define and constrain the quantity gauge coupling constant, g^2 , which is a dimensionless parameter that describes the coupling strength between nucleons and the new particle field; g^2 is related to α by [113]

$$\alpha \sim \left(\frac{\hbar c}{4\pi G m_p^2} \right) g^2 \sim 1.347 \times 10^{37} g^2 \quad (5.7)$$

Historically, there have been many experiments interested in precision measurements of gravity at these short distances. Different experiments are suited for particular range, λ , regimes; for instance, astrophysical observations constrain α at length scales $\sim \lambda > 1 \text{ cm}$ [114, 115]. We are most interested in the region probed by our molecules (roughly the internuclear separation, ~ 0.1 to 10 nm). In the sub-mm range, many of these experiments rely on mechanical setups; some early examples include Eötvos- and Cavendish-type torsion experiments [116], more recent microelectromechanical systems that focus on measuring the Casimir interaction at short distances [115] and experiments with Au-coated spheres in a torsion oscillator [117]. Atoms and molecules are a natural complement to other experiments in this range. There are a number of existing examples of these kinds of measurements using atomic force microscopy, and neutron scattering on a neutral atom target [118–122].

Recent work has set constraints on Yukawa type forces to $\alpha < 1 \times 10^{25}$ for $\lambda \sim 0.1$ nm, $\alpha < 1.7 \times 10^{20}$ for $\lambda \sim 1$ nm and $\alpha < 1.7 \times 10^{18}$ for $\lambda \sim 10$ nm [119, 122–124]. Other complementary work has constrained α on the order of $\alpha \sim 10^{21}$ for ranges near $\lambda \sim 1$ nm and $\alpha \sim 10^{10}$ for ranges near $\lambda \sim 100$ nm [117] (see figure 5.4). Still these bounds are extremely large, leaving the door open for novel experimental strategies that can further bound this Yukawa-type correction.

In the following sections, I extend our record-precision molecular spectroscopy to different strontium isotopologues and project the expected isotope shift due to Yukawa-type corrections to

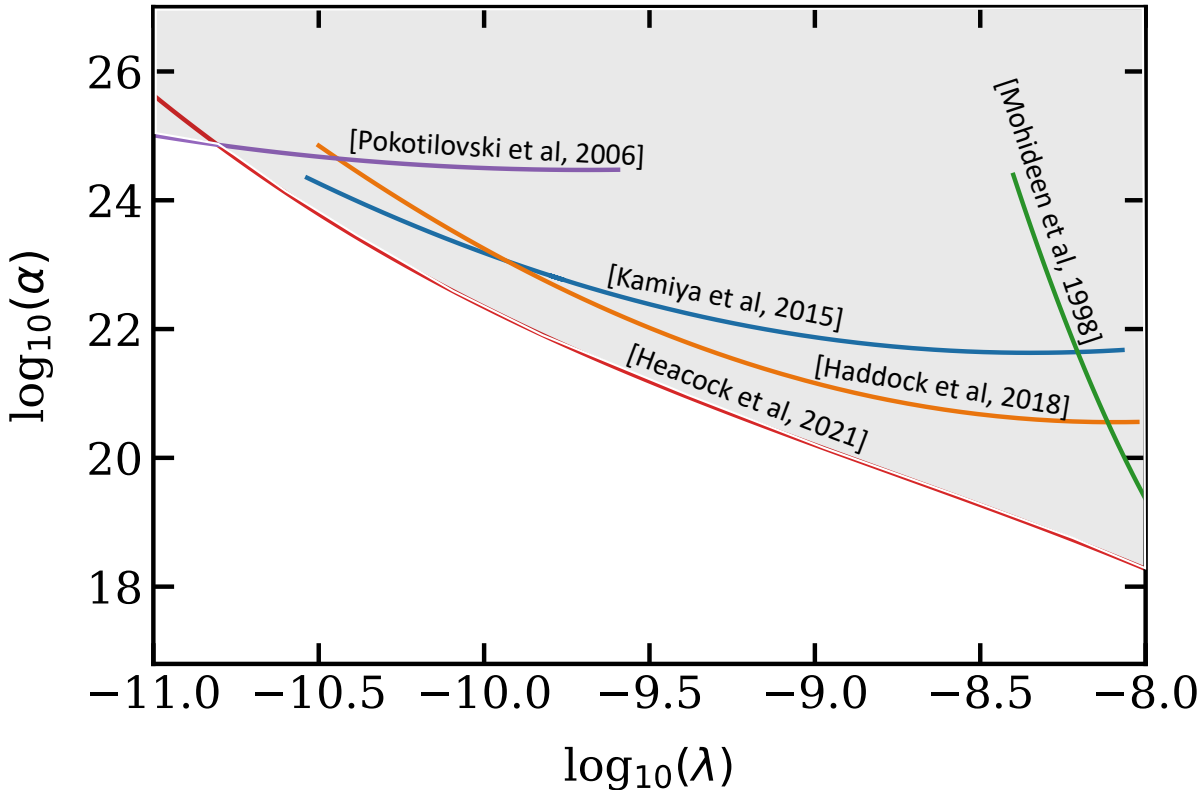


Figure 5.4: The current constraints on the interaction constant, α , and interaction range, λ , of the Yukawa-type interaction from various experiments. Previous measurements include micro-mechanical measurements of the effective Casimir pressure, measurements of the Casimir force using a torsion pendulum, Cavendish-type experiments and neutron scattering experiments [119, 122–125]. The regions above each line are excluded, and those below each line are allowed.

gravity. For the purposes of this proposal, we refer to the above constraints to project the expected mass-dependent shift in strontium. We then leverage our record clock precision to project new limits on $\alpha(\lambda)$.

5.2.2 Projected mass-dependent shift in strontium

From the theoretical perspective, the most reliable model of the ground state of $^{88}\text{Sr}_2$ comes from the RKR analysis of the spectrum obtained in the hot pipe Fourier-transform experiment [31, 46]. *Ab initio* theories of the ground state of $^{88}\text{Sr}_2$ exist using both the local spin-density functional formalism and pseudopotential formalism [126, 127], however, improved models of the ground potential are informed by high-precision experimental spectroscopy. Specifically, we need a method to determine the energy levels of the rovibrational states in the ground potential and their corresponding wavefunctions in order to make predictions about the size of the Yukawa corrections for our particular ground state molecules. In order to do so, we use the discrete variable representation (DVR) method to solve the Schrödinger equation (as in [97]), using a non-linear coordinate transformation on the grid to better sample the potential.

Ultimately, we are interested in probing the isotope shift of clock transitions so as to take advantage of the high levels of precision and accuracy achieved in our molecular system. For each vibrational state in our clock transition, we find the corresponding additional isotope shift due to a Yukawa-type correction (from equation 5.6) to be

$$\delta f_{IS}^{\text{Yukawa}}(v) = f_{\text{Yukawa}}^A(v) - f_{\text{Yukawa}}^{A'}(v) \quad (5.8)$$

and find the overall *extra* isotope shift for the clock transition to be

$$\delta\nu_{IS}^{\text{Yukawa}} = \delta f_{IS}^{\text{Yukawa}}(v) - \delta f_{IS}^{\text{Yukawa}}(v') \quad (5.9)$$

for our two clock states v and v' .

Using the above described model, we calculate the overall frequency shift that emerges from the addition of a Yukawa-type term to the potential by constraining the size of our perturbation to the current limits. Consequently, we project the expected size of the shift under these conditions in our molecular system for each vibrational state, in order to demonstrate the feasibility of probing this new physics with our state-of-the-art molecular clock. We find that we are best suited to probe shifts for Yukawa interactions at 2 nm or shorter (see figure 5.5). Moreover, weakly-bound states exhibit a steep drop off in sensitivity near threshold suggestion that this region will be of particular interest for future experimental studies.

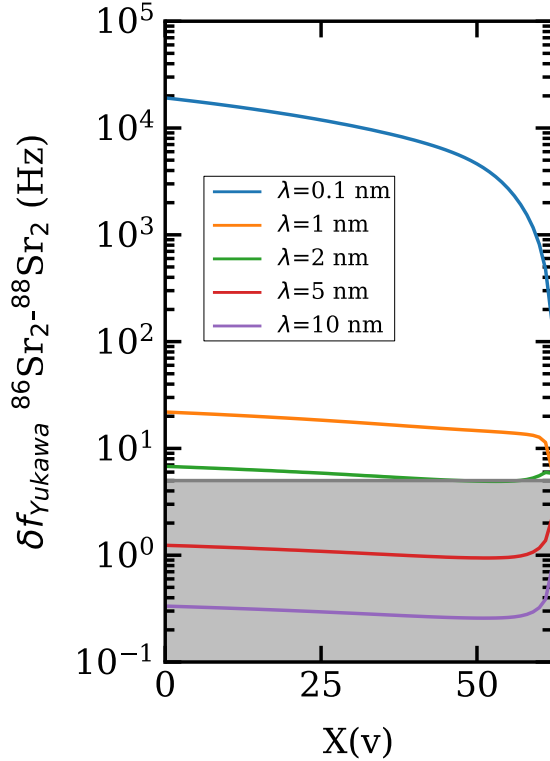


Figure 5.5: Projected shift from the additional Yukawa-type potential. We treat the additional Yukawa term as a perturbation to the Hamiltonian as in equation 5.3 and calculate the projected isotope shift between $^{86}\text{Sr}_2$ and $^{88}\text{Sr}_2$ as a function of vibrational state for a series of ranges, λ . α for each range is set at the current limit. Different vibrational states probe different internuclear separations, and deeply-bound states are more sensitive overall to the Yukawa force. The shaded region corresponds to current absolute clock resolution [18].

We investigate the λ -dependent behaviour of particular states, for a generic $\alpha = 10^{21}$, to further probe the dynamics of the system. We consider specifically $X_g(0, 0)$, $X_g(1, 0)$, $X_g(61, 0)$ and $X_g(62, 0)$. The response of a given state to a Yukawa-like force correlates to its corresponding wavefunction of that state (figure 5.6). It is important to note that $X_g(62, 0)$ state in $^{86}\text{Sr}_2$, referred to as the halo state, has a very small binding energy, -83.00 kHz [128], and very long mean bond length; it experiences a small shift by comparison to the other states studied. Overall, we find extra isotope shifts, $\delta\nu_{IS}^{\text{Yukawa}}$, on these clock transitions on the order of ~ 100 Hz, resolvable with our current clock precision (see figure 5.7 and 5.8).

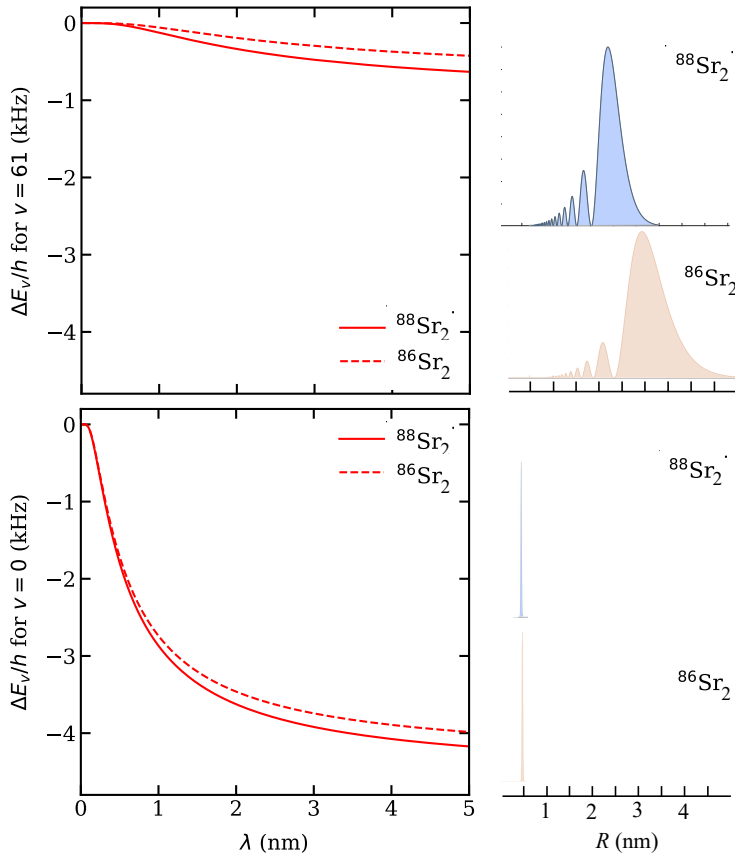


Figure 5.6: Projected shift from the additional Yukawa-type potential as a function of λ . Different vibrational states probe different internuclear separations, and deeply-bound states are more sensitive overall to the Yukawa force. The onset of response corresponds to the particular wavefunction of the state.

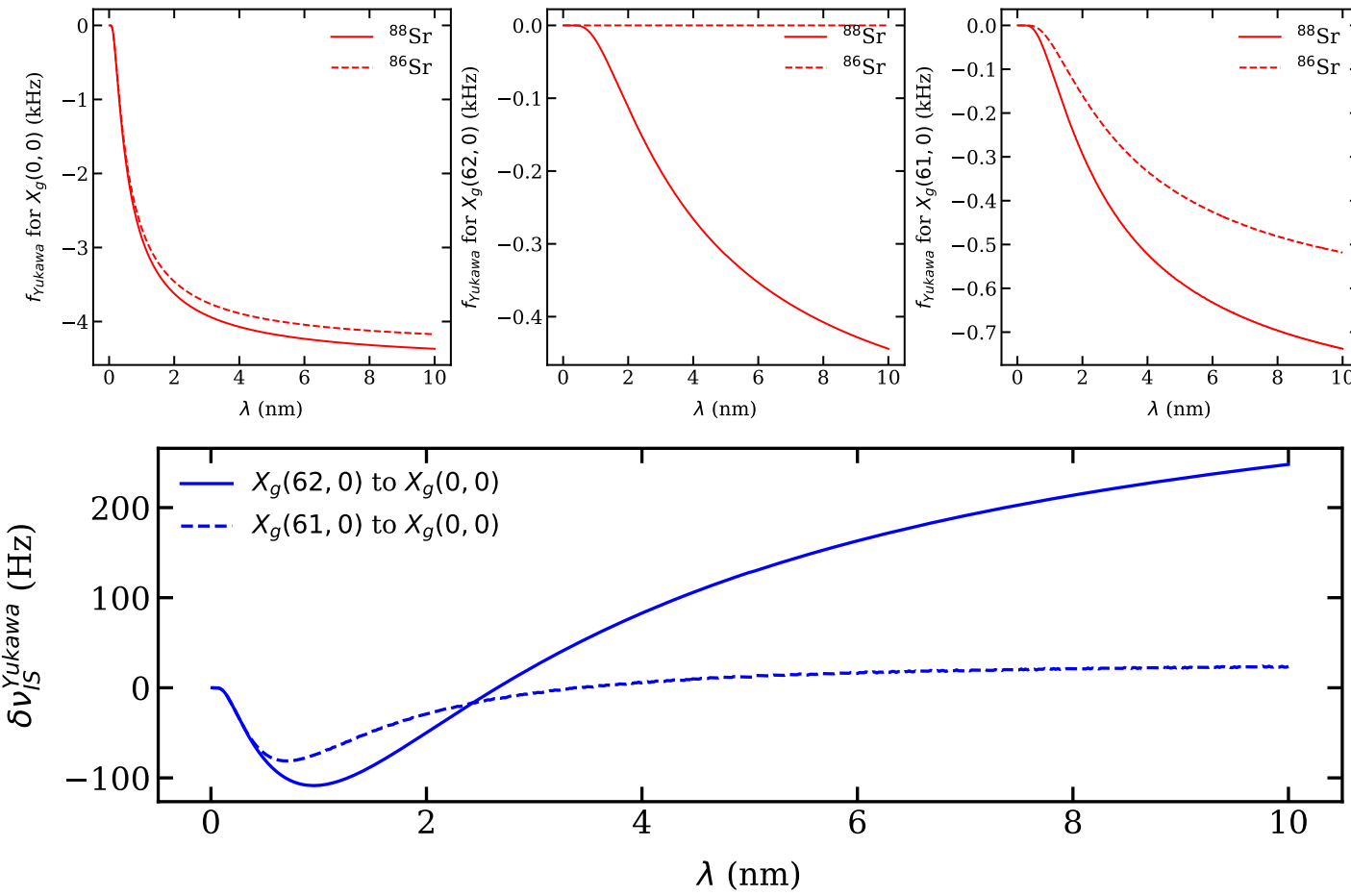


Figure 5.7: Isotope shift of the $X_g(62,0)$ and $X_g(61,0)$ to $X_g(0,0)$ clock transitions in $^{86}\text{Sr}_2$ and $^{88}\text{Sr}_2$. Isotope shifts are calculated by constraining $\alpha = 10^{21}$ for the Yukawa-type potential as in equation 5.3. We show individual frequency shifts introduced by the perturbation for each of $X_g(0,0)$, $X_g(62,0)$ and $X_g(61,0)$ as a function of the range, λ (above). Note that $X_g(62,0)$ state in $^{86}\text{Sr}_2$ has a very small binding energy, -83 kHz, and very long mean bond length, $4436.70\ a_0$; it experiences a small shift by comparison to the other states studied. We consider pairs of states corresponding to potential clock transitions of interest and predict the corresponding isotope shift, $\delta\nu_{IS}^{\text{Yukawa}}$ (below). We find overall isotope shifts on these clock transitions on the order of ~ 100 Hz, which is resolvable with our current clock precision.

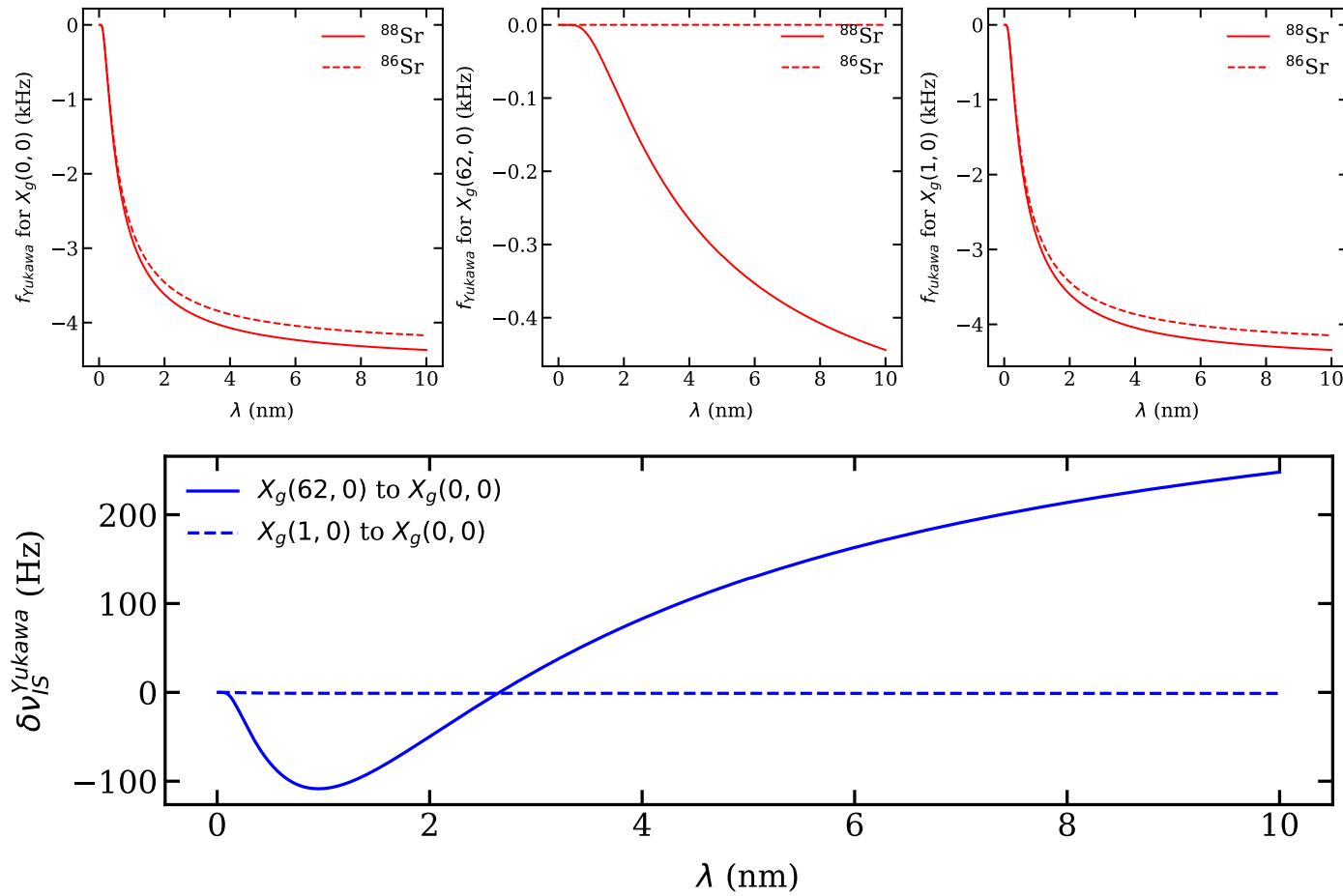


Figure 5.8: Isotope shift of the $X_g(62,0)$ and $X_g(1,0)$ to $X_g(0,0)$ proposed clock transitions in $^{86}\text{Sr}_2$ and $^{88}\text{Sr}_2$. Isotope shifts are calculated by constraining $\alpha = 10^{21}$ for the Yukawa-type potential as in equation 5.3. We show individual frequency shifts introduced by the perturbation for each of $X_g(0,0)$, $X_g(1,0)$ and $X_g(62,0)$ as a function of the range, λ (above). We consider pairs of states corresponding to clock transitions of interest and predict the corresponding isotope shift, $\delta\nu_{IS}^{\text{Yukawa}}$ (below). The $X_g(1,0)$ to $X_g(0,0)$ transition is relatively insensitive to the Yukawa term.

In this way, we demonstrate unequivocally that our system can compete with current benchmark experiments to set constraints on Yukawa-type corrections to non-Newtonian gravity. We consider several candidate clock transitions in order to preferentially design an isotope shift experiment. For example, while the $X_g(62, 0)$ to $X_g(0, 0)$ transition is very sensitive to Yukawa term, $X_g(0, 0)$ to $X_g(1, 0)$ is not very sensitive at all. A measurement that compares both could help us reduce some systematic uncertainties in our experiment. In the following section, we use our current record precision clock, and extensions to other isotopes, to consider the new limits we could impose on Yukawa-type constraints to gravity.

5.2.3 Projected new limits on α

Given our current clock precision, we project new limits on $\alpha(\lambda)$ as a complement to existing experiments. In the following calculation, we assume that theory can fit experimental data to within 1 Hz and, therefore, our resolution is determined only by our clock precision. We have already demonstrated precision spectroscopy on the order of Hz [18], and have proposed several avenues to achieve a sub-Hz level clock in the near future.

For this case study, we consider an isotope shift measurement with our current molecular clock resolution, that is ~ 5 Hz for absolute frequency measurements. We demonstrate improvement by an order of magnitude on constraints on α in the range $\lambda = 0.1$ nm to 10 nm. In this range, we would constrain alpha to below $\alpha = 2.1 \times 10^{19}$ for $\lambda = 10$ nm, below $\alpha = 5.5 \times 10^{19}$ for $\lambda = 1$ nm and below $\alpha = 2.6 \times 10^{21}$ for $\lambda = 0.1$ nm (see figure 5.9). We contextualize limits from our current clock precision within other experimental methods for probing Yukawa-type forces and find that our system places tighter constraints than other experiments for short ranges $\lambda < 1.3$ nm, probing a region that has not been well-studied to date. Moreover, this proposal acts as a framework to motivate similar measurements in other molecular systems and demonstrates the potential for molecules to complement other experiments in probing this physics.

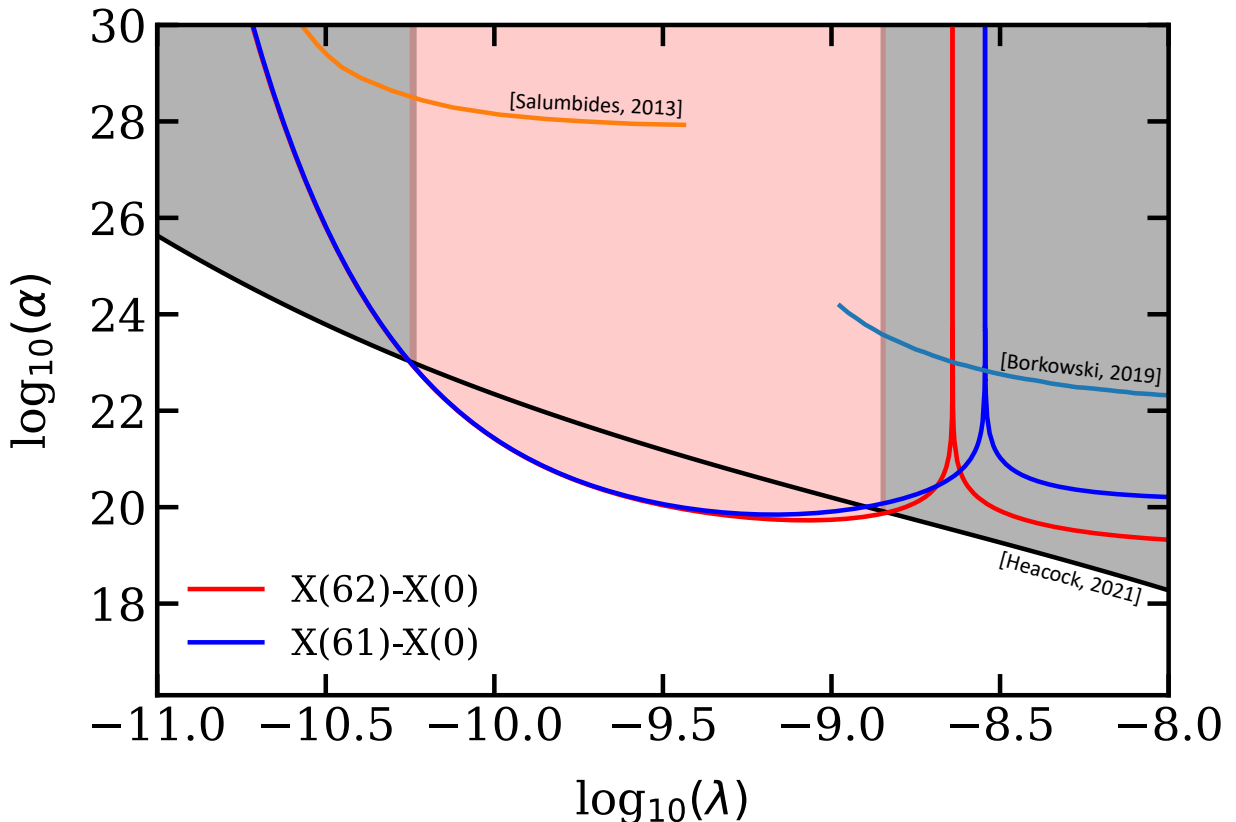


Figure 5.9: Projected constraints on the interaction constant, α , and interaction range, λ , of the Yukawa-type interaction from our clock experiment. We demonstrate improvement by an order of magnitude on constraints on α in the range $\lambda < 1.3$ nm. In this range, we constrain alpha to below $\alpha = 5.5 \times 10^{19}$ for $\lambda = 1$ nm and below $\alpha = 2.6 \times 10^{21}$ for $\lambda = 0.1$ nm. Current limits are included [122] and other molecular experiments are shown [113, 129].

Overall, we find that our molecular clock can probe these types of short-range, mass-dependent new forces with competitive precision as compared to similar molecular experiments as well as other experimental strategies. By leveraging our precise clock in two isotopic species, we can tighten the constraints on the size of the Yukawa interaction in the short range region \sim nm. Given that atomic clocks currently have achieved a relative accuracy up to 10^{-19} , it is reasonable to imagine mHz-level measurements in a molecular clock in the future. Nevertheless, we demonstrate an improved description of the Yukawa corrections by ad order of magnitude, even with our current clock.

Outlook

Our state-of-the-art experiment sits at the cutting edge of metrology with molecules. Molecular systems, such as ours, are of interest because they provide abundant avenues for searches of new physics. In these early stages, our experiment has already demonstrated high levels of precision, with potential for further improvement in the future. To realize a vibrational lattice clock with a fractional uncertainty below 10^{-15} will require a number of technical and scientific changes that can combat the current limitations in our system. Nevertheless, these pathways towards a second-generation clock are well-defined and achievable in the near future.

In our molecular clock, we have the advantage of complete and flexible quantum control that allows us to probe interesting physics throughout the ground potential of our molecule, and at a variety of internuclear separations and sensitivities. Even at lower precision than is achieved in atoms, we can compete with other state-of-the-art experiments to constrain new physics. Given the foundation we have laid out thus far, our experiment can continue to push both the limits of precision for a molecular metrological system and our fundamental understanding at the frontiers of physics. Along the way, this experiment will necessarily lead to new innovations in technology, insights into the fundamental nature of molecules and deepen our understanding of quantum chemistry, quantum control and atomic and molecular physics.

References

- [1] G. Kane, “The mass–energy scales of particle physics and cosmology—the ‘hierarchy’ problem—supersymmetry—hidden sectors,” in *String Theory and the Real World*, ser. 2053–2571, Morgan Claypool Publishers, 2017, 4–1 to 4–6, ISBN: 978-1-6817-4489-6.
- [2] A. D. Ludlow, M. M. Boyd, J. Ye, E. Peik, and P. O. Schmidt, “Optical atomic clocks,” *Rev. Mod. Phys.*, vol. 87, pp. 637–701, 2 2015.
- [3] G. E. Marti, R. B. Hutson, A. Goban, S. L. Campbell, N. Poli, and J. Ye, “Imaging Optical Frequencies with 100 μHz Precision and 1.1 μm Resolution,” *Phys. Rev. Lett.*, vol. 120, p. 103 201, 10 2018.
- [4] T. Zelevinsky, S. Kotochigova, and J. Ye, “Precision Test of Mass-Ratio Variations with Lattice-Confining Ultracold Molecules,” *Phys. Rev. Lett.*, vol. 100, p. 043 201, 4 2008.
- [5] D. Hanneke, B. Kuzhan, and A. Lunstad, “Optical clocks based on molecular vibrations as probes of variation of the proton-to-electron mass ratio,” *Quantum Science and Technology*, vol. 6, no. 1, p. 014 005, Nov. 2020.
- [6] M. S. Safronova, D. Budker, D. DeMille, D. F. J. Kimball, A. Derevianko, and C. W. Clark, “Search for new physics with atoms and molecules,” *Rev. Mod. Phys.*, vol. 90, p. 025 008, 2 2018.
- [7] M. H. Zaheer, N. J. Matjelo, D. B. Hume, M. S. Safronova, and D. R. Leibrandt, *Quantum metrology algorithms for dark matter searches with clocks*, 2023. arXiv: 2302 . 12956 [quant-ph].
- [8] A. Derevianko and M. Pospelov, “Hunting for topological dark matter with atomic clocks,” *Nature Physics*, vol. 10, no. 12, pp. 933–936, Dec. 2014.
- [9] D. Brzeminski, Z. Chacko, A. Dev, I. Flood, and A. Hook, “Searching for a fifth force with atomic and nuclear clocks,” *Phys. Rev. D*, vol. 106, p. 095 031, 9 2022.
- [10] C. Frugieule, E. Fuchs, G. Perez, and M. Schlaffer, “Constraining new physics models with isotope shift spectroscopy,” *Phys. Rev. D*, vol. 96, p. 015 011, 1 2017.
- [11] G. L. Klimchitskaya and V. M. Mostepanenko, “New constraints on Yukawa-type corrections to Newtonian gravity at short separations,” *Gravitation and Cosmology*, vol. 20, no. 1, pp. 3–9, Jan. 2014.

- [12] E. Fischbach, D. E. Krause, V. M. Mostepanenko, and M. Novello, “New constraints on ultrashort-ranged Yukawa interactions from atomic force microscopy,” *Phys. Rev. D*, vol. 64, p. 075 010, 7 2001.
- [13] G. Barontini *et al.*, “Measuring the stability of fundamental constants with a network of clocks,” *EPJ Quantum Technology*, vol. 9, no. 1, p. 12, May 2022.
- [14] M. S. Safronova, “Atomic clocks: The search for variation of fundamental constants with clocks (ann. phys. 5/2019),” *Annalen der Physik*, vol. 531, no. 5, p. 1970 023, 2019.
- [15] O. Hosten, N. J. Engelsen, R. Krishnakumar, and M. A. Kasevich, “Measurement noise 100 times lower than the quantum-projection limit using entangled atoms,” *Nature*, vol. 529, no. 7587, pp. 505–508, Jan. 2016.
- [16] M. Abdel-Hafiz *et al.*, *Guidelines for developing optical clocks with 10^{-18} fractional frequency uncertainty*, 2019. arXiv: 1906.11495 [physics.atom-ph].
- [17] W. M. Itano *et al.*, “Quantum projection noise: Population fluctuations in two-level systems,” *Phys. Rev. A*, vol. 47, pp. 3554–3570, 5 1993.
- [18] K. H. Leung *et al.*, “Terahertz vibrational molecular clock with systematic uncertainty at the 10^{-14} level,” *Phys. Rev. X*, vol. 13, p. 011 047, 1 2023.
- [19] K. H. Leung, “The strontium molecular lattice clock: Vibrational spectroscopy with hertz-level accuracy,” Ph.D. dissertation, Columbia University, 2023.
- [20] M. Borkowski, “Optical lattice clocks with weakly bound molecules,” *Phys. Rev. Lett.*, vol. 120, p. 083 202, 8 2018.
- [21] J. A. Muniz, D. J. Young, J. R. K. Cline, and J. K. Thompson, “Cavity-QED measurements of the ^{87}Sr millihertz optical clock transition and determination of its natural linewidth,” *Phys. Rev. Res.*, vol. 3, p. 023 152, 2 2021.
- [22] P. Atkins and J. de Paula, *Atkins' Physical Chemistry*, 7th ed. Oxford, 2002.
- [23] E. Fischbach and C. L. Talmadge, *The Search for Non-Newtonian Gravity*. Springer New York, 1999.
- [24] A. Santamaria, “Masses, mixings, Yukawa couplings and their symmetries,” *Physics Letters B*, vol. 305, no. 1-2, pp. 90–97, 1993.
- [25] I. Majewska, “Theoretical description of ultracold strontium molecules in an optical lattice: Control of photodissociation and interpretation of molecular clock experiments,” Ph.D. dissertation, University of Warsaw, 2021.

- [26] J. Pique, F. Hartmann, *et al.*, “Hyperfine interactions in homonuclear diatomic molecules and u-g perturbations. I. Theory,” *J. Phys. France*, vol. 47, no. 11, pp. 1909–1916, 1986.
- [27] L. Veseth, “Hund’s coupling case (c) in diatomic molecules. I. Theory,” *Journal of Physics B: Atomic and Molecular Physics*, vol. 6, no. 8, p. 1473, 1973.
- [28] T. A. Isaev, “Direct laser cooling of molecules,” *Physics-Uspekhi*, vol. 63, pp. 289–302, 3 Mar. 2020.
- [29] C. B. Osborn, “The Physics of Ultracold Sr₂ Molecules: Optical Production and Precision Measurement,” Ph.D. dissertation, Columbia University, 2013.
- [30] C.-H. Lee, “Quantum metrology with a molecular lattice clock and state-selected photodissociation of ultracold molecules,” Ph.D. dissertation, Columbia University, 2020.
- [31] A. Stein, H. Knöckel, and E. Tiemann, “The 1S+1S asymptote of Sr₂ studied by Fourier-transform spectroscopy,” *The European Physical Journal D*, vol. 57, no. 2, pp. 171–177, 2010.
- [32] S. S. Kondov *et al.*, “Molecular lattice clock with long vibrational coherence,” *Nature Physics*, vol. 15, no. 11, pp. 1118–1122, 2019.
- [33] J. Ye, H. J. Kimble, and H. Katori, “Quantum state engineering and precision metrology using state-insensitive light traps,” *Science*, vol. 320, no. 5884, pp. 1734–1738, 2008.
- [34] H. Katori, M. Takamoto, V. G. Pal’chikov, and V. D. Ovsiannikov, “Ultrastable optical clock with neutral atoms in an engineered light shift trap,” *Phys. Rev. Lett.*, vol. 91, p. 173 005, 17 2003.
- [35] M. McDonald, B. H. McGuyer, G. Z. Iwata, and T. Zelevinsky, “Thermometry via light shifts in optical lattices,” *Physical Review Letters*, vol. 114, 2 Jan. 2015.
- [36] M. S. Safranova, S. G. Porsev, U. I. Safranova, M. G. Kozlov, and C. W. Clark, “Blackbody-radiation shift in the Sr optical atomic clock,” *Phys. Rev. A*, vol. 87, p. 012 509, 1 2013.
- [37] C. J. Foot, *Atomic Physics* (Oxford Master Series in Physics). London, England: Oxford University Press, Nov. 2004.
- [38] A. P. Thorne, *Spectrophysics*. Springer Netherlands, 1988.
- [39] K. H. Leung *et al.*, “Transition strength measurements to guide magic wavelength selection in optically trapped molecules,” *Phys. Rev. Lett.*, vol. 125, p. 153 001, 15 2020.
- [40] J. M. Brown and A. Carrington, *Rotational Spectroscopy of Diatomic Molecules* (Cambridge Molecular Science). Cambridge University Press, 2003.

- [41] A. Hansson and J. K. Watson, “A comment on Hönl-London factors,” *Journal of Molecular Spectroscopy*, vol. 233, no. 2, pp. 169–173, 2005.
- [42] J. L. Dunham, “The Energy Levels of a Rotating Vibrator,” *Phys. Rev.*, vol. 41, pp. 721–731, 6 1932.
- [43] A. Stein, H. Knöckel, and E. Tiemann, “The states $(1)^1\Sigma_u^+$, $(1)^1\Pi_u$ and $(2)^1\Sigma_u^+$ of Sr_2 studied by Fourier-transform spectroscopy,” *The European Physical Journal D*, vol. 64, no. 2, pp. 227–238, 2011.
- [44] S. Chandra, “Relation between spectroscopic constants with limited Dunham coefficients,” *Pramana*, vol. 65, no. 6, pp. 1133–1137, 2005.
- [45] K. P. Huber and G. Herzberg, “Constants of diatomic molecules,” in *Molecular Spectra and Molecular Structure: IV. Constants of Diatomic Molecules*. Boston, MA: Springer US, 1979, pp. 8–689, ISBN: 978-1-4757-0961-2.
- [46] A. Stein, H. Knöckel, and E. Tiemann, “Fourier-transform spectroscopy of Sr_2 and revised ground-state potential,” *Phys. Rev. A*, vol. 78, p. 042508, 4 2008.
- [47] K. H. Leung, E Tiberi, B Iritani, I Majewska, R Moszynski, and T Zelevinsky, “Ultracold $^{88}\text{Sr}_2$ molecules in the absolute ground state,” *New Journal of Physics*, vol. 23, no. 11, p. 115002, 2021.
- [48] N. V. Vitanov, A. A. Rangelov, B. W. Shore, and K. Bergmann, “Stimulated Raman adiabatic passage in physics, chemistry, and beyond,” *Rev. Mod. Phys.*, vol. 89, p. 015006, 1 2017.
- [49] W. Zheng *et al.*, “Optimal control of stimulated Raman adiabatic passage in a superconducting qudit,” *NJP Quantum Information*, vol. 8, no. 1, p. 9, 2022.
- [50] A. Yang *et al.*, “Singlet pathway to the ground state of ultracold polar molecules,” *Phys. Rev. Lett.*, vol. 124, p. 133203, 13 2020.
- [51] A. Chotia *et al.*, “Long-Lived Dipolar Molecules and Feshbach Molecules in a 3D Optical Lattice,” *Phys. Rev. Lett.*, vol. 108, p. 080405, 8 2012.
- [52] L. W. Cheuk *et al.*, “Observation of Collisions between Two Ultracold Ground-State CaF Molecules,” *Phys. Rev. Lett.*, vol. 125, p. 043401, 4 2020.
- [53] R. Bause, A. Christianen, A. Schindewolf, I. Bloch, and X.-Y. Luo, “Ultracold Sticky Collisions: Theoretical and Experimental Status,” *The Journal of Physical Chemistry A*, vol. 127, no. 3, pp. 729–741, 2023.

- [54] J. Söding, D. Guéry-Odelin, P. Desbiolles, *et al.*, “Giant spin relaxation of an ultracold cesium gas,” 1998.
- [55] M. Guo *et al.*, “Dipolar Collisions of Ultracold Ground-State Bosonic Molecules,” *Phys. Rev. X*, vol. 8, p. 041 044, 4 2018.
- [56] P. S. Julienne, T. M. Hanna, and Z. Idziaszek, “Universal ultracold collision rates for polar molecules of two alkali-metal atoms,” Jun. 2011.
- [57] R. Moszynski, P. S. Zuchowski, and B. Jeziorski, “Time-independent coupled-cluster theory of the polarization propagator,” *Collection of Czechoslovak Chemical Communications*, vol. 70, pp. 1109–1132, 8 Aug. 2005.
- [58] B. Jeziorski and R. Moszynski, “Explicitly connected expansion for the average value of an observable in the coupled-cluster theory,” *International Journal of Quantum Chemistry*, vol. 48, no. 3, pp. 161–183, 1993.
- [59] T. Korona, M. Przybytek, and B. Jeziorski, “Time-independent coupled cluster theory of the polarization propagator. implementation and application of the singles and doubles model to dynamic polarizabilities and van der waals constants,” *Molecular Physics*, vol. 104, pp. 2303–2316, 13-14 Jul. 2006.
- [60] W. Skomorowski, F. Pawłowski, C. P. Koch, and R. Moszynski, “Rovibrational dynamics of the strontium molecule in the $a^1\Sigma_u^+a^1\Sigma_u^+$, $c^3\Pi_u$, and $a^3\Sigma_u^+a^3\Sigma_u^+$ manifold from state-of-the-art ab initio calculations,” *The Journal of Chemical Physics*, vol. 136, no. 19, p. 194 306, 2012.
- [61] A. Christianen, M. W. Zwierlein, G. C. Groenenboom, and T. Karman, “Photoinduced two-body loss of ultracold molecules,” *Physical Review Letters*, vol. 123, 12 Sep. 2019.
- [62] P. D. Gregory, J. A. Blackmore, S. L. Bromley, and S. L. Cornish, “Loss of Ultracold $\text{Rb}^{87}\text{Cs}^{133}$ Molecules via Optical Excitation of Long-Lived Two-Body Collision Complexes,” *Physical Review Letters*, vol. 124, 16 Apr. 2020.
- [63] L.-S. Ma, P. Jungner, J. Ye, and J. L. Hall, “Delivering the same optical frequency at two places: Accurate cancellation of phase noise introduced by an optical fiber or other time-varying path,” *Opt. Lett.*, vol. 19, no. 21, pp. 1777–1779, 1994.
- [64] B. Rauf, M. C. V. López, P. Thoumany, M. Pizzocaro, and D. Calonico, “Phase noise cancellation in polarisation-maintaining fibre links,” *Review of Scientific Instruments*, vol. 89, no. 3, p. 033 103, 2018.
- [65] M. Lombardi, “The Use of GPS Disciplined Oscillators as Primary Frequency Standards for Calibration and Metrology Laboratories,” *NCSLI Measure: The Journal of Measurement Science*, vol. 3, pp. 56–65, Aug. 2008.

- [66] M. Lombardi, L. Nelson, A. Novick, and V. Zhang, “Time and Frequency Measurements Using the Global Positioning System,” *Cal Lab: The International Journal of Metrology*, vol. 8, pp. 26–33, Jul. 2001.
- [67] S. J. Dick, D. D. McCarthy, and B. Luzum, *Polar motion: Historical and scientific problems*. 2000.
- [68] K. Szymaniec *et al.*, “Operation of caesium fountain frequency standards with remote hydrogen maser references,” vol. 55, no. 6, p. 782, 2018.
- [69] T. Takano, R. Mizushima, and H. Katori, “Precise determination of the isotope shift of ^{88}Sr – ^{87}Sr optical lattice clock by sharing perturbations,” *Applied Physics Express*, vol. 10, no. 8, p. 089 201, 2017.
- [70] V. I. Yudin *et al.*, “Generalized autobalanced ramsey spectroscopy of clock transitions,” *Phys. Rev. Appl.*, vol. 9, p. 054 034, 5 2018.
- [71] R. C. Brown *et al.*, “Hyperpolarizability and operational magic wavelength in an optical lattice clock,” *Phys. Rev. Lett.*, vol. 119, p. 253 001, 25 2017.
- [72] K. Beloy *et al.*, “Modeling motional energy spectra and lattice light shifts in optical lattice clocks,” *Phys. Rev. A*, vol. 101, p. 053 416, 5 2020.
- [73] S. G. Porsev and A. Derevianko, “Multipolar theory of blackbody radiation shift of atomic energy levels and its implications for optical lattice clocks,” *Phys. Rev. A*, vol. 74, p. 020 502, 2 2006.
- [74] M. Planck, *The theory of heat radiation / Max Planck ; introduction by Allan A. Needell ; translation by Morton Masius*. Tomash ; American Institute of Physics Los Angeles : New York, 1988, xlvi, 470 p. : ISBN: 0883185970.
- [75] J. Harvey, “Discovering Chemistry with Natural Bond Orbitals. By Frank Weinhold and Clark E. Landis.,” *Angewandte Chemie International Edition*, vol. 52, Jan. 2013.
- [76] S. Falke *et al.*, “A strontium lattice clock with 3×10^{-17} inaccuracy and its frequency,” *New Journal of Physics*, vol. 16, no. 7, p. 073 023, Jul. 2014.
- [77] A. Ludlow *et al.*, “Sr Lattice Clock at 1×10^{-16} Fractional Uncertainty by Remote Optical Evaluation with a Ca Clock,” *Science (New York, N.Y.)*, vol. 319, pp. 1805–8, Apr. 2008.
- [78] C. Lisdat, J. S. R. V. Winfred, T. Middelmann, F. Riehle, and U. Sterr, “Collisional Losses, Decoherence, and Frequency Shifts in Optical Lattice Clocks with Bosons,” *Phys. Rev. Lett.*, vol. 103, p. 090 801, 9 2009.

- [79] M. Takamoto, F.-L. Hong, R. Higashi, and H. Katori, “An optical lattice clock,” *Nature*, vol. 435, no. 7040, pp. 321–324, 2005.
- [80] A. D. Ludlow *et al.*, “Systematic study of the ^{87}Sr clock transition in an optical lattice,” *Phys. Rev. Lett.*, vol. 96, p. 033 003, 3 2006.
- [81] R. Le Targat *et al.*, “Accurate optical lattice clock with ^{87}Sr atoms,” *Phys. Rev. Lett.*, vol. 97, p. 130 801, 13 2006.
- [82] E. Arahata and T. Nikuni, “Bose-Condensed Gases in a 1D Optical Lattice at Finite Temperatures,” *Journal of Low Temperature Physics*, vol. 148, pp. 345–349, Aug. 2007.
- [83] T. Bothwell *et al.*, “JILA SrI optical lattice clock with uncertainty of 2.0×10^{-18} ,” *Metrologia*, vol. 56, no. 6, p. 065 004, 2019.
- [84] G. Kestler, K. Ton, D. Filin, M. S. Safronova, and J. T. Barreiro, “Magic wavelengths of the Sr ($5s^2 {}^1S_0$ - $5s5p {}^3P_1$) intercombination transition near the $5s5p {}^3P_1$ - $5p {}^2{}^3P_2$ transition,” *Phys. Rev. A*, vol. 105, p. 012 821, 1 2022.
- [85] T. A. Zheng *et al.*, “Magic wavelengths of the Yb ($6s^2 {}^1S_0$ – $6s6p {}^3P_1$) intercombination transition,” *Phys. Rev. A*, vol. 102, p. 062 805, 6 2020.
- [86] J. Mitroy, M. S. Safronova, and C. W. Clark, “Theory and applications of atomic and ionic polarizabilities,” *Journal of Physics B: Atomic, Molecular and Optical Physics*, vol. 43, no. 20, p. 202 001, 2010.
- [87] K. D. Nanda and A. I. Krylov, “Static polarizabilities for excited states within the spin-conserving and spin-flipping equation-of-motion coupled-cluster singles and doubles formalism: Theory, implementation, and benchmarks,” *The Journal of Chemical Physics*, vol. 145, no. 20, p. 204 116, 2016.
- [88] E. Epifanovsky *et al.*, “Software for the frontiers of quantum chemistry: An overview of developments in the Q-Chem 5 package,” *The Journal of Chemical Physics*, vol. 155, no. 8, p. 084 801, Aug. 2021.
- [89] I. S. Lim, H. Stoll, and P. Schwerdtfeger, “Relativistic small-core energy-consistent pseudopotentials for the alkaline-earth elements from Ca to Ra,” *The Journal of Chemical Physics*, vol. 124, no. 3, p. 034 107, 2006.
- [90] A. Dalgarno, A. L. Ford, and J. C. Browne, “Direct Sum-of-States Calculations of the Frequency-Dependent Polarizability of H_2 ,” *Physical Review Letters*, vol. 27, pp. 1033–1036, 16 Oct. 1971.
- [91] J. M. Brown and A. Carrington, *Rotational Spectroscopy of Diatomic Molecules*. Cambridge: Cambridge University Press, 2003, ISBN: 9780511814808.

- [92] T. G. A. Heijmen, R. Moszynski, P. E. S. Wormer, and A. van der Avoird, “Symmetry-adapted perturbation theory applied to interaction-induced properties of collisional complexes,” *Molecular Physics*, vol. 89, no. 1, pp. 81–110, 1996.
- [93] R. J. Le Roy and R. B. Bernstein, “Dissociation energies of diatomic molecules from vibrational spacings of higher levels: application to the halogens*,” *Chemical Physics Letters*, vol. 5, no. 1, pp. 42–44, 1970.
- [94] R. J. Le Roy, *Energy Levels of a Diatomic near Dissociation*. The Chemical Society, London, 1973, pp. 113–171.
- [95] R. J. Le Roy, “Long-range potential coefficients from RKR turning points: C₆ and C₈ for B(3Π₁Ou+)-state Cl₂, Br₂, and I₂,” *Can. J. Phys.*, vol. 52, no. 3, pp. 246–256, Feb. 1974.
- [96] B. Ji, C.-C. Tsai, and W. C. Stwalley, “Proposed modification of the criterion for the region of validity of the inverse-power expansion in diatomic long-range potentials,” *Chem. Phys. Lett.*, vol. 236, no. 3, pp. 242–246, Apr. 1995.
- [97] D. T. Colbert and W. H. Miller, “A novel discrete variable representation for quantum mechanical reactive scattering via the S-matrix Kohn method,” *The Journal of Chemical Physics*, vol. 96, no. 3, pp. 1982–1991, Feb. 1992.
- [98] E. Tiesinga, C. J. Williams, and P. S. Julienne, “Photoassociative spectroscopy of highly excited vibrational levels of alkali-metal dimers: Green-function approach for eigenvalue solvers,” *Phys. Rev. A*, vol. 57, no. 6, pp. 4257–4267, 1998.
- [99] B. N. Taylor and C. E. Kuyatt, *NIST Technical Note 1297. Guidelines for evaluating and expressing the uncertainty of NIST measurement results*. US Department of Commerce, Technology Administration, National Institute of Standards and Technology, 1994.
- [100] J. W. Farley and W. H. Wing, “Accurate calculation of dynamic stark shifts and depopulation rates of Rydberg energy levels induced by blackbody radiation. Hydrogen, helium, and alkali-metal atoms,” *Phys. Rev. A*, vol. 23, pp. 2397–2424, 5 1981.
- [101] T. Middelmann, S. Falke, C. Lisdat, and U. Sterr, “High accuracy correction of blackbody radiation shift in an optical lattice clock,” *Phys. Rev. Lett.*, vol. 109, p. 263 004, 26 2012.
- [102] C. Lisdat, S. Dörscher, I. Nosske, and U. Sterr, “Blackbody radiation shift in strontium lattice clocks revisited,” *Phys. Rev. Res.*, vol. 3, p. L042036, 4 2021.
- [103] W. H. King, *Isotope shifts in atomic spectra* (Physics of Atoms and Molecules). New York, NY: Springer, Sep. 2013.

- [104] M. Athanasakis-Kaklamanakis, S. G. Wilkins, A. A. Breier, and G. Neyens, “King-plot analysis of isotope shifts in simple diatomic molecules,” *Phys. Rev. X*, vol. 13, p. 011 015, 1 2023.
- [105] J. C. Berengut, C. Delaunay, A. Geddes, and Y. Soreq, “Generalized King linearity and new physics searches with isotope shifts,” *Phys. Rev. Res.*, vol. 2, p. 043 444, 4 2020.
- [106] H. Miyake, N. C. Pisenti, P. K. Elgee, A. Sitaram, and G. K. Campbell, “Isotope-shift spectroscopy of the $^1S_0 \rightarrow ^3P_1$ and $^1S_0 \rightarrow ^3P_0$ transitions in strontium,” *Phys. Rev. Res.*, vol. 1, p. 033 113, 3 2019.
- [107] S. Stellmer, F. Schreck, and T. C. Killian, “DEGENERATE QUANTUM GASES OF STRONTIUM,” in *Annual Review of Cold Atoms and Molecules*, WORLD SCIENTIFIC, 2014, pp. 1–80.
- [108] S. Stellmer, M. K. Tey, B. Huang, R. Grimm, and F. Schreck, “Bose-einstein condensation of strontium,” *Phys. Rev. Lett.*, vol. 103, p. 200 401, 20 2009.
- [109] S. Stellmer, B. Pasquiou, R. Grimm, and F. Schreck, “Creation of ultracold Sr₂ molecules in the electronic ground state,” *Phys. Rev. Lett.*, vol. 109, p. 115 302, 11 2012.
- [110] N. Poli, R. E. Drullinger, G. Ferrari, J. Léonard, F. Sorrentino, and G. M. Tino, “Cooling and trapping of ultracold strontium isotopic mixtures,” *Phys. Rev. A*, vol. 71, p. 061 403, 6 2005.
- [111] M. Borkowski *et al.*, “Mass scaling and nonadiabatic effects in photoassociation spectroscopy of ultracold strontium atoms,” *Phys. Rev. A*, vol. 90, p. 032 713, 3 2014.
- [112] A. Keshet and W. Ketterle, “A distributed, graphical user interface based, computer control system for atomic physics experiments,” *Rev. Sci. Instrum.*, vol. 84, no. 1, p. 015 105, Jan. 2013.
- [113] M. Borkowski *et al.*, “Weakly bound molecules as sensors of new gravitylike forces,” *Scientific Reports*, vol. 9, no. 1, p. 14 807, 2019.
- [114] B. Jain *et al.*, *Novel probes of gravity and dark energy*, 2013. arXiv: 1309.5389 [astro-ph.CO].
- [115] C. R. Jamell and R. S. Decca, “Yukawa corrections to the newtonian gravitational potential: Finite size effects in a recent experiment,” *Int. J. Mod. Phys. Conf. Ser.*, vol. 03, pp. 48–57, Jan. 2011.
- [116] B. Schwarzschild, “Reanalysis of old Eötvös data suggests 5th force... to some,” *Phys. Today*, vol. 39, no. 10, pp. 17–20, Oct. 1986.

- [117] G. L. Klimchitskaya and V. M. Mostepanenko, “Dark matter axions, non-Newtonian gravity and constraints on them from recent measurements of the Casimir force in the micrometer separation range,” *Universe*, vol. 7, no. 9, p. 343, Sep. 2021.
- [118] R. S. Decca, D. López, H. B. Chan, E. Fischbach, D. E. Krause, and C. R. Jamell, “Constraining New Forces in the Casimir Regime Using the Isoelectronic Technique,” *Phys. Rev. Lett.*, vol. 94, p. 240 401, 24 2005.
- [119] Y. Kamiya, K. Itagaki, M. Tani, G. N. Kim, and S. Komamiya, “Constraints on new gravitylike forces in the nanometer range,” *Physical Review Letters*, vol. 114, 16 Apr. 2015.
- [120] G. L. Klimchitskaya, U. Mohideen, and V. M. Mostepanenko, “Constraints on corrections to newtonian gravity from two recent measurements of the casimir interaction between metallic surfaces,” *Phys. Rev. D*, vol. 87, p. 125 031, 12 2013.
- [121] V. V. Nesvizhevsky, G. Pignol, and K. V. Protasov, “Neutron scattering and extra-short-range interactions,” *Phys. Rev. D*, vol. 77, p. 034 020, 3 2008.
- [122] B. Heacock *et al.*, “Pendellösung interferometry probes the neutron charge radius, lattice dynamics, and fifth forces,” *Science*, vol. 373, no. 6560, pp. 1239–1243, 2021.
- [123] Y. N. Pokotilovski, “Constraints on new interactions from neutron scattering experiments,” *Physics of Atomic Nuclei*, vol. 69, no. 6, pp. 924–931, Jun. 2006.
- [124] U. Mohideen and A. Roy, “Precision Measurement of the Casimir Force from 0.1 to $0.9\mu\text{m}$,” *Phys. Rev. Lett.*, vol. 81, pp. 4549–4552, 21 1998.
- [125] C. C. Haddock *et al.*, “Search for deviations from the inverse square law of gravity at nm range using a pulsed neutron beam,” *Phys. Rev. D*, vol. 97, p. 062 002, 6 2018.
- [126] R. O. Jones, “Molecular bonding in group IIA dimers Be₂–Ba₂,” *J. Chem. Phys.*, vol. 71, no. 3, pp. 1300–1308, Aug. 1979.
- [127] G. Ortiz and P. Ballone, “Pseudopotentials for non-local-density functionals,” *Phys. Rev. B*, vol. 43, pp. 6376–6387, 8 1991.
- [128] J. A. Aman, J. C. Hill, R. Ding, K. R. A. Hazzard, T. C. Killian, and W. Y. Kon, “Photoassociative spectroscopy of a halo molecule in ⁸⁶Sr,” *Phys. Rev. A*, vol. 98, p. 053 441, 5 2018.
- [129] E. J. Salumbides, J. C. J. Koelemeij, J. Komasa, K. Pachucki, K. S. E. Eikema, and W. Ubachs, “Bounds on fifth forces from precision measurements on molecules,” *Phys. Rev. D*, vol. 87, p. 112 008, 11 2013.